

Instituto Tecnológico de Costa Rica

Electronics Engineering School



Design and Implementation of a MEMS Piezoelectric Sensor Array for Patient Specific Instrumentation used for Total Ankle Replacement

Thesis submitted in partial fulfillment of the requirements for the degree of Master of Science in Electronics Engineering, Micro Electromechanical Systems (MEMS) Program Major.

Marco V. Bedoya Serrano

January 2017

I declare that the current thesis document has been constructed entirely by my own work, using available based knowledge concepts and literature related to the subject in matter, and also, introducing new generated knowledge and experimental data gathered by this own work.

In different sections where I have utilized external bibliography, I have proceeded to indicate the source through the corresponding citation all along the manuscript. As a result, I fully assume the responsibility for this thesis work and for its contents.

Declaro que el presente documento de tesis ha sido realizado enteramente por mi persona, utilizando y aplicando literatura referente al tema e introduciendo conocimientos y resultados experimentales propios.

En los casos en que he utilizado bibliografía he procedido a indicar las fuentes mediante las respectivas citas bibliográficas. En consecuencia, asumo la responsabilidad total por el trabajo de tesis realizado y por el contenido del presente documento.

Marco Bedoya Serrano

Cartago, Costa Rica, January 24th, 2016

Céd/ID: 1-1349-0679

**Tribunal evaluador
Acta de evaluación**

Tesis de maestría defendida ante el presente Tribunal Evaluador como requisito para optar por el grado académico de maestría, del Instituto Tecnológico de Costa Rica.

Estudiante: **Ing. Marco Bedoya Serrano**

Nombre del Proyecto:

"Design and Implementation of a MEMS Piezoelectric Sensor Array for Patient Specific Instrumentation used for Total Ankle Replacement"

Miembros del Tribunal



M/Sc. Marta Vilchez Monge
Profesora lectora



M.Sc. Paul Michael Stenniski
Profesor lector



Dr. - Ing. Paola Vega Castillo
Directora de Tesis

Los miembros de este Tribunal dan fe de que la presente Tesis de Maestría para optar por el grado académico de Máster en Electrónica con Énfasis en Sistemas Microelectromecánicos y cumple con las normas establecidas por la Escuela de Ingeniería Electrónica.


Nota Final de Tesis: 95


Cartago, 24 de enero de 2017

Instituto Tecnológico de Costa Rica
Escuela de Ingeniería Electrónica
Tesis de Maestría
Tribunal evaluador

Tesis de maestría defendida ante el presente Tribunal Evaluador como requisito para optar por el grado académico de maestría, del Instituto Tecnológico de Costa Rica.

Miembros del Tribunal


M.Sc. Marta Vilchez Monge
Profesora lectora


M.Sc. Paul Michael Stenniski
Profesor lector


Dr. - Ing. Paola Vega Castillo
Directora de Tesis

Los miembros de este Tribunal dan fe de que la presente tesis ha sido aprobada y cumple con las normas establecidas por la Escuela de Ingeniería Electrónica.

Cartago, 24 de enero de 2017

Instituto Tecnológico de Costa Rica
Escuela de Ingeniería Electrónica
Tesis de Maestría

Abstract

Keywords: Flexible pressure map sensor, MEMS, patient specific instrumentation, Total Ankle Replacement, orthopedic sensing technology, contact mechanics, finite element analysis.

For several decades, research has been conducted for Total Ankle Replacement (TAR) to be established as the optimal surgical treatment for diseased or degenerative ankle joints. Few reports exist regarding patient specific instrumentation for TAR and to the author knowledge, there is no work related to sensing technology designed for patient specific instrumentation in Total Ankle Replacement. This research analyses how piezoelectric, patient specific instrumentation and micro-electro-mechanical system (MEMS) technologies can be combined to design a thin flexible pressure map sensor for Total Ankle Replacement application. More specifically, the sensor design claims to provide information on how the patient specific instrument fits onto the bone surface when performing a Total Ankle Replacement. Finite Element Analysis is used (FEA) to verify design calculations and afterwards, fabrication and assembly of the sensor are followed. A custom made data acquisition system was designed and built to read the output of the sensor. Prototype successful implementation was achieved through experimental setup, where several test cases scenarios were recorded. In particular, sensor voltage output data ranges from approximately **128 mV to 310 mV**, translated in mechanical deformation from approximately **59 MPa to 161 MPa**, while theoretical mechanical deformation ranged from **50 MPa to 150 MPa** according to calculations and FEA results.

Acknowledgements

First, I would like to express my deepest and most sincere gratitude to my supervisor Dr. Paola Vega-Castillo, Vice-president for Research and Outreach at the Instituto Tecnológico de Costa Rica. Her experience, guidance, constant support and breadth of knowledge were a key factor for the accomplishment of this thesis work. The contributions from Dr. Vega established the path for this investigation and led to the thesis successful completion.

Also, I would like to extend my gratitude to advisors Paul Stemniski, Director of R&D for Wright Medical Technology and Marta Vilchez, professor at Instituto Tecnológico de Costa Rica. In Particular, I thank Paul Stemniski for his mentoring during my years of work in Wright Medical Technology, which made possible the thought of this project in the first place.

In addition, I thank to Roy Araya and Cristian Ledezma for their contributions in the electronic engineering development that was needed for this work. The knowledge and experience they shared played a key factor in developing the data acquisition system for the sensor designed and implemented in this thesis.

My deepest gratitude are also directed to my beloved family, that warm and unique feeling that I have had all my life has made possible this very important milestone in my life.

Contents

| | |
|---|-----|
| CHAPTER 1 | 13 |
| 1.1 Introduction | 13 |
| 1.2 Objectives | 14 |
| 1.3 This thesis is structured as follows: | 14 |
| CHAPTER 2 | 16 |
| 2.1 Background..... | 16 |
| 2.2 Historical Use of Sensing Technology in Total Joint Replacement | 25 |
| 2.3 Problem Description | 30 |
| 2.4 Contact Mechanics Foundations..... | 32 |
| 2.5 Piezoelectricity Foundations | 36 |
| CHAPTER 3 | 41 |
| 3.1 Sensor Configuration and Geometry | 41 |
| 3.2 MEMS Design | 44 |
| 3.2.1 Measurement System for Determining Experimental Contact Force Reaction..... | 48 |
| 3.2.1.1 Sensor Thickness Definition | 50 |
| 3.3 Finite Element Analysis of the Contact Problem | 52 |
| 3.4 Finite Element Analysis of the Thin Piezo Electric Film..... | 58 |
| CHAPTER 4..... | 61 |
| 4.1 Sensor Assembly | 61 |
| 4.2 Data Acquisition System and Test Fixture..... | 63 |
| 4.3 Test Results and Analysis..... | 70 |
| CHAPTER 5 | 93 |
| 5.1 Conclusions | 93 |
| 5.2 Future work | 97 |
| Bibliography | 100 |
| Appendix A | 103 |
| Determining Experimental Contact Force | 103 |
| Appendix B..... | 106 |
| Source Code for Arduino program | 106 |
| Appendix C..... | 109 |
| Data Acquisition Board Schematic, layout information and Bill of Materials (BOM) | 109 |

List of Figures

Figure 2.1.1. An extract of the preoperative navigation plan based on the CT scan images as part TruMatch® Personalized Solutions from DePuy Synthes (Warsaw, Indiana). [23]..... 19

Figure 2.1.2. Patient specific cutting guides for the SIGNATURE™ Personalized Patient Care System. (a) Femoral block and, (b) tibial block. Adapted from [26]. 20

Figure 2.1.3. Standing coronal radiographs after total knee replacement was conducted assisted by patient specific instrumentation. (A) Measurement of the limb mechanical axis, (B) measurement of the femoral component (FFC) and the frontal tibial component (FTC) to determine varus/valgus alignment [35] 22

Figure 2.1.4. PROPCHECY® INBONE® tibia and talus alignment guides onto the bone model surface (a) and cadaveric testing of each instrument placement, tibia (b) and talus (c). Adapted from [10]..... 24

Figure 2.2.1. Smart implant evolution illustration. Adapted from [41] 25

Figure 2.2.2. Instrumented tibia component with self-harvesting system, full assembled device shown in a) and circuit board along with sensors layout in b). Adapted from [63]. 27

Figure 2.2.3. Instrumented shoulder endoprosthesis and section view to depict the sensing electronics (a) and Instrumented vertebral body and section model to depict electro-mechanical measurement system (b). Adapted from [57] 29

Figure 2.3.1. CAD model representation of patient specific instrumentation and the corresponding fit onto the bone surface. a) Illustration of how the instruments are placed onto the surface, b) oblique view depicting proposed thin film sensor to adopt bone-instrument contact surface. Images developed by the author..... 31

Figure 2.3.2. Actual instrument and 3D printed bone model with a polyamide film in the contact interface, a) oblique lateral view and b) oblique bottom view. 31

Figure 2.4.1. a) Non-Conforming curved contact surfaces. b) Partially Conforming Contact surfaces. 32

Figure 2.4.2. Normal and tangential components acting on the contact interface [79]. 34

Figure 2.4.3. a) CAD 3D models of the bone and the simplified patient specific instrument, b) two dimensional view in the zx plane of the interactions responsible for the contact transmission: the normal pressure $p(s)$ and the tangential traction or frictional force $q(s)$ and c) contact approximation of both curvatures. 36

Figure 2.5.1. Uni-axial film being stretched in the 1 direction and the corresponding piezoelectric response.. 37

Figure 3.1.1. Models provided by Wright Medical Technology for this application development, a) individual models and b) patient specific instrument placed on top of the bone model to resemble the application. 41

Figure 3.1.2. Proposed sensor node array for collecting data from the piezoelectric film. 42

Figure 3.1.3. 3D model of sensor assembly and layer structure, a) exploded view, b) top view and c) bottom view. 43

| | |
|---|----|
| <i>Figure 3.1.4. Flexible pressure sensor structure, a) lateral view where the bottom electrodes are seen as small rectangles in a section view, b) front view where the top electrodes are seen as small rectangles in a section view.</i> | 44 |
| <i>Figure 3.2.1. Simply supported beam with uniformly distributed load analogy</i> | 45 |
| <i>Figure 3.2.2. Beam cantilever fixed at one end analogy.</i> | 46 |
| <i>Figure 3.2.3. Composite beam and one layer beam equivalence</i> | 47 |
| <i>Figure 3.2.1.1. Force approximation experiment –</i> | 48 |
| <i>Image shown from one of the runs performed.</i> | 48 |
| <i>Figure 3.2.1.2. Minitab results from tolerance interval analysis.</i> | 49 |
| <i>Figure 3.2.4. Moments diagram, a) for the simply supported beam at two ends and b) for the cantilever analogy.</i> | 50 |
| <i>Figure 3.3.1. Finite Element Analysis process followed for model convergence.</i> | 55 |
| <i>Figure 3.3.2. Mesh result according to the slave and master surface selection with the simplified instrument, a) only bone and instrument contact analysis and b) piezoelectric film included in the model.</i> | 55 |
| <i>Figure 3.3.3. Contact analysis results from FEA; a) High friction simulation resulting in 159.6 MPa as maximum pressure and b) Low friction simulation resulting in contact stress of 147.3 MPa.</i> | 56 |
| <i>Figure 3.3.4. Shear contact pressure results from FEA, a) Shear in x- direction, b) Shear in y-direction. Units in MPa.</i> | 57 |
| <i>Figure 3.4.1. Electrical potential distribution from FEA; electrical in response to the mechanical deformation, units in V.</i> | 58 |
| <i>Figure 3.4.2. Von-Mises stress distribution, a) Front view without patient instrument and, b) Lateral view showing instrument. Units in MPa.</i> | 59 |
| <i>Figure 3.4.3. Relation between mechanical properties and the electric output from mesh element with highest positive voltage reading.</i> | 60 |
| <i>Figure 4.1.1. Layout of the vertical and horizontal electrodes, a) vertical and b) horizontal.</i> | 61 |
| <i>Figure 4.1.2. Actual printed vertical and horizontal electrodes on the polyamide substrate (with adhesive layer on)</i> | 62 |
| <i>Figure 4.1.3. Assembled sensor as the structured discussed in chapter 3, a) frontal oblique view of the array of sensing nodes and b) piezoelectric film purchased from GoodFellow, company model FV301301.</i> | 62 |
| <i>Figure 4.2.1. High level view of the steps followed by the sensor output.</i> | 63 |
| <i>Figure 4.2.2. Designed circuit for the data acquisition system.</i> | 64 |
| <i>Figure 4.2.3. Block diagram for the DAQ board design.</i> | 65 |
| <i>Figure 4.2.4. Modified Block diagram for the DAQ board design with ground connections.</i> | 66 |
| <i>Figure 4.2.5. Modified Sensor pins output with ground connections.</i> | 67 |
| <i>Figure 4.2.6. DAQ board layout for two copper layers.</i> | 67 |

| | |
|---|-----|
| Figure 4.2.7. Non-soldered PCB | 68 |
| Figure 4.2.8. All components soldered PCB. | 68 |
| Figure 4.2.9. Test pneumatic fixture..... | 69 |
| Figure 4.3.1. Screenshot from the oscilloscope SainSmart DDS-120 model. | 73 |
| Figure 4.3.2. Schematic for one node sensor output reading | 74 |
| Figure 4.3.3. Laser Doppler vibrometer signal read example for piezoelectric placed on a cantilever beam [87]. | 76 |
| Figure 4.3.4. Source signal from sensor (yellow) and the corresponding amplified value. | 76 |
| Figure 4.3.5. SainSmart oscilloscope DDS-120 model device structure. | 77 |
| Figure 4.3.6. Schematic for one node sensor output reading when adding the DAQ board. | 78 |
| Figure 4.3.7. Graphical representation of both series: the data from the sensor when no DAQ board is connected (orange) and the data from the sensor but when connecting the DAQ as a second channel to the oscilloscope (blue). | 79 |
| Figure 4.3.8. Graphical comparison between a) experimental data gathering and b) Computational analysis results. | 82 |
| Figure 4.3.9. Graphical representation for the amplified signal from the DAQ board. | 83 |
| Figure 4.3.10. Entire sensor data collection, surface plot for electrical response, units in V..... | 87 |
| Figure 4.3.11. Entire sensor data collection, surface plot for mechanical response, in MPa. | 89 |
| Figure 4.3.12. Piezoelectric film surface plot, a) generated from the experimental data and b) generated by the FEA model results. | 90 |
| Figure 4.3.13. Rotation of the instrument relative to the bone model fixed position. Angle measured to be 20° clockwise..... | 91 |
| Figure 4.3.14. Pressure map resulting from an incorrect alignment of the patient specific instrument pressed on the bone, with a rotation angle of 20° clockwise. | 92 |
| Figure 5.2.1. Proposed DAQ block diagram to include voltage followers to each signal and remove the ground connections from the sensor inputs..... | 98 |
| Figure A1. Calibration results from last registered calibration on October 10th 2014, a) general information and linearity test, b) repeatability and eccentricity tests. | 103 |
| Figure C1. DAQ Board schematic image..... | 111 |

List of Tables

| | | |
|--------------|--|-----|
| TABLE I. | Numbers in volume of total knee replacement assisted with Patient specific instrumentation. Cases from 2011 and 2012, adapted from [36]..... | 23 |
| TABLE II. | Coronal alignment outliers of partial reported outcomes in conventional and computer assisted total knee replacement surgeries. For further reference of the studies presented below [26]. | 24 |
| TABLE III. | Short summary of experimental studies conducted in vivo for evaluating resulting contact forces in the hip joint..... | 28 |
| TABLE IV. | Summary of Experimental and modeled studies reporting maximum in vivo knee forces. For details about the study's authors, refer to the following citation [62]. | 30 |
| TABLE V. | Comparative table between commercial PZT, PVDF and P(VDF-TrFE) piezo electric films. Extracted from [19 and 86]. | 38 |
| TABLE VI. | Sensor geometry parameters and dimensions. | 43 |
| TABLE VII. | sensor layer thickness summary | 44 |
| TABLE VIII. | ultimate tensile strength for each layer on the sensor assembly | 47 |
| TABLE IX. | Results table for sensor design, simple beam analysis. | 51 |
| TABLE X. | Results table for sensor design, cantilever analysis..... | 52 |
| TABLE XI. | Summary for material properties used in FEA models..... | 53 |
| TABLE XII. | fixture pneumatic pressure equivalence to the instrument..... | 70 |
| TABLE XIII. | Arduino digital output matrix (coarse reading)..... | 71 |
| TABLE XIV. | Isolated Sensor Characterization Data | 74 |
| TABLE XV. | Sensor with DAQ Board Characterization Data | 78 |
| TABLE XVI. | Mechanical deformation expressed as the stress induced by an external pressure applied to the sensor. | 80 |
| TABLE XVII. | Full resolution measurement for the sensor, averaged voltages values on each node from the columns and rows..... | 86 |
| TABLE XVIII. | full resolution measurement, mechanical response of the sensor | 88 |
| TABLE XIX. | Materials and Equipment for Experiment Setup..... | 103 |
| TABLE XX. | Experiment Runs and Records | 104 |
| TABLE XXI. | Symbol Description for Schematic Reading | 109 |
| TABLE XXII. | Bill of Materials for DAQ board layout..... | 110 |

CHAPTER 1

Thesis Overview

- 1.1 Introduction
- 1.2 Objectives
- 1.3 Thesis Structure

1.1 Introduction

It has been a long way for a technology such as the Total Ankle Replacement (TAR) to take a leading role when addressing the arthritic ankle. Currently, third generation ankle implants are exhibiting more reliable results compared to the ones used in the early 1970's. This scenario is setting a new expectation for the outcomes of this procedures and the overall patient acceptance. In addition, sensing technology has remained unexplored for this kind of applications, and using MEMS approach to design and overcome such specific problem as evaluating how a "*patient-custom made instrument*" fits onto the patient actual bone surface, provides a somewhat unique value to this work, which consists on the implementation of a 25x17 piezoelectric sensor array for measuring the change in contact pressure between two different objects and is intended for Total Ankle Replacement (TAR) applications. Patient specific instrumentation (PSI) holds a great potential for Total Ankle Replacement, particularly in terms of procedure outcome and operative room time reduction. However, to our knowledge there is no published research related to mapping the pressure contact between the instrumentation and the bone interface, to assist the surgeon in ensuring the instrument is placed in the correct location as indicated and designed in the pre-operative navigation report. The idea of having a very thin layer of a flexible sensor that can read the contact pressure exerted by the patient-specific instrumentation once it is pressed against the bone surface, is found to be particularly helpful for evaluating whether the instrument is placed correctly prior to the initial drilling of the bone at the beginning of a TAR procedure. This would help to overcome the uncertainty of the placement of the patient-specific instrument.

1.2 Objectives

In terms of the general objective, this thesis works claims to design, build and test, a flexible and surface adjustable pressure sensor based on Micro Electromechanical Systems (MEMS) methodologies, fabrication and modeling techniques. The sensor scope is to be provide the pressure map of the contact surface area from the application of patient specific instrumentation for Total Ankle Replacement.

1.3 This thesis is structured as follows:

Chapter 1: presents a brief introductory chapter intended to provide an overview to the approach taken by the author.

Chapter 2: summarizes the *state-of-the-art*. A literature analysis is conducted to understand each section of the thesis structure: starting with a review of the surgical procedure for total ankle replacement, its background, challenges, drawbacks and evolution. Later, a patient specific or custom made instrumentation analysis for total joint replacement, where different approaches are brought to discussion in regard whether there is a true advantage of using this kind of instrumentation or not. Included in this same chapter, an overview of the sensor technology developed for orthopedic procedures is presented, which is followed by the problem description being addressed by this thesis work. Finally in this chapter, contact mechanics and piezoelectricity foundations are discussed to provide background of the theory applied in this thesis.

Chapter 3: is intended to establish a baseline for the sensor design and to provide evidence of experimental data involved in the application development. A key milestone is described in this chapter, as it refers to the sensor geometry, dimensions, material selection and final layer configuration. A second milestone shown in this chapter is the results of the Finite Element Analysis simulation carried out to understand the nature of the contact interaction, and the behavior of a thin piezoelectric film being forced to adopt a highly irregular surface when pressed in between two different objects.

Chapter 4: it describes the data acquisition system designed for this particular application and the general results obtained. It compiles measurement data, as well as the analysis,

assumptions and potential explanations to the issues encountered during the development of this sensing system.

Chapter 5: presents the conclusions and further future work. Additional information can also be found in the annexes.

CHAPTER 2

Literature Review

- 2.1 Background
- 2.2 Historical use of Sensing technology in Total Joint Replacement
- 2.3 Problem Description
- 2.4 Contact Mechanics Foundations
- 2.5 Piezo Electricity Foundations

2.1 Background

In December of 2012, a global study on the burden of diseases and the corresponding worldwide impact, found musculoskeletal disorders affect more than 1.7 billion people worldwide, being the 2nd greatest cause of disability [1] as they decrease quality of life, social functioning and mental health [2]. The point prevalence of physical disability was estimated at 4-5 percent of the adult population of Canada, the United States and Western Europe [3]. During 2010-2012, an estimated of 52.5 million of adults in the United States (22.7%) reported doctor-diagnosed arthritis, increasing at an approximate rate of 0.87 million adults per year. These numbers are fairly consistent with a projected number of 67 million of adults that will be diagnosed with arthritis by 2030 [1].

From the data mentioned above, it can be noticed that the impact of musculoskeletal disorders has two large components: the symptoms strongly increase over time while decreasing a person's quality of life. As a result of these conditions, arthroplasty (also known as joint replacement procedures) have been widely investigated for different joints, providing successful and reliable clinical results for total joint replacements such as knee, hip and shoulder [4]. In particular, joint replacement has been considered for treatment of ankle joint diseases since the early 1970s [5, 6]. The results, however, were not acceptable, mainly because the designers and surgeons failed to reproduce the normal mechanics of the ankle joint, to provide implant stability (due to the inability to adequately restore ligament function) and to involve the subtalar joint in the ankle analysis [6]. These results did not improve in the following decade, which lead to ankle arthrodesis (also known as fusing or fixing a joint together) becoming the preferred surgical treatment option for patients with severe ankle joint diseases [7]. However, the drawbacks of arthrodesis such as nonunion, degenerative changes to surrounding joints, potential risk of infection and loss of mobility, helped to create a

renewed interest in the total ankle replacement option (TAR). In addition, improvements in the bio-mechanical design of prostheses created a higher satisfaction level in the 1990s [8]. Unfortunately, the results observed during this time were still not as successful as those obtained for knees and hips, mostly because of the remaining poor understanding of ankle joint kinematics [9]. It wasn't until after the year 2000 that several reports started to demonstrate, through mid and long term studies, better results in total ankle replacement (TAR) [10].

Despite the significant improvements that have been made in total ankle prosthesis design over the last two decades, the success of total ankle replacement has been highly dependent on the alignment methods and surgical technique [10-13]. Moreover, one of the key factors for TAR to be successful is component longevity, which is a major constraint as the mean age for candidates is estimated at 55 years old [6]; especially when compared to total knee reconstruction which have a mean age of 68 years old for patients who undergo this procedure [14]. This situation establishes an additional challenge for total ankle replacement to succeed; nonetheless, it has been demonstrated for knee reconstruction that the implant longevity is related to accurate component alignment [15]. Conversely to knee and hip joints, ankles have a smaller contact area and articulating surfaces: loads in the ankle can reach values as high as 500% the body weight (BW) during the stance phase of walking [11]. Thus, it is vital to understand the challenges that ankle implants have to overcome in order to obtain the clinical acceptance that knees and hips implants have obtained, while different technological approaches such as preoperative navigation systems and novel sensing methods are ways to improve the outcomes of total ankle arthroplasty.

In terms of preoperative navigation systems, the goal is to create customized and disposable blocks or tools unique to each individual anatomy, intended to increase accuracy of bone preparation and decrease the number of misaligned components [16]. Designing and building individual blocks is also known as patient specific instrumentation (PSI).

The concept of these instruments was first introduced in total knee replacement systems [17]. Some of the potential benefits of these devices include reduced blood loss, no need to invade the intramedullary canal, reduced operation time, reduced time under anesthesia, and very importantly, the ability for the surgeon to plan the best-fit alignment options for a patient prior to surgery day [17, 18]. When using patient specific instrumentation for ankle

arthroplasty, there is an extra benefit not mentioned above: a reduction in reliance on intraoperative fluoroscopy, except as needed to verify the pre-operative plan is being followed appropriately [18]. In addition, these patient anatomy based instruments provide accurate bone resections, which is often difficult to achieve with conventional instrumentation [2]. Noble et al demonstrated [19], significant reduction in the number of instruments used during the procedure, duration of the hospital stay, and skin-to-skin time of operation, for a cohort of 29 patients who underwent total knee replacements. In addition, no adverse or complicated events were reported as instrument-related for several surgeries [20, 21].

Chareancholvanich et al published no significant difference when compared to conventional instrumentation methods, regarding blood loss, skin incision (length), bone cutting time, operative time, and length of stay in days [22]. These results were obtained from a randomized group of 80 patients for total knee reconstruction: 40 subjects underwent the procedure with the regular instrumentation, while the rest underwent with patient specific cutting guides (PSCG). In addition, the primary outcome of the study was to determine mechanical axis deviation in the coronal plane from both techniques. However, no statistically significance differences were observed after the implantation [22].

Additional incongruences regarding the outcome provided by conventional instrumentation surgery compared to patient specific surgery instrumentation for knee replacements are shown in the literature [2, 19, 20, 22-26]. For instance, there are clinical reports that indicate no significant differences between patients who went under total knee replacement using either conventional instrumentation (CON) or patient specific instrumentation (PSI) [16,19, 27-29]. Marimuthu et al conducted [28] a retrospective analysis of 300 patients who underwent total knee replacement between February 2012 and June 2013 using the LEGION® total knee Prosthesis (Smith and Nephew, Memphis, Tennessee); 185 patients underwent with conventional instrumentation and 115 with patient specific guides or instruments from the VISIONARE™(Smith and Nephew, Memphis, Tennessee). The results for the coronal alignment were based in the hip-knee angle (HKA), femoral coronal alignment and tibial coronal alignment [28]. The postoperative limb showed no statically significant difference between the two groups (CON and PSI) in terms of the proportion of outliers, which values were set at 2° and 3° as cut-off limits. 80.5% of the subjects who went

with the conventional instrumentation procedure had a femoral coronal alignment within 2° of neutral (90°), while 81.6% had the same result for the PSI group. Regarding tibial coronal alignment, 89.7% of the patients for the CON group had the results within the 2° of neutral, compared with the 89.6% for the PSI group. For the sagittal alignment and the component rotation, no statically significant difference was observed. Barret et al performed a study in which 66 TKAs with PSI were compared to 86 conventional TKAs and 81 based on computed assisted surgery (CAS) technology [23]. The study was performed between October 2009 and December 2010, using the TruMatch® Personalized Solutions (DePuy Synthes, Warsaw, Indiana) system with the P.F.C® Total Knee System (DePuy Synthes, Warsaw, Indiana). 81.3% of the PSI knees were reported within the 3° of the planned mechanical alignment (in the coronal plane), compared to 82.5% for CAS and 77.4% for conventional instrumentation [23]. This system is shown in Figure 2.1.1. When using 3° as the cut-off value, there was no statically difference between the three scenarios. Figure 2.1.1 shows partial information contained in the preoperative navigation plan for the TruMatch® system.

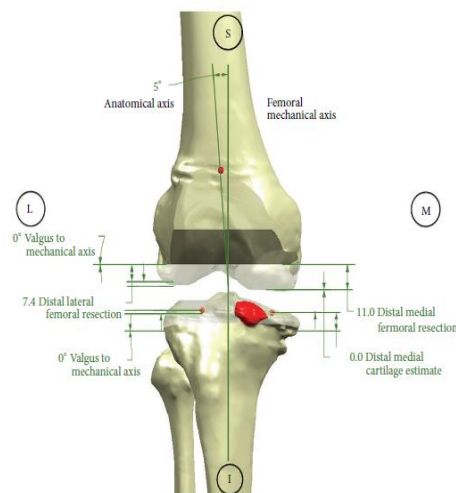


Figure 2.1.1. An extract of the preoperative navigation plan based on the CT scan images as part TruMatch® Personalized Solutions from DePuy Synthes (Warsaw, Indiana). [23]

In 2012, Ng et al [26] conducted a large retrospective analysis comparing the results from 569 TKAs using patient specific positioning guides (PSPG), with 155 surgeries performed with conventional methods. The navigation used was the SIGNATURE™ Personalized Patient care system (Biomet Inc, Warsaw, Indiana), shown in Figure 2.1.2.

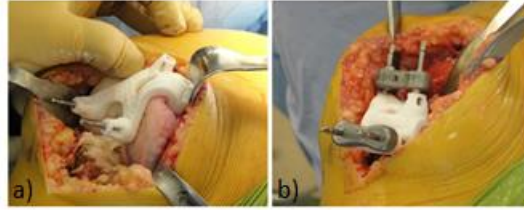


Figure 2.1.2. Patient specific cutting guides for the SIGNATURE™ Personalized Patient Care System. (a) Femoral block and, (b) tibial block. Adapted from [26].

The results were based in different parameters [26]; they reported that the overall mechanical axis (OMA) passing through the central third of the knee was observed in 88 % of the patients who underwent with the PSPG group, while in 78% for patients with the conventional or manual instrumentation group; the hip-knee-ankle angle were similar in both technologies, however the number of outliers (outside $\pm 3^\circ$) were significantly fewer for the PSPG, 9% compared with 22% for the conventional procedure. In general, this work establishes considerably better outcomes when using patient specific guides, compared not only to manual instrumentation but to computer assisted navigation as well. An interesting study compares the results achieved by customized patient instrumentation knee surgery, against conventional or manual methods, and also against the preoperative plan created as part of the navigation system [24]. From this report, 50 patients were evaluated: 25 consecutive patients underwent TKA with the preoperative TruMatch® navigation system (Depuy, Warsaw, Indiana), which included a preoperative plan to establish an ideal component alignment based on predefined surgeon preferences [24], while the other 25 went under the conventional technique. A portion of this final preoperative navigation plan is also shown in Figure 2.1.1. As for the conventional group, the target ideal alignment was defined as 90° from both, the coronal and sagittal planes. In the customized instrumentation group (CIG), the absolute difference of the femoral alignment was 0.67° in the coronal plane and 1.2° in the sagittal plane, while the average magnitude of angular deviation of the tibial alignment was 0.9° in the coronal plane and 1.3° in the sagittal plane. The differences found for traditional instrumentation were 1.5° and 2.3° for the femoral coronal and sagittal alignment, respectively, and 1.8° for the tibial coronal alignment. The statistical differences were significant only for the femoral alignment; procedures performed within CIG demonstrated more accurate results than the traditional instrumentation group. An additional study of 32 TKAs using PSI® ZIMMER demonstrates good clinical results for all cases. Prior to knee

reconstruction surgery, a preoperative plan is created and then approved by the surgeon before the unique patient guides are manufactured [17]. The reported results claim joint stability in all cases with a minimum range of motion (ROM) of 90° and correct mechanical alignment with the hip-knee-ankle line passing through the central third of the knee in all cases.

Nuntley et al [16] evaluated 150 patients who had a primary TKA, establishing three cohorts (50 subjects each) for further comparison. In group 1 conventional or traditional instrumentation was used, in group 2 the SIGNATURE™ system (Biomet, Inc, Warsaw, Indiana) was used for a mechanical restoration approach [30], while group 3 the patient-specific OtisMed™ (OtisMed™ Corp, Alameda, California) system was used for a kinematic approach [31]. The results of groups 1 and 2 are similar with more varus¹ outliers than group 3, which had more valgus outliers than either group 1 or 2. Therefore, the authors claimed that additional studies are needed to determine whether patient-specific instrumentation improves clinical functions and overall alignment outcomes [16, 30 and 31]. Stronach et al [32] show data for a consecutive series of 58 knee replacements assisted with PSI compared to a historical group of 62 consecutive primary TKAs performed with conventional instrumentation. The authors found no statistically significant difference in component alignment for femoral flexion, femoral and tibial varus/valgus angles, mechanical alignment or posterior tibia slope. They concluded that TKA assisted by customized instrumentation did not improve the overall outcome of the procedure. In particular, they found that the average tourniquet time in the PSI group was 58.8 minutes, while the regular surgery group had an average tourniquet time of 57.0 minutes; the average volume of blood lost was also very similar: 114 ml in the regular group and 111 ml in the assisted by PSI group.

DeHaan et al [33], reviewed 356 TKAs between July 2008 and April 2013; 306 of these surgeries were assisted by patient specific guides, while 50 patients received a traditional surgery. The aim of the study was to evaluate whether or not customized instrumentation leads to decreased perioperative morbidity when compared to standard procedure; they also evaluated the technology cost and the sizing accuracy of the predicted pre-operative plans. The authors reported a reduction of 20.4 minutes when assisting the surgery with unique

¹ Varus and valgus concepts refer to the frontal plane or coronal alignment of the lower limbs structure, is the inward or outward orientation of the lower limb [31]

instruments; in addition, the predicted femoral sizes were correct in 74.3% of the cases, and 90.4% for the tibial component [33]. However, there is one important limitation to this study: the experiment is not randomized and the group of customized guides is nearly five times the number of patients in the traditional procedure group.

In contrast, a randomized study was conducted by Hamilton et al [34] with 52 patients equally distributed between a conventional surgery group and a patient specific instrumented surgery group. In this case, the average total surgical time was not shortened by the use of unique patient instruments, with an average surgery completion time of 61.8 minutes, while the conventional method group completed the surgery in an average of 57.4 minutes. In addition, no significant differences with respect to mechanical alignment, measured radiographically, were also reported, but the patient specific technique did reduce the number of instruments used in surgery [34]. Ivie et al [35] concluded that the outcomes of patient specific total knee replacements were generally improved when compared to the results from a typical knee replacement surgery. This study was conducted for a cohort of 100 patients who underwent TKA surgery with patient matched instrumentation (PMI), and compared with a group of 100 patients who had already received conventional surgery by the same orthopedic surgeon. Results demonstrated that the improvement obtained by the PMI group in the varus-valgus alignment for the femoral component was 1.5 times more likely to be within the $\pm 3^\circ$ of deviation from the neutral axis of the component; similar results for the mechanical axis alignment measurements indicate that PSI TKAs were 1.8 times more likely to be within the $\pm 3^\circ$ of the desired deviation from the neutral mechanical axis. Figure 2.1.3 provides evidence of the results observed.

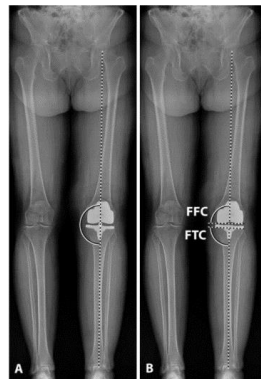


Figure 2.1.3. Standing coronal radiographs after total knee replacement was conducted assisted by patient specific instrumentation. (A) Measurement of the limb mechanical axis, (B) measurement of the femoral component (FFC) and the frontal tibial component (FTC) to determine varus/valgus alignment [35]

Although the results reported in several studies have been inconsistent, utilization of patient specific instrumentation is estimated to have become 1.5 times more common, as reported between 2011 and 2012. Approximately 82 556 total knee replacement surgeries were performed in 2012 using devices from seven orthopedic implant manufacturers and their patient specific instrumentation [2], however, no proven clinical benefit and minimal literature are yet available [34]. Table I shows a comparison between six manufacturers in 2011 and 2012.

TABLE I. NUMBERS IN VOLUME OF TOTAL KNEE REPLACEMENT ASSISTED WITH PATIENT SPECIFIC INSTRUMENTATION. CASES FROM 2011 AND 2012, ADAPTED FROM [36]

| Company name (alphabetical order) | PSI TKA Global 2011 | PSI TKA Global 2012 |
|--|----------------------------|----------------------------|
| Biomet | 11 192 | 22 506 |
| DePuy – Synthes | 6 000 | 16 000 |
| Medacta | 4 600 | 6 200 |
| Smith & Nephew | 19 500 | 22 000 |
| Wright Medical | 1 600 | 2 000 |
| Zimmer | 9 800 | 13 850 |

Summarizing the incongruences mentioned above from different studies, it is generally accepted that the use of patient specific instrumentation can potentially improve total knee replacement outcomes in the future; not just in terms of component alignment but also from a cost savings and reduced surgery time standpoint, which eventually could represent savings to hospitals [2, 33] and therefore patients. Finally, it is important to compare conventional techniques with different computer assisted methods other than patient specific instrumentation and evaluate the results. More specifically, table II presents an overview of the results reported when conventional TKA and computer assisted surgeries were compared in several studies between 2000 and 2011 [26]. However, it must be noted that the purpose is not to compare the results from general computer assisted navigation (CAN) methods and patient specific instrumentation, as is considered out of the scope of the present work. Comprehensive studies related to different techniques in computer assisted orthopedic surgery can be found in the literature [20, 37].

TABLE II. CORONAL ALIGNMENT OUTLIERS OF PARTIAL REPORTED OUTCOMES IN CONVENTIONAL AND COMPUTER ASSISTED TOTAL KNEE REPLACEMENT SURGERIES. FOR FURTHER REFERENCE OF THE STUDIES PRESENTED BELOW [26].

| Year | Number of studies | Number of navigated TKAs | Navigated outliers > $\pm 3^\circ$ | Percentage of navigated outliers | Number of standard TKAs | Standard outliers > $\pm 3^\circ$ | Percentage of standard outliers |
|------|-------------------|--------------------------|------------------------------------|----------------------------------|-------------------------|-----------------------------------|---------------------------------|
| 2000 | 1 | 15 | 0 | 0.0 | 15 | 5 | 33.3 |
| 2001 | 2 | 55 | 9 | 16.4 | 55 | 15 | 54.0 |
| 2003 | 2 | 132 | 0 | 0.0 | 133 | 21 | 15.8 |
| 2004 | 7 | 333 | 16 | 4.8 | 334 | 86 | 25.8 |
| 2005 | 10 | 743 | 81 | 11.0 | 865 | 313 | 36.2 |
| 2006 | 3 | 199 | 65 | 32.7 | 166 | 77 | 46.3 |
| 2007 | 8 | 682 | 74 | 10.8 | 580 | 142 | 24.5 |
| 2008 | 11 | 985 | 79 | 8.0 | 1022 | 240 | 23.5 |
| 2009 | 5 | 305 | 34 | 11.3 | 304 | 75 | 24.7 |
| 2010 | 2 | 100 | 7 | 7.0 | 96 | 37 | 38.5 |
| 2011 | 3 | 133 | 13 | 9.8 | 97 | 27 | 27.8 |

Conversely to total knee replacement, ankle arthroplasty has not been fully supported by computer assisted techniques such as pre-operative navigation systems and patient specific guides design. To date, only a few reports exist regarding the use of patient specific instrumentation in the Total Ankle Replacement [18, 38]. In more detail, the work from Berlet et al [18] reports a novel method to validate the use of a navigation system for total ankle replacement. As shown in Figure 2.1.4, the aim is to evaluate repeatability of the tibia and talus alignment guide placement and deviation from the preoperative navigation plan. They reported mean variations less than 3° for each degree of freedom (DOF) for the tibia and talus alignment blocks.

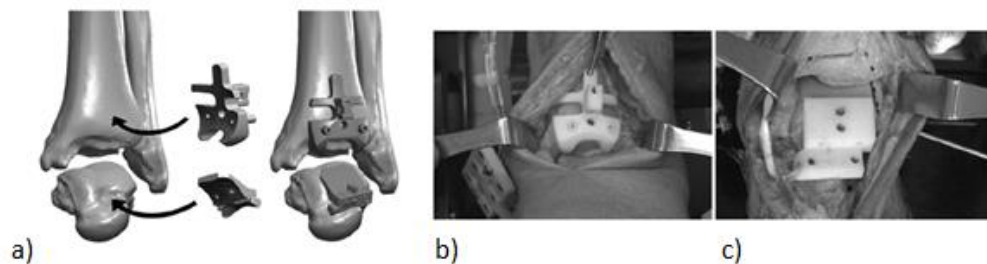


Figure 2.1.4. PROPCHECY® INBONE® tibia and talus alignment guides onto the bone model surface (a) and cadaveric testing of each instrument placement, tibia (b) and talus (c). Adapted from [10]

The largest variation reported in the tibia alignment guide was the internal/external rotation (transverse plane), which was still less than 1° ; the medial/lateral translation (frontal plane)

represented the largest error for the talus guide placement (less than 1 mm). The mean variation between the preoperative navigation report and the final position of the implants, INBONE® Total Ankle System (Wright Medical Technology, Arlington, Tennessee) was reported to be less than $\pm 3^\circ$ [18].

2.2 Historical Use of Sensing Technology in Total Joint Replacement

In vivo data from orthopedic applications of sensor technology was first documented in the 1960s when forces, pressure and temperature were recorded for instrumented femoral head implants and for instrumental correction of scoliosis [39, 40]. These sensing systems have shown a remarkable evolution from the early days of strain gauges connected through percutaneous leads into today’s wireless systems with telemetry and powered passively [41]. Figure 2.2.1 depicts the evolution of “smart” or instrumented implants.

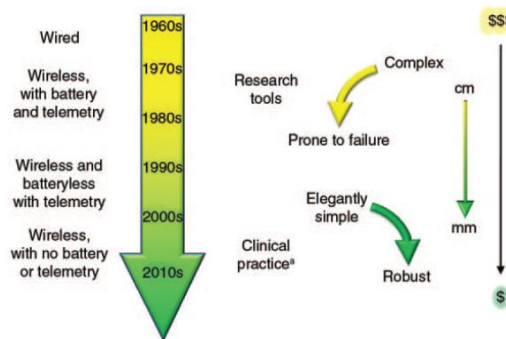


Figure 2.2.1. Smart implant evolution illustration. Adapted from [41]

Although smart implants have been used exclusively as research tools [41, 42] they have provided critical data, improving implant design and characterizing in vivo physical environment. It is well known that stresses and strains are major factors influencing bone growth, remodeling and repair of the musculoskeletal tissues [42]. More importantly, sensing technology applied to biomechanics has been critical to gain insight into the complex structures of bones and joints; thus, it has made possible a better understanding of the mechanical interactions between bones, cartilage, ligaments, muscles and tendons [43-54]. In more recent work, additional benefits for instrumented implants have been mentioned, such as identify implant misalignment, implant loosening, and component wear [54]. Moreover, the authors mention another potential use of the instrumented knee, which is soft

tissue balancing assistance during implantation surgery. They claim that an instrumented tibial tray can provide direct feedback to the surgeon as to whether the knee is properly balanced or not [49]. In addition, Almouahed et al [55] mentions the importance of collateral ligament balancing to ensure an even load distribution in the two compartments of the tibio-femoral joint.

Westerhoff et al [56] developed an instrumented shoulder joint implant based on the Bio-Modular® Shoulder System (Biomet Inc. Warsaw, Indiana). The aim of the work was to measure contact forces and moments acting in the glenohumeral joint. They reported loads of approximately 40% body weight (BW) in an abduction motion of 45°, one week after surgery. They also claimed that the results were similar to previous mathematical studies. Another study was conducted by Bergmann et al [57] to gain precise knowledge of in vivo loads in the shoulder joint. The instrumented shoulder prosthesis was equipped with 9-channel telemetry system, 6 strain gauges and an inductive power supply. They reported the highest peak load in one patient positioned in forward flexion ($>90^\circ$) and 2 kg extra weight, and it reached 238% BW. Figure 2.2.3 depicts the novel instrumented shoulder prosthesis implanted in 6 patients.

As previously discussed, the knee joint is one of the most important joints in the musculoskeletal system and is one of the most analyzed and studied mechanisms [58]. Several studies have been conducted to measure in vivo loads in the knee joint [46-49, 55, 57-61]. Kutzner et al [54], reported average in vivo peak loads of 356% body weight (BW) during stair descent as the highest load condition for the knee joint. These results were obtained by using an instrumented knee implant on 5 subjects. The overall results for the resultant tibio-femoral contact force presented in this work are lower compared to those predicted by many mathematical models. Erhart et al [58], used an instrumented knee implant to assess changes in the medial compartment of one single patient through in vivo measurements. The subject was also equipped with a load modifying variable stiffness shoe. The authors determined that the special shoe helped reducing the medial peak load by 22%. Anderson et al [59], described a novel method for measuring knee forces in vivo for 11 patients. A thin (0.2 mm) flexible electronic pressure sensor was developed and inserted in the medial compartment. The results showed large variations in the force reading, but no "unloaded" state could be detected. In addition, the work of Arami et al, [62] used smart implants

to measure *in vivo* interaction forces in the knee joint. The authors chose anisotropic magneto resistance (AMR) sensors to estimate joint orientation; the magnet was placed in the femoral component while the AMR sensors were inserted in the polyethylene. In order to measure contact forces on the joint, strain gauges were custom designed and fabricated to be inserted into the polyethylene insert. A revision knee implant was also instrumented for *in vivo* characterization of the replaced joint [48]. The authors reported average peak tibial forces of 2.2 % BW on day 6 after surgery; also, they reported an increment of 0.6 times the body weight in climbing stairs activity after 6 weeks of recovery. More recently, a novel sensing device has been developed by Homberg et al [63]; a tibia tray powered internally by an integrated piezoelectric energy harvesting system. The most interesting feature about this device is the self-harvesting energy system, based in the piezoelectric effect. The system entirely powers all the sensor's systems and the wireless circuits. The authors claimed that a subject of 55 kg can fully charge the storage capacitors in 11 steps; the total energy harvested per step is reported to be 1051 μJ . On average, *in vivo* results reported from smart implants are realistic measurements of the interactions between the structural elements conforming the musculoskeletal joints [50, 60]. Figure 2.2.2 depicts a total knee system with instrumented tibia tray.

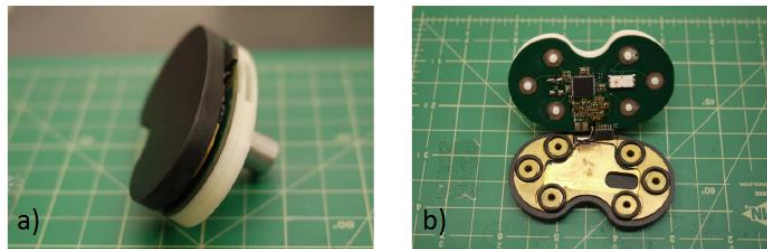


Figure 2.2.2. Instrumented tibia component with self-harvesting system, full assembled device shown in a) and circuit board along with sensors layout in b). Adapted from [63].

Similar results have been reported for the hip joint [43, 51-53, 60, 65-68]. Table III summarizes a short sample of those results. Moreover, considerable amount of literature exists concerning *in vivo* experiments for evaluating contact forces in the hip joint [52].

TABLE III. SHORT SUMMARY OF EXPERIMENTAL STUDIES CONDUCTED IN VIVO FOR EVALUATING RESULTING CONTACT FORCES IN THE HIP JOINT

| Study | No. of subjects | highest peak loads (BW) | Activity |
|---------------------|-----------------|-------------------------|--|
| Rydell [39] | - | 3.50 | Dynamic walk |
| English et al [53] | 1 | 3.59 | One-legged stance 126 3.59 pelvis tilted up with hand support. |
| Davy et al [52] | 1 | 2.80 | Stair climbing |
| Bergmann et al [64] | 1 | 8.70 | Stumbling |
| Brand et al [72] | 1 | 3.50 | Freely walking at selected speed |
| Bergmann et al [65] | 4 | 11, 000 N | Stumbling |

Furthermore, vertebral body replacements and lumbar spine sensors have also been instrumented in several studies [69]. Telemeterized vertebral body replacements have been implanted in three patients by Rohlman et al [69]; the results show interesting findings regarding the load conditions on spine during several exercises in the first month postoperatively. The authors report peak load forces of 450 N when standing and sitting; 420 N when upper body is flexed; and 700 N when additional weight in the hands is supported. Graichen et al [57] developed a miniaturized 9-channel telemetry transmitter, capable of measuring different and complex loading situations (shoulder, vertebral replacement and hip) during different activities, which is shown in Figure 2.2.3. The authors claim some advantages of this device over previous versions, a few of them are: less power consumption, hermetic sealing of all components inside the implants which therefore allows long term data transmission and electronic integration within a custom-made chip designed and built from semiconductor technology (bipolar complementary metal oxide semiconductor, BiCMOS). The limitations found are related to low efficiency of the inductive power supply at distances over several centimeters, as well as the RF transmission data is limited to less than 50 cm. This device has been implemented on shoulder prosthesis from three different patients, as shown in figure 2.2.3a). However, the authors also implemented this transmitter on instrumented proximal tibia trays and vertebral body replacement as well [57].



Figure 2.2.3. Instrumented shoulder endoprosthesis and section view to depict the sensing electronics (a) and Instrumented vertebral body and section model to depict electro-mechanical measurement system (b). Adapted from [57]

Despite the benefits and the relevance of *in vivo* measurements, predicted mathematical and computational models represent a potential tool to improve or create new implants designs [70]. However, for this to become reality, a study directly compared calculated hip joint forces with measured values from instrumented hip prostheses [71]. In this work, two subjects with instrumented implants were analyzed and the results were similar in pattern and magnitude, with average differences of 13.5% in the first subject and 18.1% in the second subject. Brand et al. [72] compared mathematical estimates calculated from laboratory observations with an instrumented hip prosthesis in one patient; the results were reported to be similar at peak loads. Heller et al [66], reported the first cycle-to-cycle validation of predicted musculoskeletal loading for climbing stairs and walking for four patients with instrumented hip implants. The comparison of *in vivo* measurements and calculated (modeled) hip contact forces showed 13% of the relative deviation during walking, while 14% of the deviation occurred during stair climbing. Regarding the knee joint, several researchers have measured external force systems. In 1970 Morrison et al [73], reported, through a mathematical model, a variation from 206% BW to 400% BW in the maximum contact forces of the knee joint. Taylor et al [74] calculated peak force values as high as 620% of BW for one specific patient from their study, using a musculoskeletal lower limb model. Costigan et al [45], conducted a study to estimate hip and knee joint kinetics of 35 young, healthy subjects when climbing stairs, using a subject-specific model for each joint; the result reported for the peak load in the knee joint was as high as 5 times (500%) the body weight. Other studies based on mathematical models have shown variations from 310% up to 800% of body weight peak loads in the knee joint [54]. From a computational approach, different

studies indicate considerable between predicted models and in vivo measured systems for knee and shoulder joints [41, 60, 65 and 75], Table IV below shows the comparison between related works.

TABLE IV. SUMMARY OF EXPERIMENTAL AND MODELED STUDIES REPORTING MAXIMUM *IN VIVO* KNEE FORCES. FOR DETAILS ABOUT THE STUDY'S AUTHORS, REFER TO THE FOLLOWING CITATION [62].

| Condition | No. Of studies | No. of Subjects | Average Total Body force (%) |
|------------|----------------|-----------------|------------------------------|
| Overground | 6 | 1 | 2.5 |
| Overground | 2 | 3 | 1.8 – 2.5 |
| Overground | 2 | 1 | 2.1 – 2.8 |
| Overground | 5 | 1 | 2.2 – 3.0 |
| Treadmill | 2 | 1 | 2.1 |
| Treadmill | 1 | 1 | 1.8 – 2.5 |
| Model | 2 | 12 | 2.1 – 3.9 |
| Model | 1 | 2 | 2.2 |
| Model | 2 | 4 | 2.7 – 3.8 |
| Model | 1 | 10 | 2.9 – 3.5 |
| Model | 12 | 1 | 3.9 |

Conversely to these results, computational models for the hip joint have shown better results between predicted models and experimental data [60, 71 and 72]. Though not yet perfected, smart components hold great promise for helping overcome the uncertainties of prediction models and to provide realistic data to improve implant designs and alignments [34, 45, 55, and 76-78].

2.3 Problem Description

The procedure patients undergo when a total ankle replacement is performed, strongly depends on the system (different by each company) used by the surgeon [10]. The outcome is also strongly related on how well aligned the prosthesis will be set in regard of the ankle and lower limb anatomy. Regardless the system used by the physician, this thesis is focused on the instrumentation designed specifically for each patient based on their own specific anatomy, and the problem statement is found on evaluating how those instruments actually fit onto the bone surface.

Despite the fact that instruments are designed to fit on the bone in only one particular spot, there is a risk of misaligning the contact surfaces. Therefore, the claim of this work is to design a thin film piezo electric sensor that can adopt the interface area and determine the pressure map of the contact surface. Consider Figure 2.3.1b), the piezo sensor will be placed

in between the instrument and the bone surface, forcing the film to adopt the contact area surface. Using direct piezoelectric film will produce an electrical potential difference when the film experiences mechanical deformation and the corresponding stress distribution will produce a correlated voltage distribution that can be collected and read to understand the magnitude of the mechanical stress.

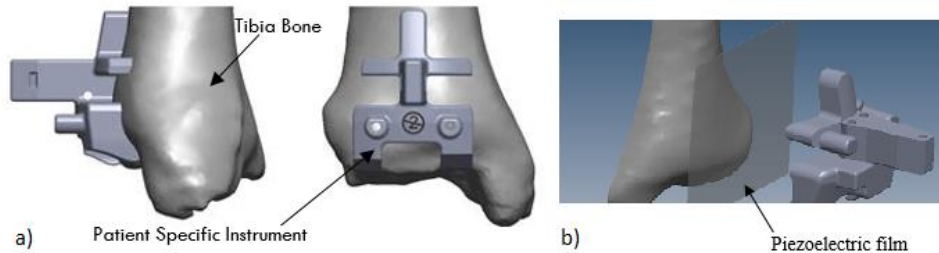


Figure 2.3.1. CAD model representation of patient specific instrumentation and the corresponding fit onto the bone surface. a) Illustration of how the instruments are placed onto the surface, b) oblique view depicting proposed thin film sensor to adopt bone-instrument contact surface. Images developed by the author.

In Figure 2.3.1 the contact area is depicted for the tibia bone, as well as a representation of the thin piezo film that will be designed to achieve the mechanical deformation needed to adopt the contact interface between the bone surface and the instrument. In addition, figure 2.3.2 shows the actual instrument being pressed onto a printed bone model with a thin ($25\mu\text{m}$) polyamide substrate in between; representing the desired configuration of the sensor.

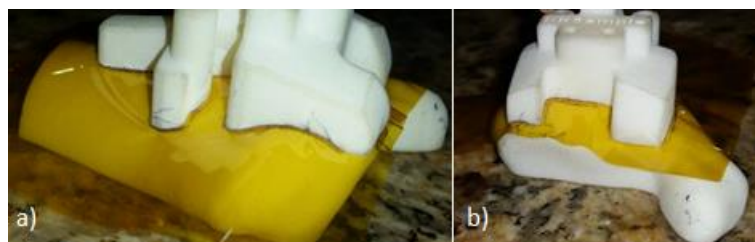


Figure 2.3.2. Actual instrument and 3D printed bone model with a polyamide film in the contact interface, a) oblique lateral view and b) oblique bottom view.

A first evaluation of the problem statements indicates a challenge from both design perspectives: *mechanical and electrical*. In terms of the mechanical design, the challenge is oriented in determining the correct piezo thickness and material, as well as other components materials and dimensions, such as the substrates, adhesives and conductive layers; the correct selection of these materials will ensure the correct mechanical behavior of the sensor avoiding plastic deformations that will prevent sensor breakage or misreadings.

Regarding the electrical design, material selection is also an important milestone to achieve as it will determine the output signal that can be acquired by the system. In addition, the electrical design must be capable of sensing as much of the contact area is possible in order to obtain a pressure map that truly resembles the actual contact between the bone and the instrument.

2.4 Contact Mechanics Foundations

Contact mechanics theory can be studied by different approaches, however, the overview to be discussed in this section will be mainly focused on describing contact mechanics theory and how the application fits in that scenario, from an analytical standpoint.

Before moving forward with the contact problem definition within the scope of this thesis, an important difference must be established between conforming and non-conforming types of contact. The first case occurs when the contact surfaces from two objects fit on each other or if the profiles follow a similar curvature; whether a non-conforming type of contact is that where the two surfaces interacting have different profiles. Figure 2.4.1 shows a schematic of the interaction of non-conforming and partially conforming surfaces.

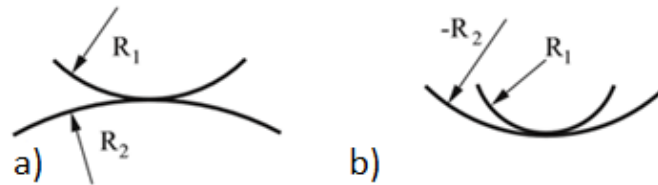


Figure 2.4.1. a) Non-Conforming curved contact surfaces. b) Partially Conforming Contact surfaces.

For the linear strain theory of elasticity to be applicable for contact problems, the deformation of the bodies at the region of contact has to be small enough when compared to the entire body dimensions. Moreover, for non-conforming contact the region at which the two bodies interact will have a small area compared to the curvature radio of the un-deformed surface, as it can be depicted as well from Figure 2.4.1a). The contact stresses will therefore be highly concentrated at the contact region and will rapidly decrease as we increase the distance from the point of contact, so the area of interest lies close to the contact interface [79]. Since the goal of this overview is to characterize the contact problem that arises when the patient

specific instrumentation is pressed onto the bone surface (see figure 2.3.1), this chapter will be focused on providing the analogy between the application and the theory found for contact mechanics.

As stated earlier, the region that occupies our interest is close to the contact interface of the two elastic bodies, however, describing high level of detail for the mechanical stresses around the contact area is also of particular importance since they will be input for the piezoelectric device and the sensor response. Understanding the mechanical behavior is crucial for an appropriate sensor design in terms of material selection and geometry dimensioning. To continue with the study of contact nature between the instrument and the bone (see Figure 2.3.1), there are two interactions responsible for the contact transmission, the normal pressure $p(x)$ and the tangential traction or frictional force $q(x)$, which can be depicted in Figure 2.4.2. The normal and shear stresses are, as consequence, result from the normal pressure and tangential or friction force respectively. It can be shown that the stress components for any point A can be found as well as the displacement of any point C when evaluating an elemental area of width ds and located at s distance from the origin, as follows:

$$\sigma_x = -\frac{2z}{\pi} \int_{-b}^a \frac{p(x)(x-s)^2 ds}{\{(x-s)^2 + z^2\}^2} - \frac{2}{\pi} \int_{-b}^a \frac{q(s)(x-s)^3 ds}{\{(x-s)^2 + z^2\}^2} \quad (2.4.1)$$

$$\sigma_z = -\frac{2z^3}{\pi} \int_{-b}^a \frac{p(x) ds}{\{(x-s)^2 + z^2\}^2} - \frac{2z^2}{\pi} \int_{-b}^a \frac{q(s)(x-s) ds}{\{(x-s)^2 + z^2\}^2} \quad (2.4.2)$$

$$\tau_{xz} = -\frac{2z^2}{\pi} \int_{-b}^a \frac{p(x)(x-s) ds}{\{(x-s)^2 + z^2\}^2} - \frac{2z}{\pi} \int_{-b}^a \frac{q(s)(x-s)^2 ds}{\{(x-s)^2 + z^2\}^2} \quad (2.4.3)$$

The expressions (2.4.1), (2.4.2) and (2.4.3) describe the normal and shear stresses components for any contact problem with force distributions as depicted in Figure 2.4.2, which represents an elastic half-space loaded over a strip (length $a + b$). Although mathematically challenging, these integrals can be solved if the normal and tangential force distributions are known, allowing to find the stress distribution close to the contact interface. Nevertheless, knowing these exact force distribution is not always practical, and more

general methods are needed to evaluate the nature of the contact problem raised from the bone-instrument interaction.

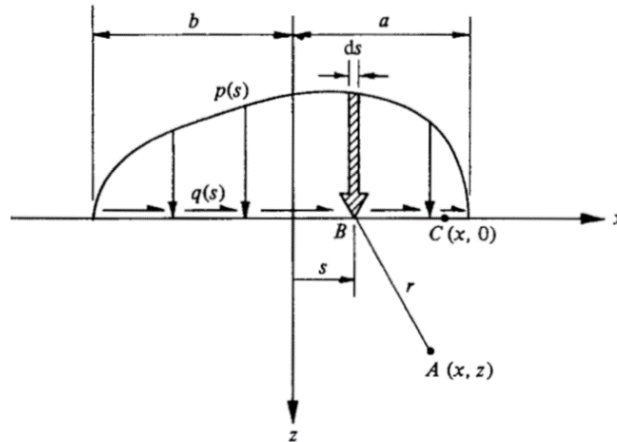


Figure 2.4.2. Normal and tangential components acting on the contact interface [79].

Studying the Hertz normal contact problem of elastic solids is an interesting approach of approximating the analytic solution for the maximum pressure given at the bone-instrument interface. The Hertz theory is suitable when dealing with elastic models and when the following assumptions are established:

1. The contact area (A) is small relative to the dimensions of each body of the contact interaction, and to the relative radii of curvature of the contact profile or contact radius (R). These assumptions also mean that the surfaces must be non-conforming and continuous, which is accomplished if the contact area is significantly small relative to the radii of curvature of the contact profile ($A \ll R$)
2. The strains produced by the contact interaction must be small.
3. Each solid can be considered as an elastic half-space. This means that the contact area (A) is significantly small when compared to the curvature radius of each body (R_1, R_2).
4. The friction component along the contact area can be neglected and the interaction is considered frictionless.

In general, real engineering applications dealing with contact between two bodies are highly non-linear and modeling the contact as a problem between elastic bodies might not be appropriate for all scenarios. In fact, contact analysis of non-linear plastic or permanent deformations are typically solved numerically through computational tools. Nonetheless, for

an initial and theoretical approximation, all of the above assumptions might be considered into the contact problem between the bone and the patient specific instrument (Figure 2.3.1c) in order to establish a baseline or a comparison for the upcoming computational analysis. As it has been stated earlier in this chapter, the maximum contact pressure and the associated stress are the goals of this construction. Applying the Hertz theory, the maximum pressure can be calculated as [80],

$$p_0 = \frac{2}{\pi} E^* \left(\frac{d}{R} \right)^{1/2} \quad (2.4.4)$$

where d is the contact displacement or indentation, R is the contact radius and E^* is the equivalent modulus of elasticity, calculated Eq. (2.4.5):

$$E^* = \frac{1 - \nu_1^2}{E_1} + \frac{1 - \nu_2^2}{E_2} \quad (2.4.5)$$

where ν_1 and ν_2 are the Poisson ratios for each body, while E_1 and E_2 are the Young's Modulus for each body as well. Moreover, the Hertz theory also finds the normal force applied to the elastic half space as follows,

$$F = \frac{4}{3} E^* R^{1/2} d^{3/2} \quad (2.4.6)$$

Combining Eq. (2.4.5) and Eq. (2.4.6), the maximum pressure can be obtained in terms of the applied normal force, as shown in Eq. (2.4.7) below,

$$p_0 = \left(\frac{6FE^{*2}}{\pi^3 R^2} \right)^{1/3} \quad (2.4.7)$$

The results from Eq. (2.4.7) can be evaluated in two dimensional slides (“zx” plane) from the bone-instrument CAD model, as depicted in Figure 2.4.4. Therefore, a maximum pressure value can be obtained for different cut slides in the “y” direction, allowing to compare an

analytical approach from the results of computational analysis which will be described in the following sections.

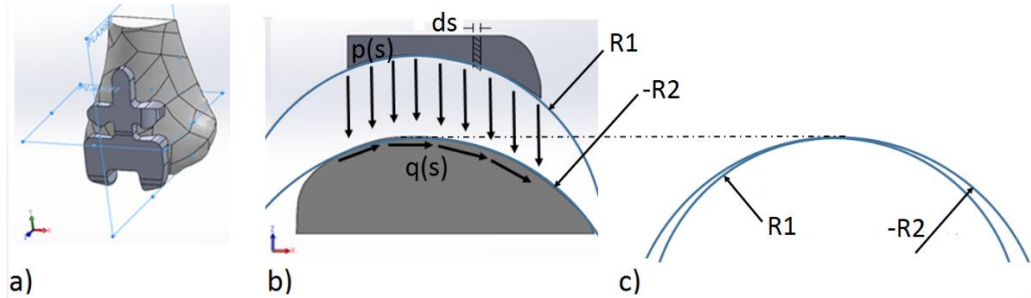


Figure 2.4.3. a) CAD 3D models of the bone and the simplified patient specific instrument, b) two dimensional view in the zx plane of the interactions responsible for the contact transmission: the normal pressure $p(s)$ and the tangential traction or frictional force $q(s)$ and c) contact approximation of both curvatures.

According to Figure 2.4.3c, the contact problem in the zx plane can be classified as “partially conforming”, allowing the use of Hertz theory for the analytical approach. When using this method, a proportional relationship must be obtained for the equivalent radius used in Eq. (2.4.7), which can be calculated through Eq. (2,4,8), as follows [80],

$$\frac{1}{R} = \frac{1}{R_1} + \frac{1}{R_2} \quad (2.4.8)$$

Figure.2.4.3a) shows a simplified CAD model of the patient specific instrument, this is done to simplify the model geometry and thus the meshing process in the Finite Element Analysis presented in section 3.4.

The purpose of showing only one slide in the zx -plane, as depicted in Figure. 2.4.3b), is to obtain an analytical approximation through the Hertz contact theory and the Eq. (2.4.4) to Eq. (2.4.8). Figure4.3.3c) denotes the interaction between the two radii as a partially conforming type of contact. The negative sign is for the larger radii.

2.5 Piezoelectricity Foundations

Piezoelectricity is the result of linear coupling between electrical and mechanical interaction among certain materials that exhibit a piezoelectric response [81]. Direct piezoelectric effect

refers to the electric response caused by mechanical deformation, whereas indirect effect means the opposite: a mechanical deformation or strain produced as a result of an applied electric field. Piezoelectric effect can also be seen as energy transfer between mechanical and electrical energy [82].

For a material to exhibit piezoelectric effects, the crystal structure must have no center of symmetry, while also containing charged particles that can be rearranged by the effects of polarization. Examples of materials exhibiting these properties are: lead zirconate titanate (PZT), zinc oxide (ZnO), quartz, polyvinylidene difluoride (PVDF) and more recently, ferroelectric/piezoelectric copolymers with trifluoroethylene P(VDF-TrFE) [83].

In the case of PVDF and copolymers, the piezoelectric response is obtained when exposing the material to a high electric field after a mechanical stretching has been applied, or after a machining process [82]. As expected, depending on the direction of the mechanical interaction, the piezoelectric effect might change. For instance, a uni-axial stretching will result in uni-axial piezoelectric effect, while a bi-axial stretching will result in bi-axial and isotropic piezo response in the plane. Because the scope of this work is to measure the pressure being applied across the thickness of a thin piezo layer, the truly important direction is perpendicular to the in-plane layer, being the d_{33} coefficient the responsible for obtaining a signal from the sensor. To better describe this scenario, Figure 2.5.1 shows a uni-axial piezoelectric film that was machined (stretched) in the 1-direction.

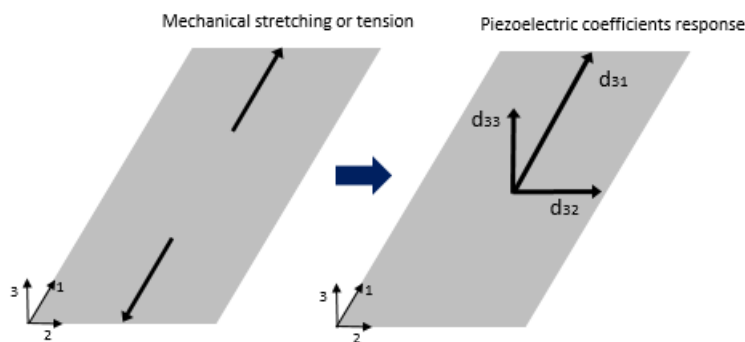


Figure 2.5.1. Uni-axial film being stretched in the 1 direction and the corresponding piezoelectric response.

Among the materials mentioned previously, PZT, zinc oxide and the quartz will not meet the flexibility requirement that the application demands. It is well known that despite the high piezoelectric response of these materials, the mechanical behavior is mainly brittle and the amount of tensile stress produced by high flexural moments is not very high, limiting the

possibility of adopting an irregular surface such as bone or patient specific instrumentation, as shown in Figure 3.2.2. Therefore, it can be stated that the mechanical response in terms of flexibility is the limiting factor when choosing the piezoelectric material. Thus, the biggest challenge for the piezo film is to withstand the mechanical deformation while still being able to deliver the corresponding output voltage.

To satisfy these requirements, the PVDF and the copolymers materials are the only options available. However, Table IV shows a comparison between PVDF (uni and bi-axial), PZT and Copolymer materials. PVDF and P(VDF-TrFE) copolymer offer better mechanical response with considerable smaller piezoelectric response relative to PZT, however, the mechanical properties are crucial for meeting the application requirements. Between PVDF and the copolymer, the former shows better piezoelectric response in the 33 direction; in addition, PVDF is easier to obtain from a commercial standpoint. Therefore PVDF is a more suitable material for the application. Moreover, PVDF biocompatibility has been widely proven [82], which complies with the medical device industry requirements.

TABLE V. COMPARATIVE TABLE BETWEEN COMMERCIAL PZT, PVDF AND P(VDF-TrFE) PIEZO ELECTRIC FILMS. EXTRACTED FROM [19 AND 86]

| Material properties | PZT | PVDF | | P(VDF-TrFE) Copolymer 75/25% |
|--|------|-----------|----------|---------------------------------|
| | | Uni-Axial | Bi-Axial | |
| Piezoelectric constants | | | | |
| d_{33} (pC/N) | 300 | -25 | -25 | 16 |
| d_{31} (pC/N) | -150 | 15 | 3 | 6 |
| d_{32} (pC/N) | -150 | 3 | 3 | 6 |
| Relative permittivity ϵ/ϵ_0 ($\epsilon_0 = 8.854 \times 10^{-12}$ F/m) | 1800 | 12 | 12 | 9.4 |
| Young's modulus (GPa) | | | | |
| Y_1 | 50 | 3 | 3 | 0.9 |
| Y_2 | 50 | 1 | 3 | 1.5 |
| Y_3 | 50 | 10 | 10 | NA |
| Maximum stress in traction (MPa) | | | | |
| direction 1 | 80 | 200 | 200 | 150 |
| direction 2 | 80 | 40 | 200 | 30 |

Generally, piezoelectric constitutive equations can be written in terms of the sensing mode or in terms of the actuation mode. Given the scope of this thesis, and in terms of the direct piezoelectric effect, the coupled constitutive equation for the sensor mode can be read as

$$\{D\}_{3 \times 1} = [d]_{3 \times 6} \{T\}_{6 \times 1} + [\epsilon^T]_{3 \times 3} \{E\}_{3 \times 1} \quad (2.5.1)$$

Where \mathbf{D} is the electric displacement or polarization, \mathbf{d} the piezoelectric constant matrix, \mathbf{T} the mechanical stress vector, $\boldsymbol{\varepsilon}^T$ the permittivity matrix and \mathbf{E} is the electric field. An element d_{ij} from the matrix \mathbf{d} represents the coupling between the electrical displacements in direction i and the mechanical strain in direction j [81].

Eq. (2.5.1) can be very difficult to resolve through analytical methods and often it requires finite element analysis tools to approximate the solution, as presented in Section 3.5. Nevertheless, the expression can be simplified under certain assumptions [83], for example, when an external tensile force in 1 direction induces a normal stress in the 3 direction, the generated polarity can be expressed as

$$D_3 = d_{31}T_1 \quad (2.5.2)$$

Eq. 2.5.2 can also be adjusted for a normal stress induced by bending moment in the 1-3 direction:

$$D_3 = d_{33}\sigma_{13} \quad (2.5.3)$$

Where σ_{13} is the normal stress induced by the moment. Furthermore, the resulting voltage due to the generated polarity D_3 can be written is given by

$$D_3 = \varepsilon_{33} \frac{V}{t} \rightarrow V = t \frac{D_3}{\varepsilon_{33}} \quad (2.5.4)$$

Where t is the thickness of the piezo layer, V is the equivalent voltage corresponding to the generated polarity, and ε_{33} is the dielectric constant in the 3 direction, however, for the PVDF this property is isotropic and therefore equivalent in all directions. Thus, Eq. (2.5.5) returns the value of dielectric constant expressed in terms of the vacuum permittivity constant,

$$\varepsilon_{33} = \varepsilon * \varepsilon_0 \quad (2.5.4)$$

where ϵ_0 is the permittivity in the vacuum or the permittivity of free space and its value is given as $\epsilon_0 = 8.854 \times 10^{-12}$ F/m. For the selected PVDF the ϵ value is 12 at a frequency of 1MHz, as reported by the manufacturer [87]. More details about material properties are addressed in the computational analysis, section 3.4.

When looking at the size of the piezoelectric coefficients matrix from Eq. (2.5.1), it can be noticed that the Table V only shows piezoelectric constants d_{33} , d_{31} and d_{32} . This is due to crystal symmetries found in the materials, resulting in only a few non-zero elements for the coupling matrix [82]. When developing Eq. (2.5.1) in the matrix form, the non-zero elements can be shown as

$$\begin{Bmatrix} D_1 \\ D_2 \\ D_3 \end{Bmatrix} = \begin{bmatrix} 0 & 0 & 0 & 0 & d_{15} & 0 \\ 0 & 0 & 0 & d_{24} & 0 & 0 \\ d_{31} & d_{32} & d_{33} & 0 & 0 & 0 \end{bmatrix} \begin{Bmatrix} T_1 \\ T_2 \\ T_3 \\ T_4 \\ T_5 \\ T_6 \end{Bmatrix} + \begin{bmatrix} \epsilon_{11} & 0 & 0 \\ 0 & \epsilon_{22} & 0 \\ 0 & 0 & \epsilon_{33} \end{bmatrix} \begin{Bmatrix} E_1 \\ E_2 \\ E_3 \end{Bmatrix} \quad (2.5.6)$$

For the recently chosen PVDF piezoelectric film, the coupling matrix $[d]$ has the following typical form:

$$[d] = \begin{bmatrix} 0 & 0 & 0 & 0 & 0 & 0 \\ 0 & 0 & 0 & 0 & 0 & 0 \\ d_{31} & d_{32} & d_{33} & 0 & 0 & 0 \end{bmatrix} \quad (2.5.7)$$

The matrices of piezoelectric coefficients shown in Eq. (2.5.7) are for a specific PVDF film purchased from the company *GoodFellow* under the model of FV301301, 0.110 mm thickness. Chapter 3, section 3.2 presents further discussion about the selection criteria for the thickness of the piezoelectric film.

CHAPTER 3

Flexible MEMS Sensor Design

3.1 Sensor Configuration and Geometry

3.2 MEMS Design

3.2.1 Measurement System for Determining Experimental Contact Force Reaction.

3.2.2 Sensor Thickness Definition.

3.3 Finite Element Analysis of the Contact Problem

3.4 Finite Element Analysis of the thin Piezo Electric Film

3.1 Sensor Configuration and Geometry

As described in Section 2.3, the goal of this research is to design and built a sensor capable of adjusting to a highly irregular contact surface between a patient specific instrument (PSI) and the human bone. Total Ankle Replacement (TAR) is a procedure that mainly affect two bones in the ankle joint: the tibia and the talus, as presented in Figure 2.3.2. However, the sensor geometry will be based only on the tibia bone and therefore the tibia PSI.

The first configuration problem to solve is to determine the sensing area for the application. Despite the fact that there are different bone sizes among different patients, the aim of this thesis is to develop a design that can later be adjusted to various sizes. In this experiment, the sensing area is determined to fit on a printed tibia bone model of a typical size and its corresponding patient tibia specific instrument. These models are courtesy of Wright Medical Technology.

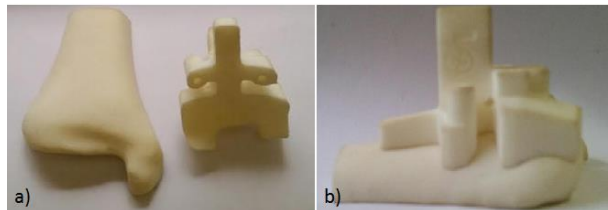


Figure 3.1.1. Models provided by Wright Medical Technology for this application development, a) individual models and b) patient specific instrument placed on top of the bone model to resemble the application.

Considering the models provided and the geometry observed, the dimensions in the frontal plane have been defined by using the CAD model of the instrument, resulting in a sensing total area of 35 mm x 50 mm, as shown in Figure 3.1.2. In addition to defining the total

functional area of the sensor (which it will be capable of reading the applied pressure), it is also important to define the resolution of the resulting signals is going to be. As it will be discussed in Section 3.4, the piezoelectric film will result in different polarization, and therefore different voltage readings, across the plane when submitted to mechanical deformation. These data need to be collected through the sensor electrodes capable of recording such polarization values throughout the piezo. One challenge for the sensor design is determining the pitch and the width of the electrode sensor as well as the entire matrix structure. Figure 3.1.2 shows the proposed design of the electrodes, being an array of nodes forming the matrix of the sensor data.

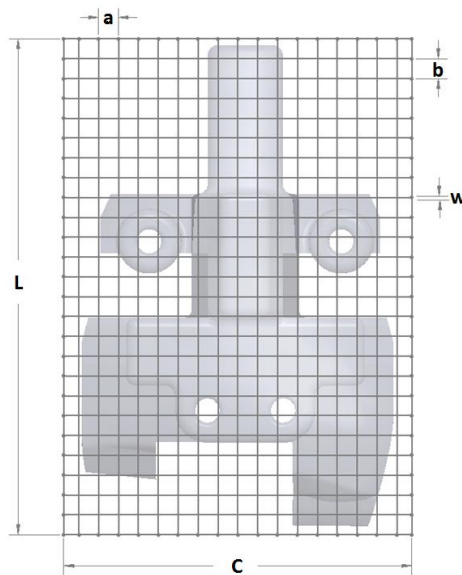


Figure 3.1.2. Proposed sensor node array for collecting data from the piezoelectric film.

How close the electrode traces are to each other is known as the pitch, or distance between each trace center, depicted in Figure 3.1.2 as letter “*a*” for the horizontal pitch and “*b*” for the vertical pitch. The width of these traces is also crucial for the sensor design, because they carry out the electrical response while also withstanding the high normal and shear stresses produced by the mechanical deformation. At this point, there is no data approximation for the mechanical data of the electrical charge that will be carried out by the electrode traces. However, it is expected that stress induced by the mechanical impact is the biggest challenge and the trace width is selected to be as thick as 1.0 mm to provide enough stability to the sensor array. This magnitude will be confirmed in Section 3.2 when more detail about the mechanical analysis is presented.

This matrix sensor structure also gives an important parameter for the sensor, which is known as the resolution or level of detail. By commercial applications, it is well established that a sensor resolution is the amount of nodes by a measure of area. Table VI contains the most relevant information about the sensor geometry and resolution.

TABLE VI. SENSOR GEOMETRY PARAMETERS AND DIMENSIONS.

| Parameter | Letter | Value | Unit |
|--|--------|-------|-----------------------|
| Sensor length | L | 50 | cm |
| Sensor width | C | 35 | cm |
| Horizontal pitch (distance between traces) | a | 1 | mm |
| Horizontal pitch (distance between traces) | b | 1 | mm |
| Copper trace width | w | 1 | mm |
| Sensor Resolution | R | 25 | Nodes/cm ² |
| Number of Horizontal electrodes traces (columns) | - | 17 | - |
| Number of Vertical electrodes traces (rows) | - | 25 | - |

So far, it has been discussed that the piezoelectric sensor has horizontal and vertical electrodes as illustrated in Figure 3.1.2. In more detail, a 3D model of the structure for the sensor is shown in Figure 3.1.3, where the assembly of components follows a specific order of different layers pressed onto each other.

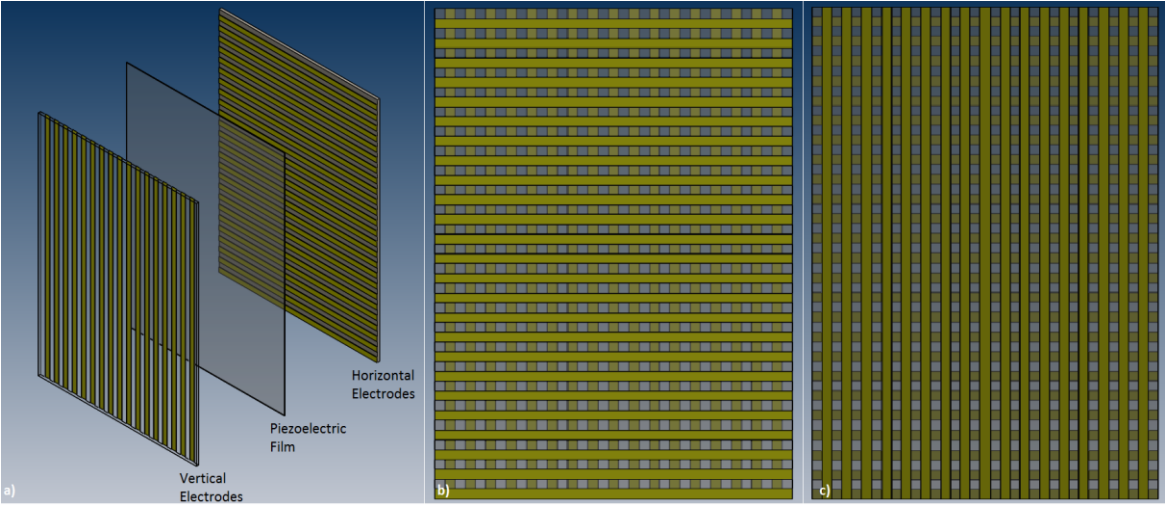


Figure 3.1.3. 3D model of sensor assembly and layer structure, a) exploded view, b) top view and c) bottom view.

As a result, the sensor is structured with a top and bottom electrodes comprised by a layer of polyamide, acting as the flexible substrate on which the copper traces patterns are printed,

followed by a 3M adhesive (3M467) layer in between the copper traces. The piezoelectric film is then pressed by both, top and bottom subassemblies, forming the schematic shown in Figure. 3.1.4.

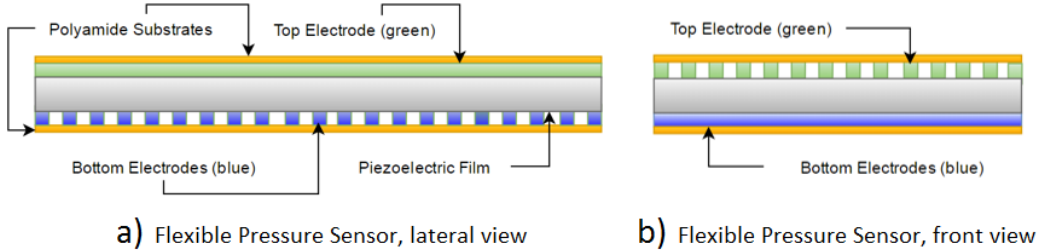


Figure 3.1.4. Flexible pressure sensor structure, a) lateral view where the bottom electrodes are seen as small rectangles in a section view, b) front view where the top electrodes are seen as small rectangles in a section view.

The sensor’s cross section is then formed by different layers, which altogether have a thickness of 0.230 mm. Table VII summarizes the different layer thicknesses of the sensor.

TABLE VII. SENSOR LAYER THICKNESS SUMMARY

| Layer | Thickness (μm) |
|--|----------------|
| Polyamide substrate (top electrode) | 25 |
| Copper and adhesive | 35 |
| PVDF Piezoelectric film | 110 |
| Copper and adhesive | 35 |
| Polyamide substrate (bottom electrode) | 25 |
| Total sensor thickness | 230 |

Through section 3.1, the overall sensor geometry and structure have been discussed. It is important to emphasize, however, that some of the decisions made to this point are to be validated upon the completion of this chapter.

3.2 MEMS Design

It is difficult to predict a reliable analytical value for the amount of stress the sensor is going to experience once the pressure is applied to the instrument. Thus, analogies from the classical mechanical beam analysis are to be conducted in order to determine an appropriate thickness for the sensor and more specifically, for the piezoelectric film.

The first analogy is a simply supported beam with uniformly distributed load, which can be observed by looking a cross section area of the instrument and the bone interface. Figure

3.2.1 shows an equivalent diagram of the force configuration when the instrument is pressed onto the bone, which is ultimately the expected force distribution that the sensor is going to experience. Consequently, the sensor can be analyzed as a beam experiencing a uniform force supported at the two ends.

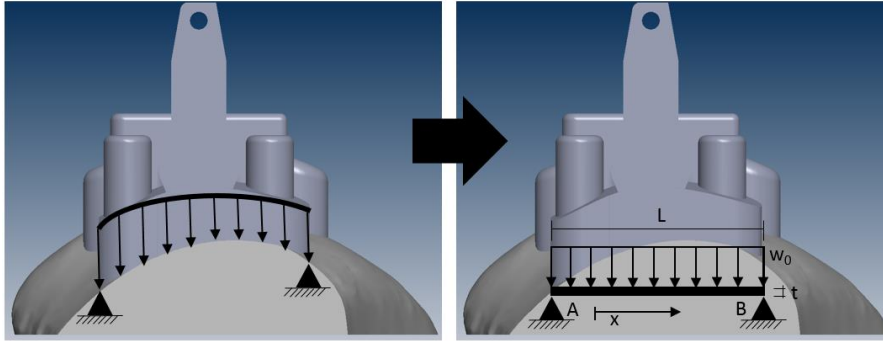


Figure 3.2.1. Simply supported beam with uniformly distributed load analogy

Typically, the static beam analyses are important to determine the appropriate thickness of the material needed for a given application, which is precisely the goal of this section: *to determine an appropriate sensor thickness to withstand the mechanical stress produced by an external pressure*. The higher stress components come from the maximum normal stress induced by the highest moment in the beam. Although shear stress components are also important, the biggest consideration is the bending moment the sensor experiences when the external pressure is applied [84]. From the classic mechanics methods, it can be shown that the moment around B for the beam configuration shown in Figure 3.2.1 is written as,

$$M_B = (R_A x) - \frac{w_0}{2} x^2 \quad (3.2.1)$$

where R_A is the reaction force at the end A of the beam, x is the distance increments from point B to point A and w_0 is the distributed force along the beam. A similar approach can be taken into consideration for evaluating the shear forces acting on the sensor,

$$V_B = R_A - w_0 x \quad (3.2.2)$$

where V_b is the shear force resulting at the end B , while w_0 is the distributed force and x the increment in the horizontal direction.

Prior to solving the moment and shear expression for the simply supported beam, a second analogy is presented at what is assumed to be the most critical section of the instrument in terms of mechanical stress. By examining the contact between the instrument and the bone from a lateral view, a cantilever-like beam can be observed at the distal end of the instrument. Figure 3.2.2 shows how this analogy is visualized, similar to the previous case.

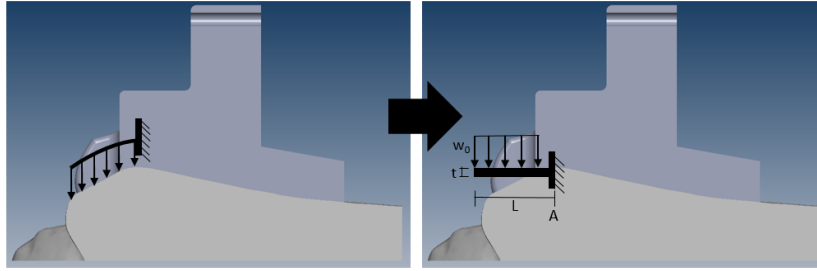


Figure 3.2.2. Beam cantilever fixed at one end analogy.

The moment and shear equations governing this load configuration, are expressed by,

$$M_A = M_0 + \frac{w_0}{2}x^2 - R_A x \quad (3.2.3)$$

where M_A is the moment around point A at the right end of the beam, R_A is the reaction at the fixed end, M_0 is the moment originated by the fixed end, x is the distance increments towards the free end, and w_0 is the distributed force along the beam. Same construction is made to determine the shear forces acting upon the cantilever-like beam.

$$V_B = R_A - w_0 x \quad (3.2.2)$$

Where V_A is the shear force resulting at the end A , R_A is the reaction at the fixed end while w_0 is the distributed force and x the increment in the horizontal direction.

As recently stated, evaluating the moment and the shear forces along the sensor is important to understand the maximum stress the sensor might go through, and then design for a safe value of thickness for the piezoelectric. From the classic mechanical approaches as well [84], it is known that when dealing with a composite beam with layers of different materials, the

whole beam can be analyzed as composed by only one material with the total thickness, by selecting the material with the weaker mechanical properties on the composite. Figure 3.2.3 graphically explains how a beam with multiple layer material can be analyzed as a one layer material.

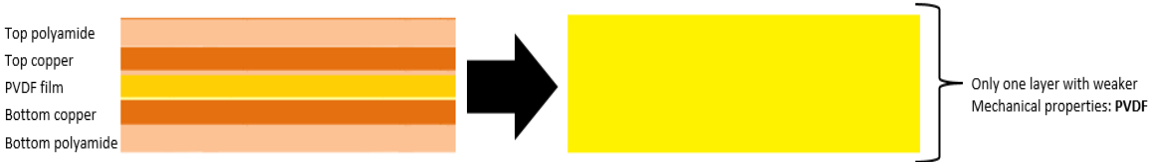


Figure 3.2.3. Composite beam and one layer beam equivalence

Table VIII contains the mechanical properties from the materials selected so far in the sensor assembly. The properties are written to provide evidence of which material needs to be selected as the weaker material to conduct the analysis from this point forward.

TABLE VIII. ULTIMATE TENSILE STRENGTH FOR EACH LAYER ON THE SENSOR ASSEMBLY

| Material | Ultimate Tensile Strength (MPa) | Young Modulus (GPa) |
|---|---------------------------------|---------------------|
| Polyamide Substrate | 231 | 2.5 |
| Copper | 210 | 110 |
| GoodFellow FV301301 0.110 mm thick PVDF | 180 | 1.8 |

Figure 3.2.2 anticipates that the PVDF exhibits the lower mechanical response in terms of the ultimate tensile strength and the Young’s Modulus. Therefore, the rest of the mechanical analysis is conducted by assuming the beam is composed by a homogenous layer of PVDF. This assumption is also highly important when the finite element analysis of the sensor is conducted (section 3.4).

All of the previous analysis cannot be solved without determining the distributed force w_0 that is applied to the instrument when pressed onto the bone, otherwise, the mechanical assembly will be undefined because of the amount of unknown variables. Nevertheless, finding an analytical solution for the maximum force applied can be extremely difficult. Thus, an experiment is conducted to determine an approximate value of the force applied to the system. This experiment is described in Section 3.2.1.

3.2.1 Measurement System for Determining Experimental Contact Force Reaction.

This section is intended to provide a brief description of the experiment conducted to determine an averaged and approximated value for the amount of force that is being transmitted from the user, to the instrument and then to the bone. Eventually, this amount of force is what the sensor should be able to read. More information about the equipment and materials used during this experiment is available on appendix A, as well as the raw data taken by the operators.

A simple experiment was carried out using the patient-specific instrument and the bone model shown in Figure 3.1.1 and a mass analytical scale from the Chemistry Laboratory at the Instituto Tecnológico de Costa Rica (Cartago, Costa Rica). The experimental sequence is listed below for an easy understanding of the procedure.

1. The bone model is placed on top of the scale plate, at the center.
2. The instrument is then gently placed on top of the bone, at the surface matching area.
3. The operator set the scale to zero (tare option).
4. The operator pressed the instrument against the bone model.
5. An evaluation is made by the operator to decide if the model is properly fitting on the bone surface.
6. After the operator is confident the instrument is well placed and additional force is required to keep the instrument in place, the value on the scale is taken.
7. Steps from 1 to 6 are repeated 90 times to provide enough evidence.

Figure 3.2.1.1 illustrates the experiment set up and depicts the results obtained by the operators.



Figure 3.2.1.1. Force approximation experiment –
Image shown from one of the runs performed.

By following the sequence of steps described above, 90 measures of the “mass” value were recorded. While the experiment was conducted to determine the magnitude of the force applied to the instrument, the value recorded is in fact, the mass read by the scale. The value (in grams) that is displayed by the scale in the Figure 3.2.1.1, can be translated into force by multiplying by the gravity acceleration, based on the “weight” acting as a force. Upon completion of the data gathering process, the results were analyzed using Minitab 16.1 software (Pennsylvania, United States). Within the software, a tolerance interval analysis was performed to understand the data behavior; Figure 3.2.1.2 shows the graphical representation of the analysis conducted by the software.

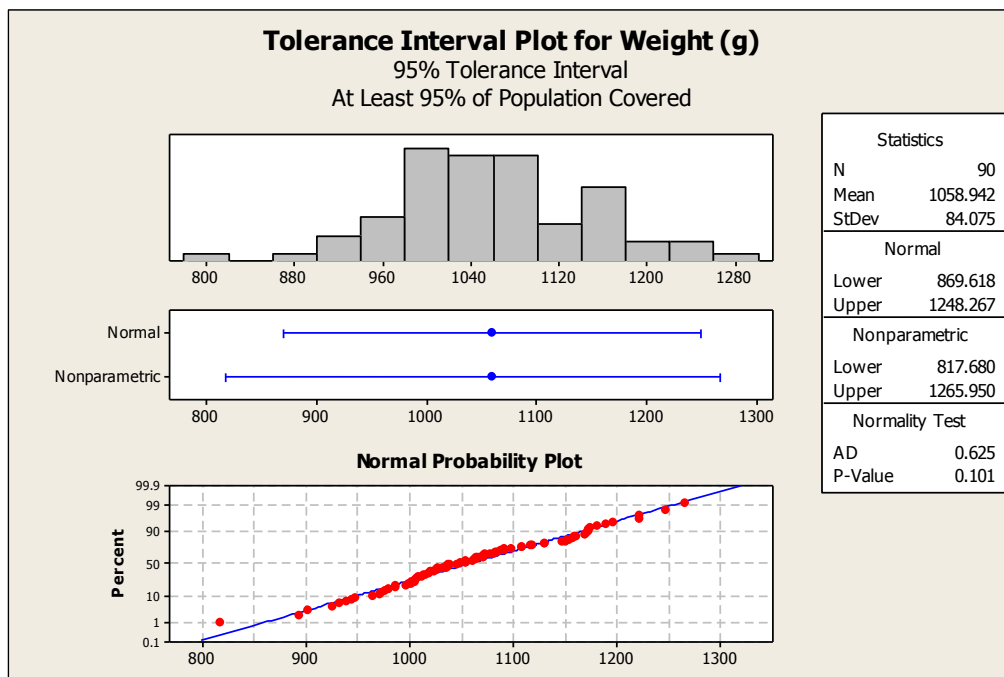


Figure 3.2.1.2. Minitab results from tolerance interval analysis.

The information summarized in Figure 3.2.1.2 provides, with 95% of confidence level, evidence that the mean value for the mass value equivalent to the force acting on the bone model is 1058.942 g, with a lower limit of 869.618 and an upper limit of 1265.950 g. Moreover, the data follows a normal distribution (p value > 0.05) which is an important piece of evidence to support the result of the experiment.

The aim of this study, is to gather evidence to support that a mean value of force can be expressed as,

$$F = ma \rightarrow F = 1058.942g * 9.81m/s^2 \quad (3.2.1.1)$$

$$F = 10.5N$$

Based on the result from this experiment and the evidence that supports it, the force value to be used from this point forward, can be taken as 10.5N.

3.2.1.1 Sensor Thickness Definition

Solving the Eq. (3.2.1) and Eq. (3.2.2) for the entire length of the beam, will result in the moment and shear diagrams that are shown in Figures 3.2.3 and Figure 3.2.3. The x increments are chosen to be every 1 mm.

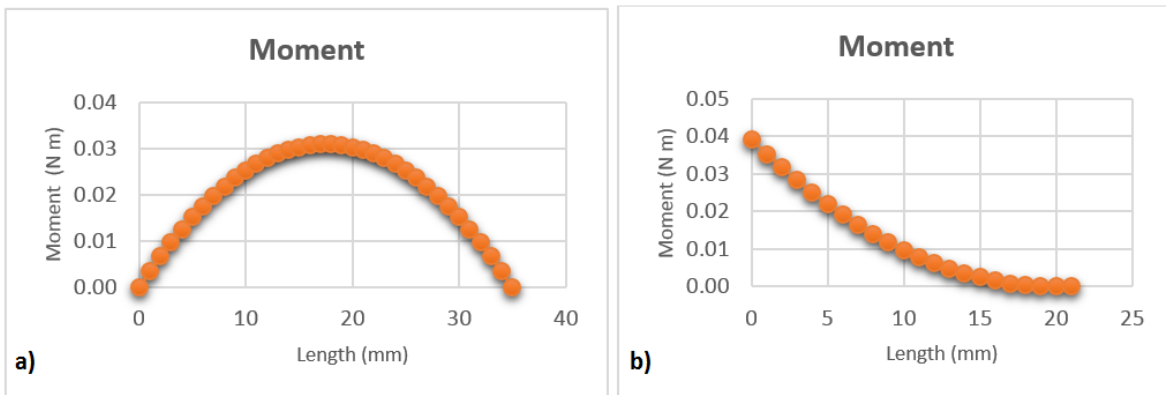


Figure 3.2.4. Moments diagram, a) for the simply supported beam at two ends and b) for the cantilever analogy.

Figure 3.2.4a) shows the bending moment acting on the beam follows a symmetric concave shape, as expected for the analogy made for the simply supported beam. True moment diagram for the real sensor will be shifted to the left according to distribution shown in Figure 3.2.1. Although not entirely realistic, this moment diagram helps by giving a value of the highest moment in the sensor. Thus, the maximum stress can be calculated by the following expression,

$$\sigma_m = \frac{M_{max}c}{I} \quad (3.2.3)$$

where σ_m is the maximum normal stress, M_{max} is the highest moment value, c is the largest distance from the top (or bottom because of the symmetry) of the sensor to the neutral axis, and I is the inertial moment of the transversal section. Since the model is being taken from a

top view of the instrument and bone assembly, the transversal section is to be a lateral view of the sensor, which is important to address in order to determine the inertial moment of area, expressed by,

$$I = \frac{bh^3}{12} \quad (3.2.4)$$

where b is the length of the transversal section, which in this case is equivalent to the length of the sensor as illustrated in Figure 3.1.2. In addition, h is the height of the beam (sensor thickness). It can be inferred, by looking Eq. (3.2.4) that the governing dimension will be the height or thickness of the sensor, for example: for $h \ll b$, the result of the inertial moment of area –and therefore, the mechanical stress itself– is mostly influenced by the impact of the h magnitude, particularly for small values that get closer to the microscale or even further. Consequently, the high aspect ratio between the thickness with the length and width is the key aspect of the sensor design, as expected from regular MEMS device development with one the characteristic dimensions being close to the microscale (thickness).

By taking the maximum moment from Figure 3.2.3, the corresponding maximum stress can be obtained by using the recently experimental value of the force applied to the instrument. Table IX has a number of constants needed to perform this calculation as well as the resulting maximum stress experienced by the sensor (highlighted in green) when analyzed as a simply supported composite beam.

TABLE IX. RESULTS TABLE FOR SENSOR DESIGN, SIMPLE BEAM ANALYSIS.

| Constants | Value | Unit |
|---------------------------------------|-----------------|----------------|
| Area | 0.002 | m ² |
| Length, L | 0.035 | m |
| Force, F | 10.3 | N |
| Distributed Force, w_0 | 212.9 | N/m |
| Young Modulus, E | 1.80E+09 | Pa |
| Cross section, b | 0.050 | m |
| Sensor thickness, t | 0.000230 | m |
| Inertial Moment, I | 5.07E-14 | m ⁴ |
| Reaction in A, Ra | 3.726 | N |
| Reaction in B, Rb | 3.726 | N |
| Maximum Stress | 73.9 | MPa |
| PVDF yield stress | 30.0 | MPa |
| PVDF Ultimate Tensile Strength | 180.0 | MPa |

A key aspect from Table IX is the data shown for the yield and ultimate tensile strength. In fact, the yield stress given by the manufacturer is highlighted in red to bring the attention on the fact the sensor will get stressed beyond the elastic limit and it will consequently experience plastic deformation. The same information is presented to the reader in Table X, for the second analogy of a cantilever composite beam.

TABLE X. RESULTS TABLE FOR SENSOR DESIGN, CANTILEVER ANALYSIS.

| Constants | Value | Unit |
|---------------------------------------|--------------|----------------|
| Area | 0.002 | m ² |
| Length, L | 0.020 | m |
| Force, F | 10.3 | N |
| Distributed Force, w ₀ | 195.7 | N/m |
| Young Modulus, E | 1.80E+09 | Pa |
| Cross section, b | 0.035 | m |
| Sensor thickness, t | 0.000230 | m |
| Inertial Moment, I | 4.06E-14 | m ⁴ |
| Moment in A, M _a | 0.04 | N m |
| Reaction in A, R _a | 3.91 | N |
| Maximum Stress | 111.0 | MPa |
| PVDF yield stress | 30.0 | MPa |
| PVDF Ultimate Tensile Strength | 180.0 | MPa |

Similar conditions are expected for this load configuration. With these two analogies, the thickness of the piezoelectric material for this experiment was finally selected as 230 μm , and according to Table 7, the piezo film thickness is therefore selected as 110 μm , which can be provided by the manufacturer [87]. By analyzing both scenarios, the calculations show the mechanical response of the sensor is safe and conservative in terms of the ultimate tensile strength.

3.3 Finite Element Analysis of the Contact Problem

As stated in Chapter 2, real engineering contact problems can be highly non-linear; mainly if the surfaces undergoing in contact cannot be considered part of elastic bodies and cannot comply with the Hertz theory assumptions. The particular analysis of the contact interaction between the bone and the patient specific instrument is not the exception, and some of the

assumptions made by Hertz Theory are not met, for example the friction consideration and the high congruency between the bone and the instrument.

This particular section is therefore dedicated to the finite element analysis of the contact nature between the bone and the patient specific instrument. The computational analysis was conducted using ABAQUS/CAE 6.13-1 (Simulia, Dassault Systèmes) software. Table XI contains the summary of materials used in the analysis as well as the corresponding properties, including the properties of the piezoelectric film which will be analyzed in the Section 3.4.

TABLE XI. SUMMARY FOR MATERIAL PROPERTIES USED IN FEA MODELS

| Property | Bone | Instrument | Piezo film |
|---------------------|-------------------------|-------------------------|--|
| Material | Human Bone | Nylon 6-6 Dura Form® PA | GoodFellow FV301301 0.110 mm thick PVDF |
| Poisson Ratio | 0.366 | 0.4 | 0.34 |
| Young Modulus | 1.3×10^{10} Pa | 1.6×10^9 Pa | 1.8×10^8 |
| d_{33} | - | - | -20 pC/N |
| d_{32} | - | - | 2 pC/N |
| d_{31} | - | - | 18 pC/N |
| Dielectric constant | - | - | 12 @ 1MHz |

Although computational analysis is not the main focus of this work, is important to present some of the key aspects of the software and the model. At the beginning, contact between the bone and the instrument was evaluated through the “*general contact*” definition of the software, which is the more general type of contact given by the software [85]. Moreover, surface selection is vital for the model to run appropriately, and “*slave*” and “*master*” surface selection must be done carefully to have reliable results. In Abaqus, the *slave* surface contains the nodes that cannot penetrate the master surface, and the selection should be made to the surfaces less rigid and the stiffness is recommended to be smaller as well, allowing the deformation to occur. In terms of meshing, the slave surface should always be meshed finer than the master counterpart, as well as master surfaces should be smooth [85].

In general, the methodology followed in this contact analysis also applies for the piezoelectric case to be developed in the next section. A summary of the steps followed to build the model taking into consideration all of the above aspects, is depicted in Figure 3.3.1 and can be listed as follows:

1. Elastic domains are added to all bodies, the sensor also included the piezoelectric domain.
2. The step definition: Quasi-static analysis was chosen through the software option of Dynamics, implicit. The increment “n” was set at $n = 0.05$.
3. Interactions between domains: Surface-to-Surface contact was defined by the penalty factor method with the tangential option selected. Different friction coefficients (μ) were tested, results for $\mu = 0.10$ and $\mu = 0.25$ are shown in the results. The proper master-slave surface selection is crucial. Master is the body undergoing higher mechanical deformation.
4. The load is defined as a displacement in the z direction. For the guide-bone analysis, is set at 1.3 mm. The initial gap between bodies is 0.6 mm, as a result, the displacement gets additional 0.7 mm acting as pushing force onto the bone surface, translated in constant force. This approach was chosen because of convergence issues when modeling with applied force as boundary condition. The final value of 1.3 mm of displacement is selected after an iterative process. When the piezoelectric is added, the displacement is set to move the guide 11.25 mm towards the bone, pushing the piezoelectric film in the middle. An output voltage boundary condition is also added to read the piezoelectric response.
5. Mesh: Tetrahedral elements are selected for standard and well known convergence results. The body with the slave surface must be meshed finer than the master. For the guide-bone contact analysis, the bone is selected as master, thus the global element size is selected at 1.75. The instrument is then selected as slave and the global size element is 1.25. Same rationale when including the piezo sensor: the film to be the slave and thus global element of 0.50; while guide and bone to be selected as masters and element sizes of 2.00 and 1.50, respectively.

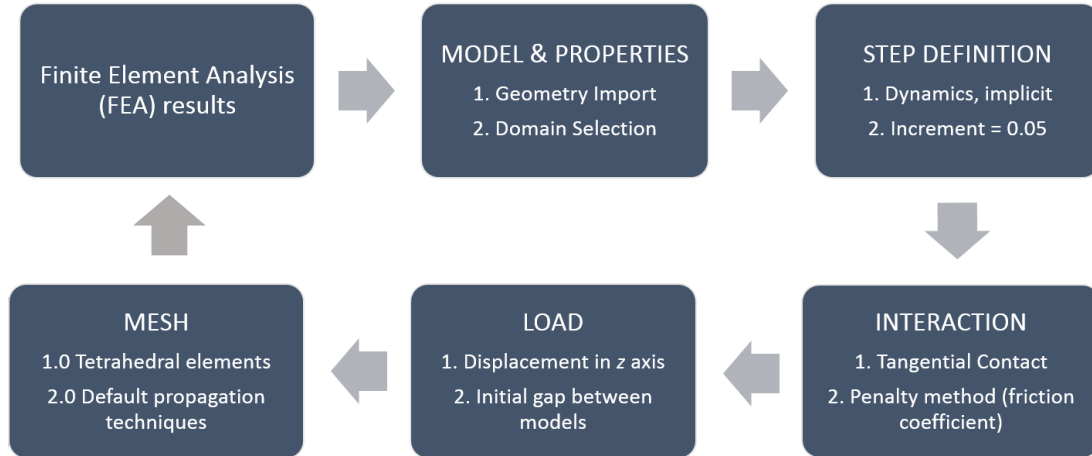


Figure 3.3.1. Finite Element Analysis process followed for model convergence.

An important aspect that was noticed prior meshing the bodies is that the instrument complex geometry and features are difficult to mesh since they would consume a considerable amount of computational resources. Therefore, the instrument geometry was simplified to concentrate the analysis only at the contact interface. Figure 3.4.2 shows the meshing result under this simplification of the instrument geometry.

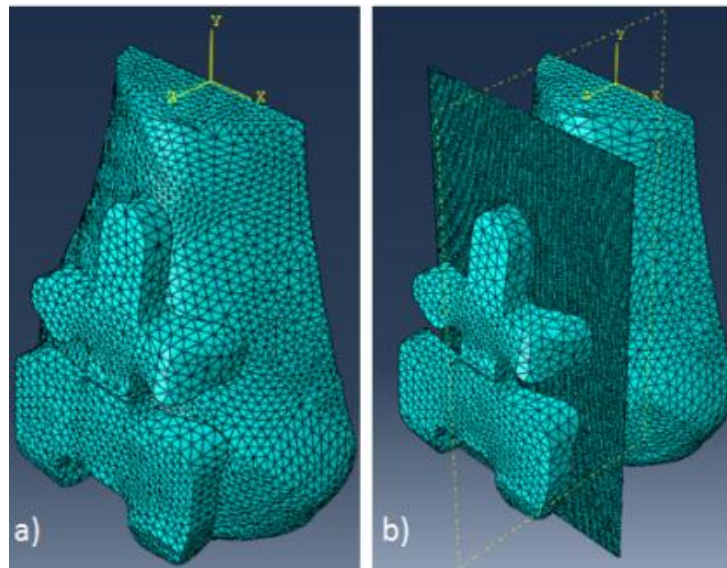


Figure 3.3.2. Mesh result according to the slave and master surface selection with the simplified instrument, a) only bone and instrument contact analysis and b) piezoelectric film included in the model.

After the meshing, interactions and all of the software required inputs are defined and the model is submitted for computational analysis. Figure 3.3.3a) represents the result of the

interaction between the bone and the guide right at the contact interface when the friction factor, $\mu = 0.25$ has been selected. Figure 3.3.3b) shows the contact result when $\mu = 0.10$. For these images, the instrument has been hidden from the model. An interesting observation from both results is that the middle right and lower left sections have a small contribution to the contact interface, which indicates the instrument did not fully fit on the bone surface at the region where a nearly fully conformal contact was expected according to its design. Because of this finding, virtual springs with very low constants ($k = 0.001$ N/m) were added in the yx -plane, allowing the instrument to translate and slide a bit onto the bone surface without compromising convergence.

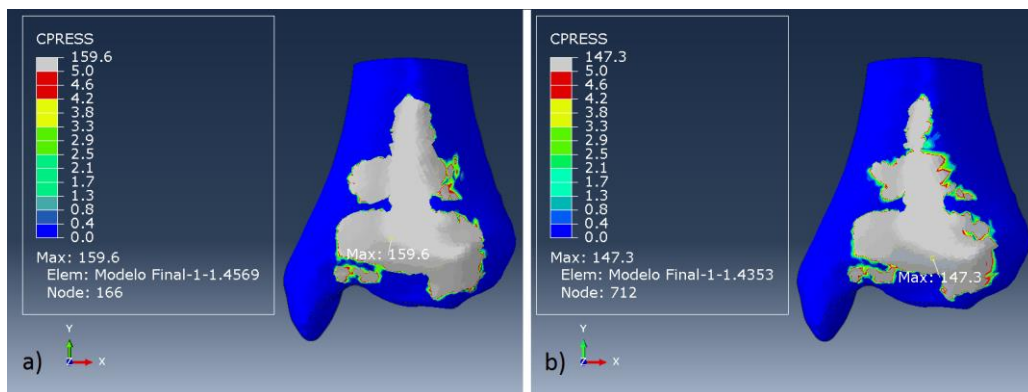


Figure 3.3.3. Contact analysis results from FEA; a) High friction simulation resulting in 159.6 MPa as maximum pressure and b) Low friction simulation resulting in contact stress of 147.3 MPa.

After the springs were added, the model processing time was decreased and the convergence was smoother, however, the behavior was the same as Figure 3.3.3. These findings should be validated through the sensor experimental data and brought to discussion when evaluating sensor output.

At this point, the analytical approximation can be evaluated at the node coordinate for the maximum contact pressure shown in Figure 3.3.3a). At this location, the radii of curvature are measured from the CAD software, the values obtained are: $R_1 = 87.5$ mm and $R_2 = 94.5$ mm. Radii definition is shown in Figure 2.4.3. Also, the theoretical normal force F applied to the instrument is needed. It was found at 9.80 N, according to statistical experiments carried out previously.

Evaluating these values in Eq. (2.4.6), (2.4.7) and Eq. (2.4.8) gives a maximum contact pressure of **140.8 MPa**. This value differs by approximately **11.8%** from the **159.6 MPa**

found in the FEA results, shown in Figure 3.3.3a). Repeating the exercise with the low friction results from Figure 3.3.3b) gives **4.4%** of difference from the **147.3 MPa** found in the FEA results. Although small, these differences can be potentially explained by the assumptions of the analytical approach compared to the FEA model. For example, the computational analysis considered the effect of friction through the Penalty contact method, while the Hertz theory neglects the friction contribution. In fact, the reason of showing two results with different friction coefficients, is to demonstrate that the results from finite element analysis get closer to the results from Hertz theory as the friction goes down, verifying the accuracy of the finite element model, at a theoretical level.

Figure 3.3.4a) and Figure 3.3.4b) show the contact shear pressure in x - and y -directions, respectively (ABAQUS notation). In case of the x -shear pressure component, is interesting to see that the lower left and middle right sections are not contributing to the contact when the instrument tries to slide to the left or to the right, just as recently discussed for Figure 3.3.3. The change in the sign obeys the curvature of the bone itself, and the direction of the shift. Same situation is observed with shear pressure contact in y -direction.

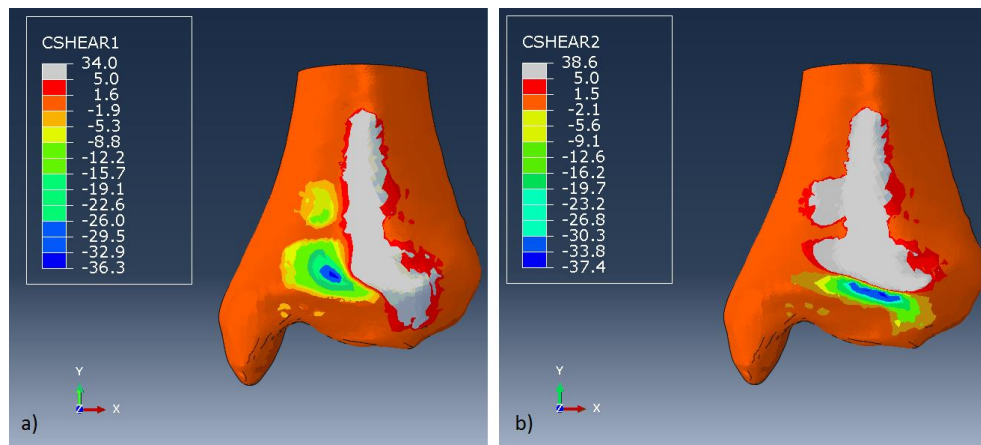


Figure 3.3.4. Shear contact pressure results from FEA, a) Shear in x - direction, b) Shear in y -direction. Units in MPa.

The value added by the shear stress results from the contact modeling, which is good agreement with outcome observed in normal contact pressure. Despite the final output of the sensor being developed in this work, the result from the contact analysis is introducing a new insight that might be interesting to develop in further detail, in terms of the instrument design and geometry.

3.4 Finite Element Analysis of the Thin Piezo Electric Film

Given the final thickness for the entire sensor, the finite element analysis is conducted under the assumption that the sensor is a homogenous material whose final thickness is the sum of all of the layers and the entire thickness can be considered as just one material with the weaker mechanical properties [84]. This assumption was addressed in Section 3.2 when mechanical analysis was conducted. Generally for this case, the weaker element is the piezoelectric material, thus the analysis is conducted as if the sensor was only a piezoelectric film with the entire array thickness.

By following the same methodology listed in the Section 3.3, a new geometric model is submitted for analysis including the sensor as a film between the instrument and the bone. Figure 3.4.1 shows the electrical response obtained by the PVDF when pressed between the instrument and the bone. The output voltage ranges from -87 mV to +50 mV. The positive and negatives values for the output potential are because of the d_{33} negative coefficient value from Table II, where a concave curvature in the z -direction produces negatives voltages and a convex curvature produces positive values.

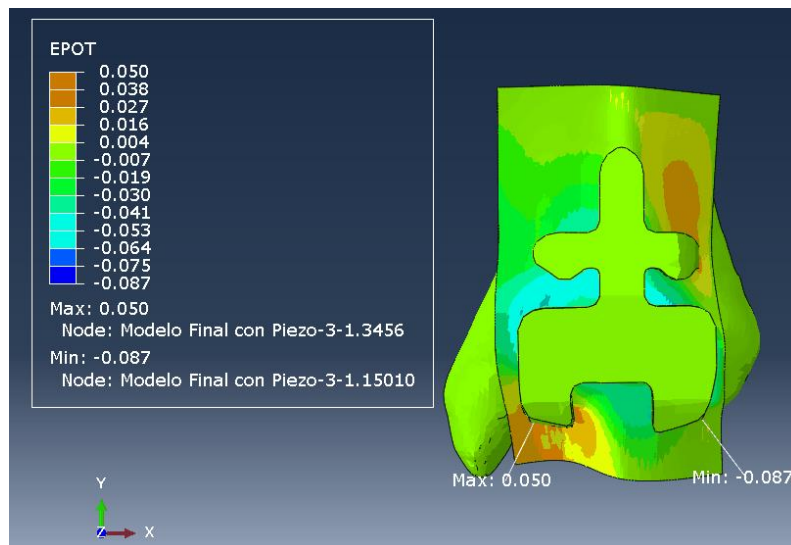


Figure 3.4.1. Electrical potential distribution from FEA; electrical in response to the mechanical deformation, units in V.

In addition, Figure 3.4.1 shows the location of the maximum and minimum voltage outputs at the bottom sections of the instrument, which complies with the Von Mises stress shown in Figure 3.3.3, where the highest stress values are found at the same locations. This is also in

good agreement with Eq. (2.5.1), when higher piezoelectric responses are produced as result of higher mechanical stress. The Von Mises stress distribution from Figure 2.4.6 also indicates that the maximum stress value is not higher than 125 MPa (red scale), which is still a safe value with respect to the tensile strength of the material [81].

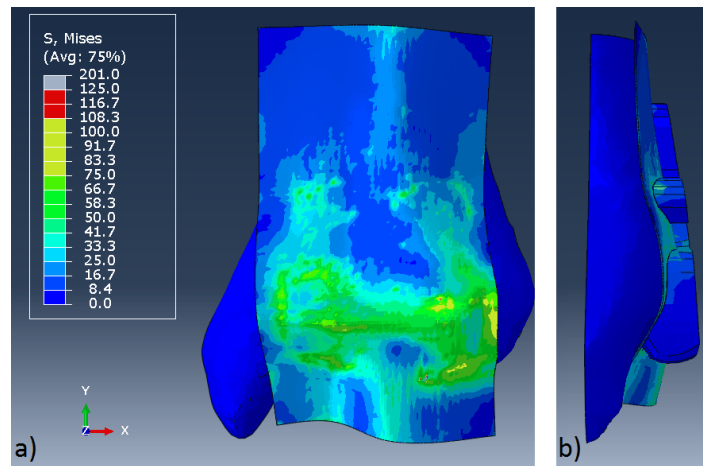


Figure 3.4.2. Von-Mises stress distribution, a) Front view without patient instrument and, b) Lateral view showing instrument. Units in MPa.

Further information can be extracted from analyzing particular mesh elements. The data for the mesh element with the highest positive piezoelectric response (+50 mV), located at the lower left section of the instrument, is extracted from the software and shown graphically in Figure 3.4.3.

As expected, the electric response of the piezoelectric film and the mechanical stress are closely related, also predicted by Eq. (2.5.1) and shown in green and yellow series from Figure 3.4.3. However, the importance of this graph is to evaluate the voltage range at which the sensor is only sensing mechanical deformation but not contact pressure.

By looking the stress behavior as depicted by the yellow series in Figure 3.4.3, the mechanical deformation starts approximately at 0.8 mm, where the sensor begins to adopt the shape of the bone; afterwards and up to approximately 6.4 mm the instrument approaches to the bone pushing the sensor in between, but no contact is made yet.

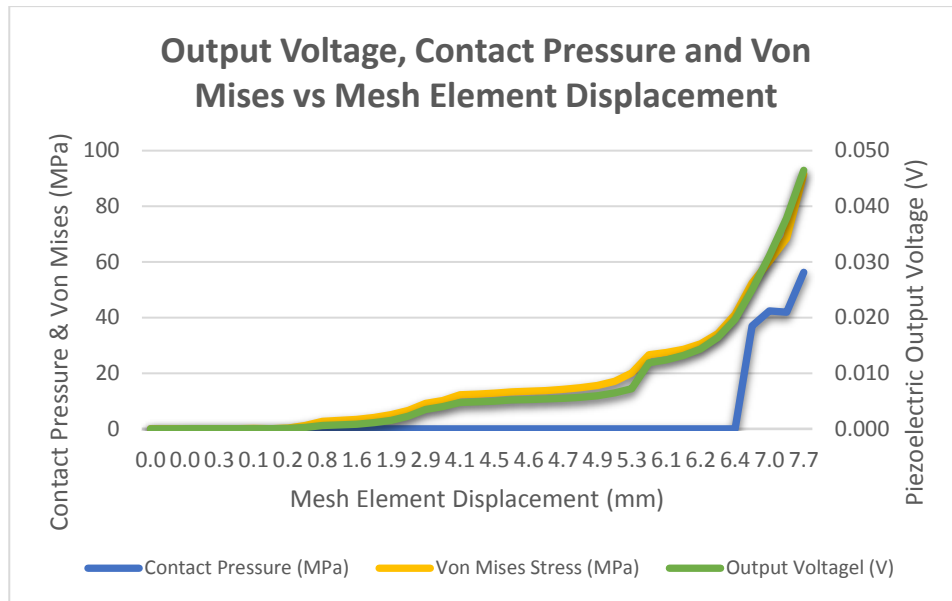


Figure 3.4.3. Relation between mechanical properties and the electric output from mesh element with highest positive voltage reading.

As shown by the green series, the voltage output at 6.4 mm is close to 20 mV, indicating that readings below this value do not correspond to actual contact. Right after this point the contact pressure starts increasing rapidly and voltages above 25 mV now indicate the piezoelectric is being pressed by the instrument until the displacement has reached the maximum value, approximately at 7.7 mm. One particular section of interest is the nearly constant value of contact pressure between 7 mm and 7.7 mm, which could be possibly explained as a stabilization period occurring when the instrument slides on the bone surface until it fits, similarly to the situation observed when explaining the contact results in Figure 3.3.3 and the use of virtual springs in the computational analysis. This information is highly important for the development of the acquisition system for the sensor and for the interpretation of data, particularly because it allows establishing a threshold limit for making a difference from surfaces in true conforming contact and surfaces only bending the sensor.

CHAPTER 4

Results and Analysis

- 4.1 Sensor Assembly
- 4.2 Data Acquisition System and Testing Fixture.
- 4.3 Test Results and Analysis

4.1 Sensor Assembly

The sensor array, shown in Chapter 3 through different images, was designed using EAGLE 7.2.0 Graphical Layout Editor for Windows (CADSoft Computer). Thus, the copper traces forming the electrodes were laid out using the software. Some additional length was added to provide the corresponding soldering spots for each line. Figure 4.1.1 illustrates both, the vertical and horizontal electrodes patterns.

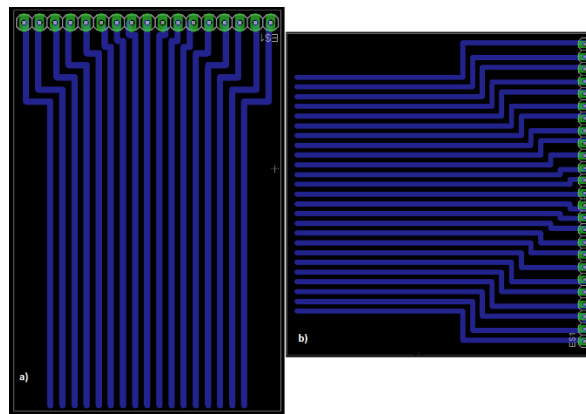


Figure 4.1.1. Layout of the vertical and horizontal electrodes, a) vertical and b) horizontal.

As observed in Figure 4.1.1, the thickness of each line or trace is 1 mm with the distance between them as well of 1 mm. However, the commercial soldering pins have pitch of 0.1 in between each pin, and thus some small deviations at the end of each trace had to be introduced. Once the layout is complete, the files are exported to be printed in the polyamide substrate as previously discussed. Upon this flexible circuit printing, the top and bottom electrodes are ready for assembly. The company *LeitOn* (Berlin, Germany) was contacted for developing the prototypes. Figure 4.1.2 shows the result of the flexible printed circuits based on the layout shown in Figure 4.1.1.



Figure 4.1.2. Actual printed vertical and horizontal electrodes on the polyamide substrate (with adhesive layer on).

The 3M adhesive (467MP) is incorporated in the flexible printed circuit shown in Figure 4.1.2 in between the traces of the printed copper patterns. As expected, is needed to peel the adhesive cover layer to reveal the printed pattern. Afterwards, the electrode is ready to be assembled with the piezoelectric film. It has been mentioned that the piezoelectric is a PVDF film from the company *GoodFellow* (Cambridge, England) under the model of FV301301. Its specifications are: uni-axial PVDF film of 0.110 mm thickness and 50x50mm² of total area. Figure 4.1.3 shows the assembled sensor, with an additional view of the piezoelectric film.

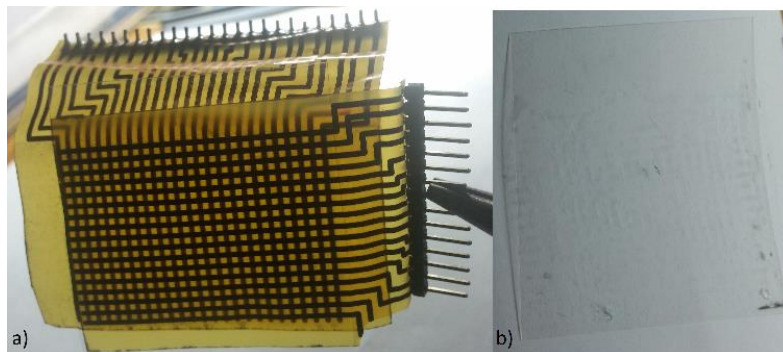


Figure 4.1.3. Assembled sensor as the structured discussed in chapter 3, a) frontal oblique view of the array of sensing nodes and b) piezoelectric film purchased from *GoodFellow*, company model FV301301.

Upon assembly of the sensor, the corresponding pins are soldered to enable communication of each trace with an external acquisition data system. Figure 4.1.3 also shows the pins soldered to the electrodes which will be needed to connect to an external data acquisition board, as recently mentioned.

Because of the high number of entries needed to extract information from each line, the communication process from the sensor to a computer based system is challenging. Furthermore, the output signal range expected from the sensor shown in the results of the computational analysis, is also adding complexity to the acquisition data since the signals are very small. Additional details about the electronics required to extract the data, as well as the mechanical test bench developed to run the test cases, are discussed in the Section 4.2.

4.2 Data Acquisition System and Test Fixture.

Two sub-systems are required to start reading the output from the sensor assembly and verify the results with those given by the finite element analysis. First, the electronic data acquisition system (DAQ) must be defined for the voltage range that is expected as output from the sensor. The acquisition system must then be responsible for amplifying the signal, performing a signal selection due to the large amount of signal coming from the sensor (multiplexing), verifying the signal sign in order to evaluate negative values and lastly, send the data to an analog-to-digital converter (ADC) which for this application is selected through an Arduino board (mega 2560). After the Arduino processes the signal and converts it to a digital number, the values are stored in matrix form using the coordinates from the sensor nodes and a 3D surface plot is expected as final output. Figure 4.2.1 shows a high level description of the sequence of steps the signal must go through in order to get visualized by the computer based system.

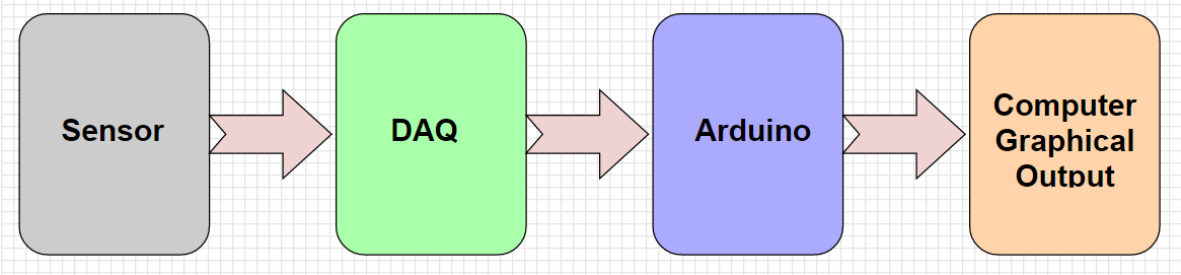


Figure 4.2.1. High level view of the steps followed by the sensor output.

Despite data acquisition systems and boards are highly known and there are multiple options from commercial solutions, the monetary cost of getting a standard and out of the shelf acquisition board is beyond the budget available for the thesis. This is mainly due to the

specifications needed to process the data from the sensor. Consequently, a custom made system must be designed and built in order to read the signals from the sensor.

The circuit proposed to perform the acquisition of the signal, is shown below in Figure 4.2.2. Considering the output from the computational analysis seen in the previous chapter, the voltage range is expected – to this point – to be somewhere in between -50 mV and +80 mV, depending on the bending direction from the piezo film. Based on this input, the components for the data acquisition system are selected and the circuit is designed and proposed.

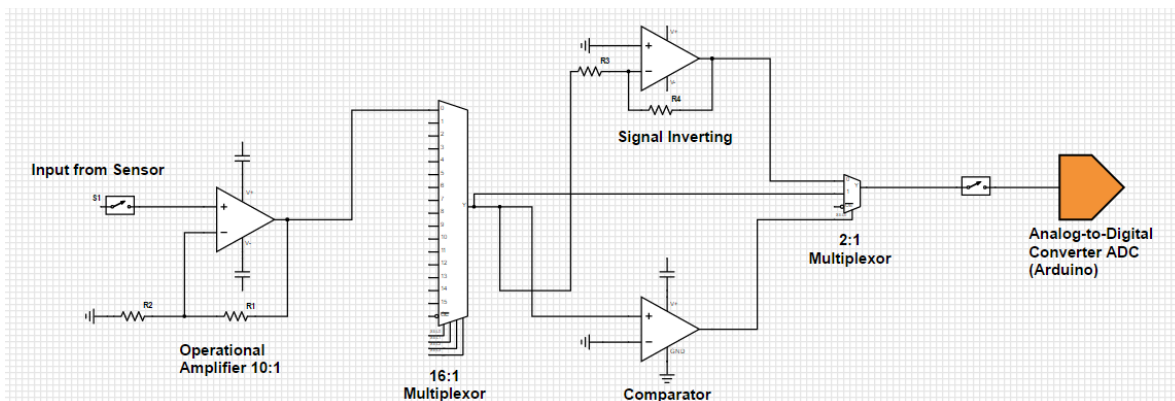


Figure 4.2.2. Designed circuit for the data acquisition system.

The components for the circuit shown above are selected to operate at -5V as V_{EE} and +5V as V_{CC} . The logic of the circuit is to first take the signal and amplify its value with an operational amplifier (op amp) connected as a non-inverting type with a gain factor of 1:11, meaning that the output from the op amp will be 11 times larger than the input. In order for this to happen, the values in R1 and R2 are chosen to be 10k Ω and 1k Ω , respectively. Moving forward, the amplified signal now enters in a 16-channel multiplexer responsible for selecting the corresponding value given the corresponding coordinate from the sensor. The multiplexer is logically controlled by the Arduino, which contains a custom made program to control these multiplexers as function of the coordinate in the sensor matrix. Appendix B contains the code for how the Arduino is programmed to control the multiplexers in terms of the array coordinates, the reader is encouraged to take a look to the matter if further information is required.

After the multiplexing stage, the signal feed three components: an op amp connected as a inverting amplifier with gain factor equals to 1 ($R3 = R4 = 10k\Omega$); an op amp connected as

a comparator to a voltage reference, in this case ground (GND) to produce saturated output voltages ($+V_{CC}$) when the signal is larger than zero and to produce a zero voltage output when the signal is smaller than zero (i.e. negative value). This $V_{CC}/0V$ output from the comparator controls the selection pin in the next component in the circuitry: the 2-channel multiplexer, which as has been recently stated, is controlled by the comparator and selects the signal from the 16-channel multiplexer whenever positive or from the inverting amplifier whenever a negative value is found. In addition, this 2-channel multiplexer is the third components receiving the signal from the 16-channel multiplexer. Finally, the signal enters to the Arduino for the analog to digital conversion process. Figure 4.2.3 illustrates a block diagram for the entire acquisition board that has been designed.

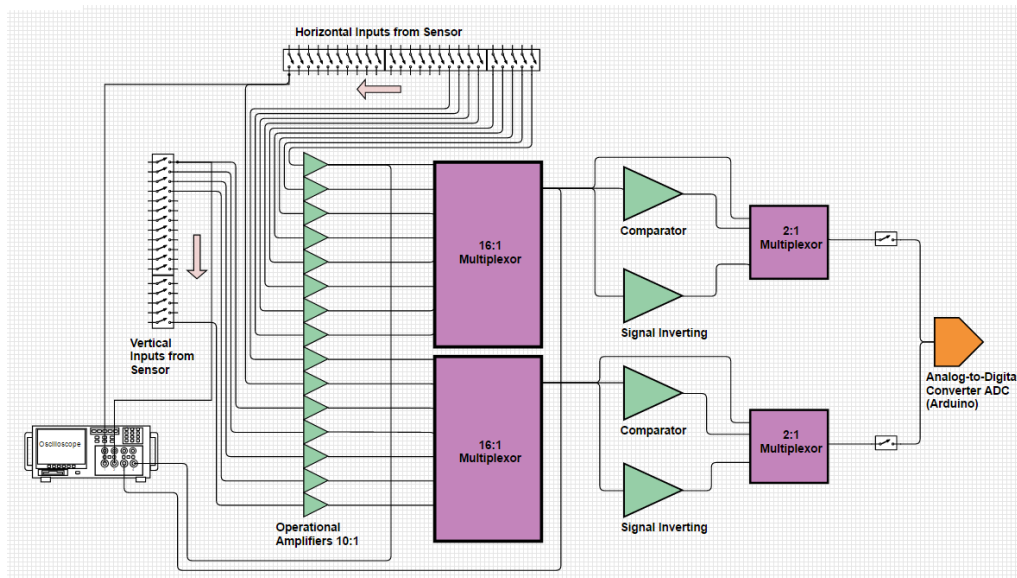


Figure 4.2.3. Block diagram for the DAQ board design.

An important consideration at this point, is that Figure 4.2.3 is not a complete schematic for the board. The complete schematic along with the bill of materials (BOM) is also found on Appendix C. Also, this block diagram includes an oscilloscope connected to three important sections: first, directly connected to the raw signal from the sensor, a second probe connected to the output of the op amp amplifiers and finally, after the 16 channels multiplexors. This information will be relevant in next section when describing the results obtained. More importantly, when creating the final layout for the DAQ system, it must be considered that the sensor needs a reference voltage to produce the electric potential when the mechanical

input is applied, i.e. ground connection. As a result, a decision was made to connect some of the inputs of the sensor to ground on the board, with the intended use of generating a reference voltage. When making this decision, the pins connected to ground were selected every two signals, intercalating a signal then a ground connection, then a signal and so on. As a downside, this configuration will reduce the resolution of the sensor to the half, because half of the lines are to be grounded in both the top and the bottom electrode. Figure 4.2.4 shows the updated block diagram with the recently grounded connections added.

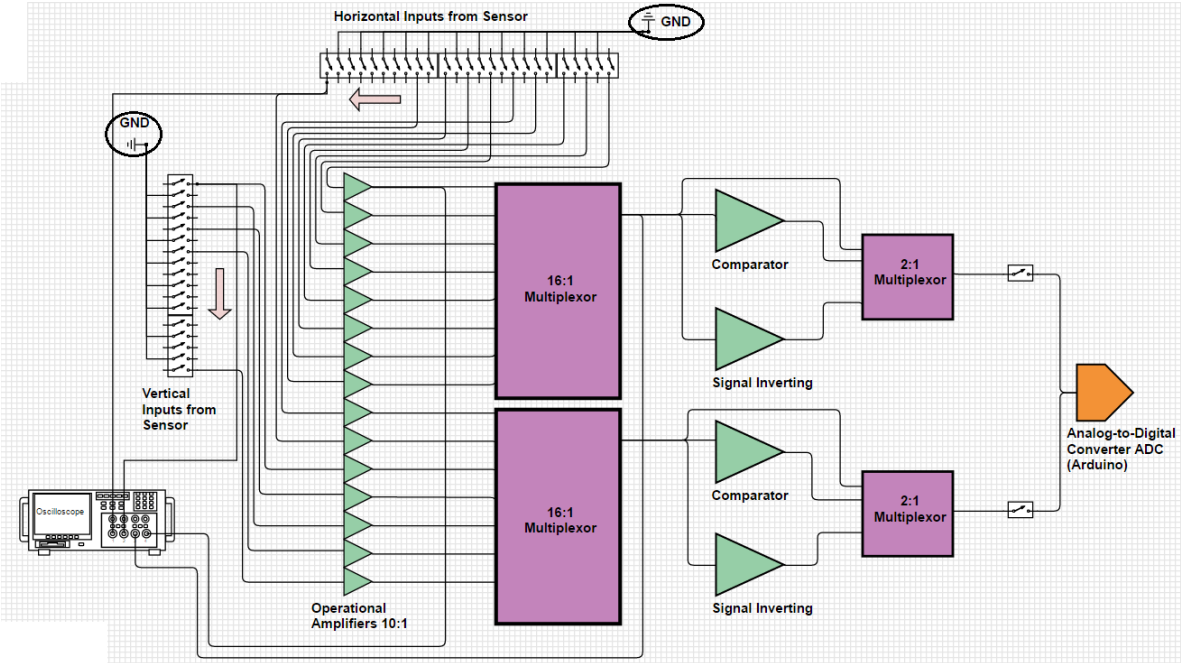


Figure 4.2.4. Modified Block diagram for the DAQ board design with ground connections.

To better explain the resolution reduction and how this modification to the board schematic is affecting the sensor, an equivalent image is created to depict the equivalent connection.

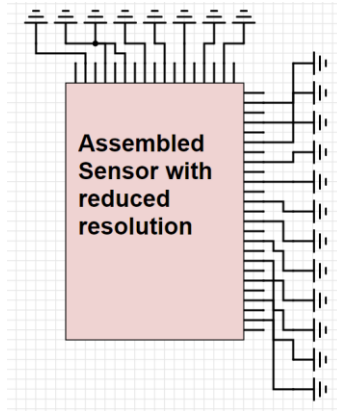


Figure 4.2.5. Modified Sensor pins output with ground connections.

In Section 4.3, test case No.1, the results will be discussed when connecting the sensor under this “*coarse configuration*”. In fact, the DAQ board was manufactured to acquire data under this configuration. Moving forward with the stages of DAQ system development, the final layout is shown in Figure 4.2.6 for a two level printed circuit board (PCB) with power routing of approximately 6.1 mm thick (0.024 in) and 4.0 mm for the signal routing (0.016in).

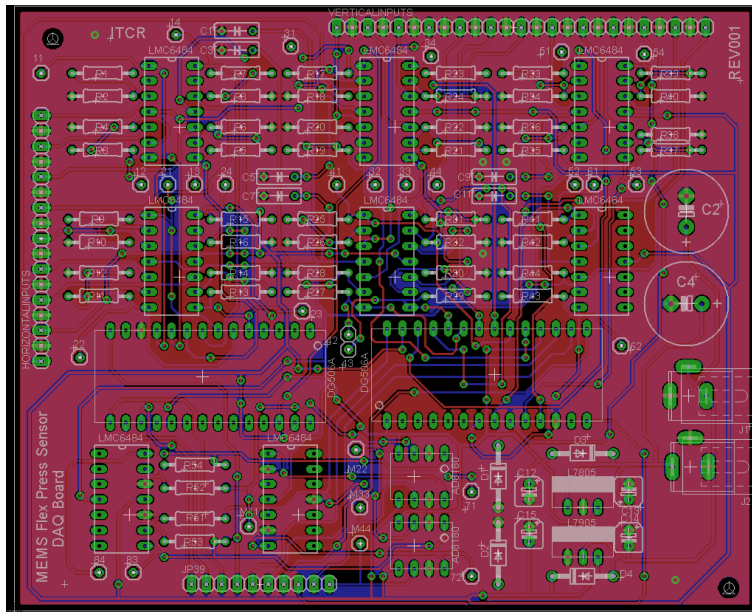


Figure 4.2.6. DAQ board layout for two copper layers.

In addition to the block diagram components shown in Figure 4.2.4, the final layout of the board included a voltage regulator circuit to always deliver +/-5V through the entire board,

which can be appreciate it at the lower right corner of the layout. More information can also be found on Appendix C. The selected manufacturer house to print this circuit board was Advanced Circuits (Colorado, United States). Figures 4.2.7 and 4.2.8 show the PCB without components and the fully soldered board as well.

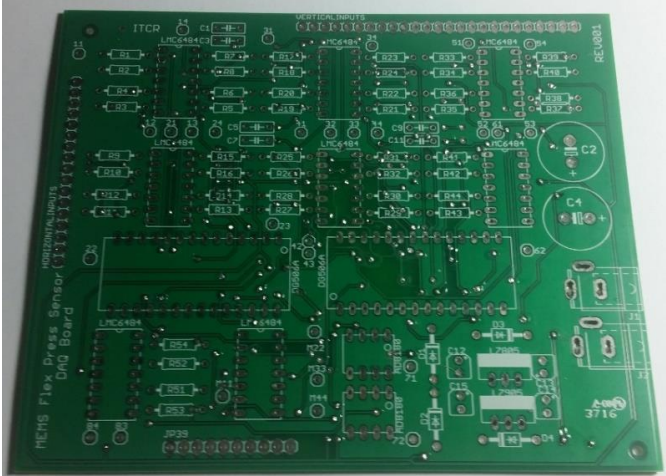


Figure 4.2.7. Non-soldered PCB.

At the beginning, all the vias were soldered to communicate the top and bottom copper. Afterwards, the components were put in place and soldered to the board as seen in the image below.



Figure 4.2.8. All components soldered PCB.

Once the PCB is in place, the system is almost ready to start taking the outputs from the sensor. So far, the only pending task prior initiating the readings is the mechanical test bench

or fixture to provide a well-known pressure value to the sensor and compare after the measure has been made.

To address this particular requirement, a pneumatic based fixture was developed to hold and align the instrument, sensor and bone in one place and in one direction. The aim of this fixture or test bench is to provide a more stable measurement on the system and to provide the sensor with known pressure values. Figure 4.2.9 shows the physical assembly with all of the components in place, including the custom made PCB and the Arduino, all wired together.

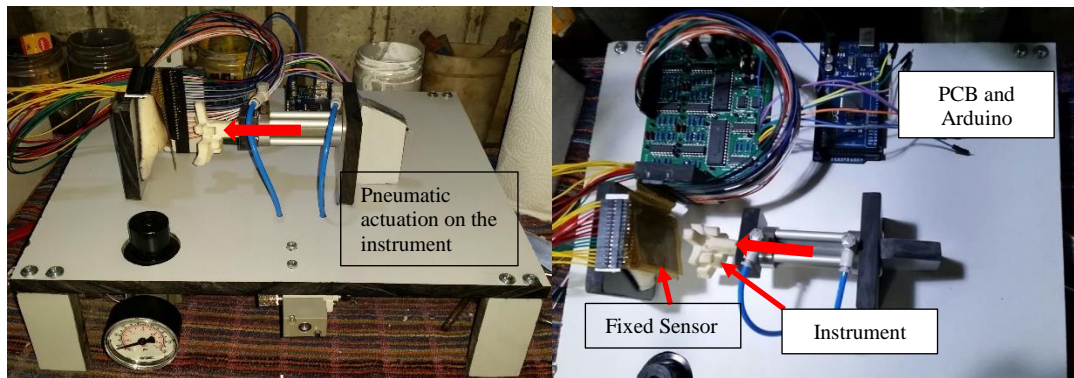


Figure 4.2.9. Test pneumatic fixture.

An important fact is that the pressure regulator is calibrated at +/-3% on the analog scale of the gauge and the pressure increments can be read every 2.0 psi. Finally, it is important to mention the diameter of the pneumatic actuator, since it will be responsible for delivering the pressure to the instrument and from this to the sensor. The actuator is purchased from McMaster Carr (Illinois, United States) under the code 1691T86, impact-resistant air cylinder, round face, 0.25 in outer diameter, and 2.0 in of stroke. With this information, and the experimental force determined in section 3.2.1 experienced by the instrument when pressed onto the bone, it is possible to estimate the amount of compressed air pressure that is needed to obtain approximately 10.5 N of force on the instrument. From basics mechanics, it is well known that,

$$P = \frac{F}{A} \quad (4.2.1)$$

Where P is the pressure coming from the compressed air supply, F is the force applied to the rod and, A the area of the rod. Table XII contains the results of the fixture set up.

TABLE XII. FIXTURE PNEUMATIC PRESSURE EQUIVALENCE TO THE INSTRUMENT

| Magnitude | Value | Units |
|--|-------------|----------------|
| Pressure (regulated from the pressure indicator) | 48 | Psi |
| Pressure | 330.9 | kPa |
| Actuator diameter | 0.25 | in |
| Actuator diameter | 6.35 | mm |
| Actuator area | 3.16692E-05 | m ² |
| Force | 10.5 | N |

As seen in Table XII, it takes about 48 psi, which is equivalent to 330.9 kPa, to produce a force of 10.5 N on the instrument, which is a close approximation to the mean force value extracted from the experiment conducted in Section 3.2.1.

4.3 Test Results and Analysis

Following all the set up and the wiring from the test fixture, the PCB and the Arduino, the testing process takes place. The only aspect that has not been addressed in detail to this point is the Arduino program or source code for the application, which contains the controlling bits for the multiplexing in the PCB and additionally performs the reading from the analog input and displays the digital response. In Appendix B, the source code with the corresponding comments can be found. The following experiments were conducted:

1. First run with entire system connected: At first, the whole system is wired up, the program is uploaded to the Arduino and the pressure is regulated at 20 psi (137.9 kPa), pushing the instrument with a resulting force of 4.4 N. The response from the Arduino is printed in a matrix form that is shown in Table XIII below. As seen, the values read from each node of the sensor are always close to the maximum value of 1023 bits returned by the Arduino, and the matrix is filled with similar values entirely. In terms of the Arduino functionality, the *AnalogRead* function from the analog inputs takes signals from 0V to +5V and converts them to digital outputs from 0 to 1023 in a bits scale. The Arduino resolution when converting from analog to digital is 0.0049 V, which means that the output from the DAQ board is close to 5V, as $1023 \times 0.0049 = 5.0127V$. This result is telling that all of the operational amplifiers

are getting close or they are all at the saturated value, which is equivalent to the input voltage V_{CC} , in this case +5V.

TABLE XIII. ARDUINO DIGITAL OUTPUT MATRIX (COARSE READING)

| | x- coordinates (mm) | | | | | | | | |
|----|---------------------|-----|------|------|------|------|------|------|------|
| | 2 | 6 | 10 | 14 | 18 | 22 | 26 | 30 | 34 |
| 2 | 1023 | 993 | 1023 | 1023 | 1023 | 1000 | 1023 | 1023 | 1023 |
| 6 | 1023 | 993 | 1023 | 1023 | 1023 | 1000 | 1023 | 1023 | 1023 |
| 10 | 1023 | 993 | 1023 | 1023 | 1023 | 1000 | 1023 | 1023 | 1017 |
| 14 | 1023 | 993 | 1023 | 1023 | 1023 | 1000 | 1023 | 1023 | 1023 |
| 18 | 1023 | 976 | 1023 | 1023 | 1023 | 1000 | 1023 | 1023 | 1023 |
| 22 | 1023 | 993 | 1023 | 1023 | 1023 | 1000 | 1023 | 1023 | 1023 |
| 26 | 1023 | 993 | 1023 | 1023 | 1023 | 1000 | 1023 | 1023 | 1015 |
| 30 | 1023 | 993 | 1023 | 1023 | 1023 | 1000 | 1023 | 1023 | 1023 |
| 34 | 1023 | 993 | 1023 | 1023 | 1023 | 1000 | 1023 | 1023 | 1023 |
| 38 | 1023 | 993 | 1023 | 1023 | 1023 | 1000 | 1023 | 1023 | 1023 |
| 42 | 1023 | 993 | 1023 | 1023 | 1023 | 1000 | 1023 | 1023 | 1023 |
| 46 | 1023 | 993 | 1023 | 1023 | 1023 | 1000 | 1023 | 1023 | 1023 |
| 50 | 1023 | 993 | 1023 | 1023 | 1023 | 1000 | 1023 | 1023 | 1023 |

Additionally, the pressure setting was changed from 20 psi (137.9 kPa) up to 80 psi (551.6 kPa) in increments of 10 psi. The result was the same as shown in Table XIII, meaning that the amplifiers were still saturating at the V_{CC} value and the DAQ was not responding to the change in the pressure applied to the sensor. More importantly, it was noticed that the digital values of the matrix remained the same even without applying any kind of pressure to the sensor. Immediately, the output after each amplifier was measured using an oscilloscope (Fluke industrial scope meter 125) connected to the probes as shown before in diagram from Figure 4.2.4, showing indeed 5V relative to ground. The input signal from the sensor to the amplifier was also verified with the corresponding probes (see Figure 4.2.4 as well) and the result was oscillating between 0 and approximately 20 mV, which can be considered noise from the sensor. Another important aspect to be observed from the results in the matrix of Table XIII, is the resolution being decreased as result of the ground connections every two electrodes as it was discussed in previous section. By looking at the coordinates, it can be noticed that the node density is coarser than expected, as the sensor was design to have a

sensing point or node every 2 mm (1 mm of pitch), the matrix in table shows the coordinates every 4 mm. Although not yet in conclusions, is clear that the connections made on the PCB designed as the DAQ board do not extract properly the information from the sensor. Fortunately, individual connections are possible for each sensor electrode (individual lines) and more testing was carried out in order to gain insight of the sensor output and behavior. Finally, an additional technical aspect was analyzed as a potential caused for the Arduino to steadily maintain the same values in each cell of the matrix: the time needed for the Arduino to read an analog input versus the switching time that it takes the multiplexers to switch from one input to another. For the custom designed DAQ board, the 16 channel multiplexer was the *Maxim CMOS DG506A* and the 2:1 channel multiplexer was the *Analog Devices AD8180* (see appendix C); and from the manufacturer datasheets it can be found that the switching times are .06 μs and .01 μs , respectively, whereas it takes about 100 μs for the Arduino to read the analog input. This numbers show that there is enough time for the multiplexers to do the switching and send the data to the Arduino. In fact, the Arduino will take 100 μs to do the reading, then it will send another flag for a new switching on the multiplexers and then it will take another 100 μs to do the second reading and so on. As a result, there is technical evidence that supports the Arduino and the DAQ are properly matched in terms of software communication and data transfer.

2. Data acquisition board testing: Because of the previous results of the op amp getting at the saturation value, it is needed to evaluate whether the DAQ board is working as expected or not. One way to review this matter is connecting both channels from the oscilloscope to follow the same signal path: one channel connected to the raw signal from the sensor, and the second channel connected to the output of the amplifier from the same signal. The expectation is have a signal, on channel 2, 10 times bigger than the signal observed in channel 1. Since the sensor output has not been verified at this point yet, it is required to enter a well-known input from a signal generator so the board functionality can be evaluated. Using a *FeelTech* arbitrary Function signal generator, model FY32005, a square signal was generated with 50mV amplitude and 50Hz frequency. Under such parameters, the terminal of the signal generator was connected to the input of the amplifier and also to the channel 1 of the oscilloscope (in addition to the Fluke model previously used, a SainSmart oscilloscope model

DDS-120 was also used); then the second channel of the oscilloscope was then connected to the output of the amplifier. Again, a 1:10 gain is expected. When using the SainSmart oscilloscope, the readings are actually taken in the computer through the device software. Figure 4.3.1 captures a screenshot of both channels measurements.

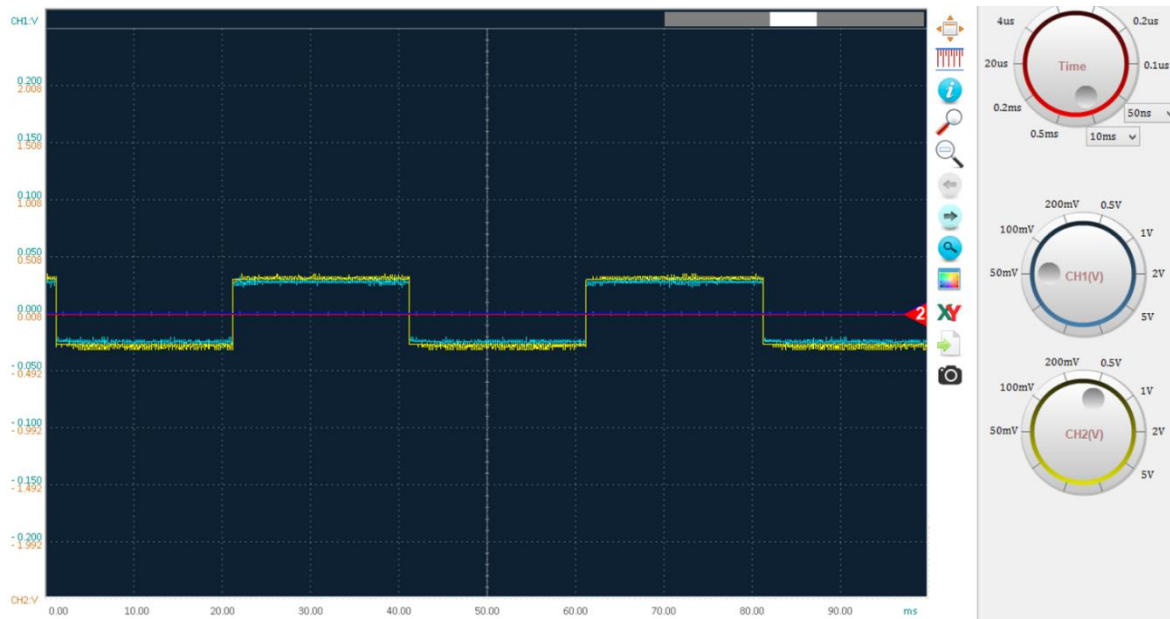


Figure 4.3.1. Screenshot from the oscilloscope SainSmart DDS-120 model.

Blue wave in the screenshot refers to the channel 1 measurement while the yellow one shows the data from channel 2. In the knobs observed in the middle-right section of the Figure 4.3.1, is observed that the scale from channel 1 (blue) is 10 times smaller than the scale in the yellow knob (channel 2). In fact, by looking at the waves' amplitude is clear to appreciate that both signals are equivalent. This is well supported by the scale factor seen in the middle-right knobs. In summary, the DAQ board responded accordingly to design parameters and these results demonstrate that the issue observed in test case #1, is not due to the DAQ board itself. As a side note, this test was reproduced for every amplifier in the board, just to eliminate the uncertainty of having one chip broken or malfunctioning.

3. Results from a unique node output, sensor characterization: Now that the DAQ board has been isolated and tested, and there is enough evidence to support that is working well, it is needed to understand the sensor response, in an isolated fashion as well. In order to run such

a test, a particular node needs to be selected to extract the data from. Measuring the same node taken in Section 3.4, the vertical electrode was connected to ground and the horizontal electrode was connected to the channel of the oscilloscope (only one channel needed for this test case). Figure 4.3.2 illustrates an equivalent circuit to better explain how the connection was set. The following step after setting up the connections was to set up the pressure value, which was fixed to 20 psi (137.9 kPa) for the first value recorded.

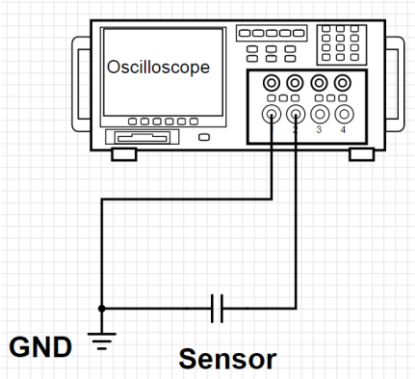


Figure 4.3.2. Schematic for one node sensor output reading.

The sensor is analyzed as a capacitor with one plate to the ground and the other to the oscilloscope channel, with the piezoelectric film being the semiconductor in between the two plates. Although it might be obvious for the reader, is important to emphasize that this capacitor represents just one node, i.e. an intersection between a vertical bottom electrode and a horizontal top electrode.

After the initial value reading, the pressure was incremented approximately every 5 psi and up to 80 psi (551.6 kPa). Every observation was recorded and tabulated in table XIV, under the “Raw Signal Output” column. The expectation from this experiment was to evaluate the relationship between the pressure and the output voltage. The results show, indeed, that the output voltage increases linearly as the pressure increases. Although simple, these results are important since provide evidence that the sensor is behaving as expected and the contact pressure information is there.

TABLE XIV. ISOLATED SENSOR CHARACTERIZATION DATA

| Compressed air Pressure (psi) | Compressed air Pressure (kPa) | Raw Signal Output (mV) |
|-------------------------------|-------------------------------|------------------------|
| 20 | 137.9 | 128 |

| Compressed air Pressure (psi) | Compressed air Pressure (kPa) | Raw Signal Output (mV) |
|-------------------------------|-------------------------------|------------------------|
| 25 | 172.4 | 140 |
| 30 | 206.8 | 160 |
| 35 | 241.3 | 170 |
| 40 | 275.8 | 180 |
| 45 | 310.3 | 200 |
| 50 | 344.7 | 210 |
| 55 | 379.2 | 240 |
| 60 | 413.7 | 260 |
| 65 | 448.2 | 280 |
| 70 | 482.6 | 310 |
| 75 | 517.1 | 330 |
| 80 | 551.6 | 350 |

An important aspect from Table XIV is the pressure value that is referred in the first two columns: they both correspond to the pneumatic pressure actuating on the test fixture, the first reported in psi units while the second is converted to kPa (SI units). This clarification is important since those pressure values should not be confused with the mechanical deformation the sensor will associate with the output voltage. In this matter, the third column has the output voltage generated as a result of the polarization in the piezo, which as per Eq. (2.5.1) will result because of the mechanical stress.

Despite the sensor output seems to be working properly, the output signal is not being maintained over a period of time, as it should normally do. Instead, the signal disappears. In fact, the values written in Table XIV are the highest peak values observed and quickly the signal went back to noise. Even though a normal oscillation is expected at the beginning, as normally happens with data acquisition systems, it is also expected that the amplitude of this oscillation decreases down to a steady and final signal, which would be the true sensor value. Figure 4.3.3 shows an example of the signal form that is expected.

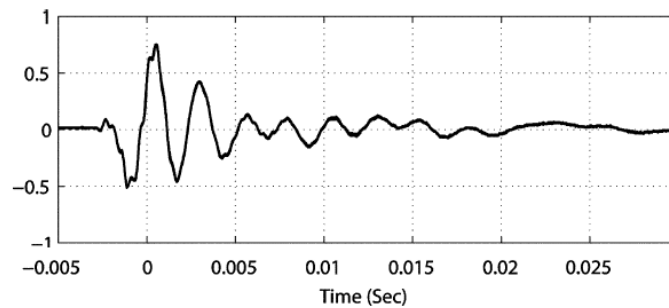


Figure 4.3.3. Laser Doppler vibrometer signal read example for piezoelectric placed on a cantilever beam [87].

Conversely to Figure 4.3.3, the output signal registered by the oscilloscope (same result using Fluke Industrial Scope Meter 125 model and SainSmart DDS-120 model) changed when the pressure on the instrument was applied but rapidly decreased down to the value of the oscillation before the pressure peak was observed. In other words, the mean value of the signal should maintain a certain difference from the mean value before the pressure has been applied. However, this is not the case and the signal is getting back in the noise portion very quickly without being able to sustain. Figure 4.3.4 illustrates the situation.

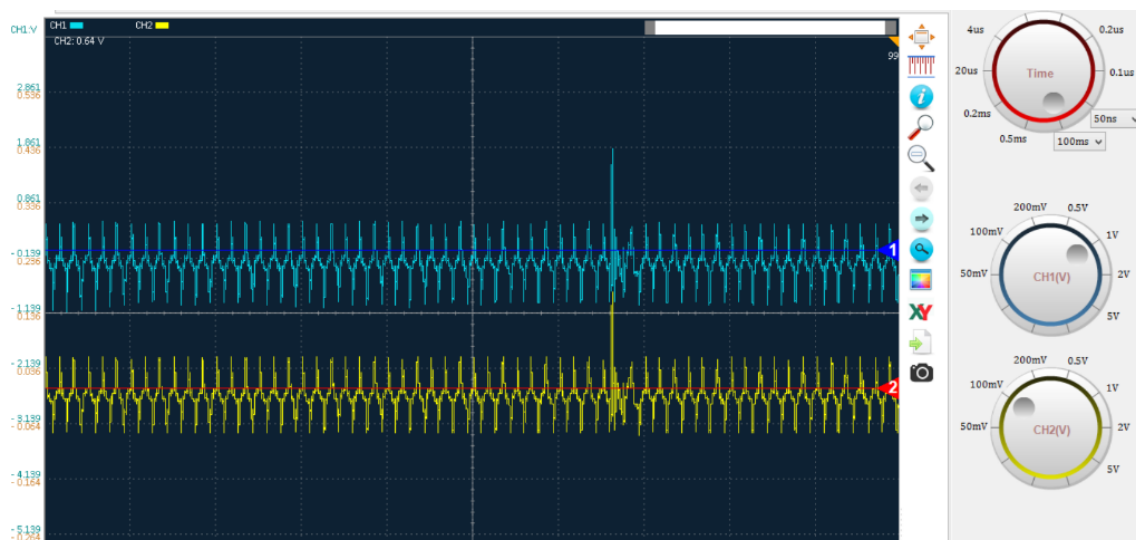
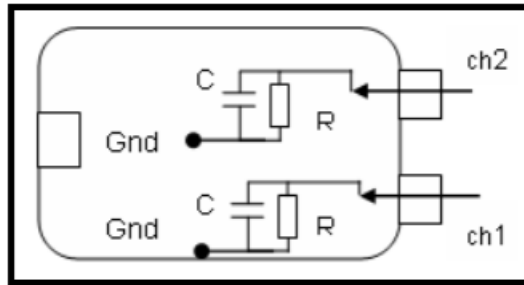


Figure 4.3.4. Source signal from sensor (yellow) and the corresponding amplified value.

The deviation from what is expected can be attributed to the equivalent circuit within the oscilloscope, because of the internal RC circuit discharges the capacitor formed by the sensor. Another cause might be the small charge resulted from the polarization effect happening on the piezoelectric film. In fact, a very small charge or a very small polarization on the piezo combined with the equivalent impedance from the RC circuit within the scope meter, could potentially explain the rapid loss of the signal. Figure 4.3.5 is extracted from the SainSmart oscilloscope manufacturer datasheet and shows the device internal structure and the corresponding RC values.



DDS-120 Top View, $R=1M \Omega$, $C=25pF$

Figure 4.3.5. SainSmart oscilloscope DDS-120 model device structure.

While still suspecting about the low charge from the piezo, is not very practical to validate. In addition, the high peak observed when the pressure is applied, leads to think the piezo is actually generating a strong signal. However, the issue here is the difficulty to keep the signal up to a readable value. One of the things that was tried to maintain the signal, was to connect a voltage follower operational amplifier in between the sensor output and the DAQ board, however, this was done using prototypes circuit boards and saturations issues in the amplifiers made difficult to obtain the expected results. Thus, solving the saturations issues on DAQ board must be the first next step in order to perform further tests on the sensor. In fact, adding this voltage follower as a new component to the DAQ board is recommended for a second revision of the system, in the final chapter, more in this matter will be addressed.

4. Results from directly measuring the output of one single node from the DAQ board: Now that has been demonstrated that separately, the sensor and DAQ board are both functional, the same experiment has been conducted putting together the sensor and the DAQ board. The same sensor node was measured with both channels of the oscilloscope as well: channel 1 connected to the signal coming out of the sensor and channel 2 connected to the output of the op amplifier. Figure 4.3.6 illustrates the corresponding circuit for better understanding.

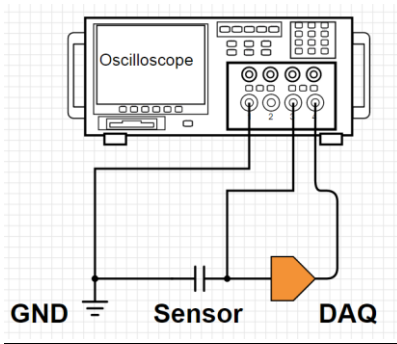


Figure 4.3.6. Schematic for one node sensor output reading when adding the DAQ board.

Now both channels are taking data from the system, one from the sensor and the other from the DAQ board. For the readings in channel 1, the observations are expected to be very similar to the ones recorded in the previous test case, since the measuring location is the same: *the raw output from the sensor*. The method followed was the similar, at first, the compressed air pressure was set at 20 psi and then incremented every 5 psi to record the data in between. Table XV has the result of those measures in the “Source Signal Output” and “Amplified Signal Output” columns. A final column is added to calculate the experimental gain factor from the op amp relative to the theoretical gain factor of 1:10. In addition, the “Raw Signal Output” from the previous experiment was kept in order to compare results.

TABLE XV. SENSOR WITH DAQ BOARD CHARACTERIZATION DATA

| Pressure (psi) | Pressure (kPa) | Raw Signal Output (mV) | Source Signal Output (mV) | Amplified Signal Output (V) | Op Amp Gain Factor |
|----------------|----------------|------------------------|---------------------------|-----------------------------|--------------------|
| 20 | 137.9 | 128 | 150 | 2.0 | 13 |
| 25 | 172.4 | 140 | 160 | 2.3 | 14 |
| 30 | 206.8 | 160 | 180 | 2.5 | 14 |
| 35 | 241.3 | 170 | 200 | 2.7 | 14 |
| 40 | 275.8 | 180 | 230 | 3.0 | 13 |
| 45 | 310.3 | 200 | 240 | 3.2 | 13 |
| 50 | 344.7 | 210 | 260 | 3.4 | 13 |
| 55 | 379.2 | 240 | 280 | 3.6 | 13 |
| 60 | 413.7 | 260 | 300 | 3.8 | 13 |
| 65 | 448.2 | 280 | 320 | 4.0 | 13 |
| 70 | 482.6 | 310 | 340 | 4.1 | 12 |
| 75 | 517.1 | 330 | 360 | 4.2 | 12 |
| 80 | 551.6 | 350 | 380 | 4.3 | 11 |

The first and most interesting aspect from Table XV is the offset between the “Raw Signal Output” and “Source Signal Output”, which by the definition should be very close to each

other. Basically because both are measured at the same location: *the sensor output*. In order to gain insight of the meaning of this offset, both columns are plotted as functions of the pressured of compressed air applied. Figure 4.3.7 shows the graphical relationship.

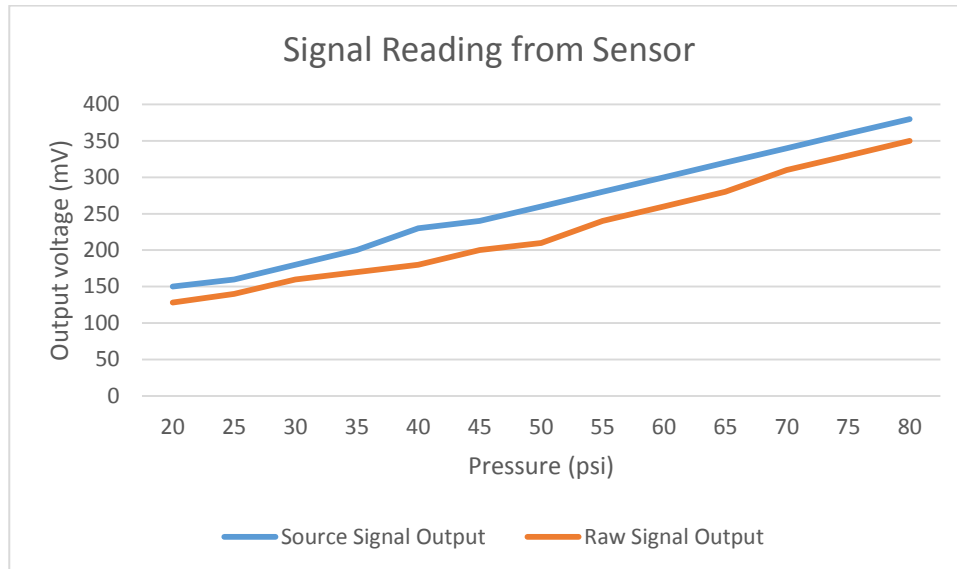


Figure 4.3.7. Graphical representation of both series: the data from the sensor when no DAQ board is connected (orange) and the data from the sensor but when connecting the DAQ as a second channel to the oscilloscope (blue).

The offset seen in the plot from Figure 4.3.7 is an interesting finding because it demonstrates a difference in the sensor output when measuring one way or another. This data is helpful for calibration considerations, since the offset can be potentially thought of a calibration factor for reading corrections. Taking the average difference between both sets of data, the mean offset for the sensor reading is **34 mV**.

To this point, it has been widely discussed how an external pressure from compressed air generates a certain amount of voltage out from the piezoelectric sensor. It might be confusing, however, to discuss the differences between an external pressure and the mechanical stress produced in the piezo as a response of such external pressure. In other words, the external pressure will produce a mechanical stress (measured also in the same units) that will translate to a voltage signal. The fact of having both, the external pressure and the mechanical deformation, in the same units of measure, makes it a little more confusing. Thus, it is necessary to understand the equivalence of the output voltage with the mechanical deformation happening within the piezoelectric as a result of the external pressure. For this, equations from chapter 2 can be recalled, where Eq. (2.5.3) gives the polarity generated as a

result from the mechanical stress, and Eq. (2.5.4) gives the polarity as function of the generated voltage. Therefore, both equations can be rearrange and written as,

$$\sigma = \frac{D}{d_{33}} \quad (4.3.1)$$

Where σ represents the mechanical stress, usually in MPa, D is the polarity induced in the piezoelectric and d_{33} is the piezoelectric coefficient in the z-direction. In addition, the polarity can be expressed as,

$$D = \frac{V\varepsilon_{33}}{t} = \frac{V\varepsilon_{PVDf}\varepsilon_0}{t} \quad (4.3.2)$$

Where t is the thickness of the piezo film, V is the voltage generated and measured by the experimental setup, ε_{PVDf} is the dielectric constant of the piezo film as per manufacturer data and ε_0 is the free space or vacuum permittivity.

Lastly, combining Eq. (4.3.1) and Eq. (4.3.2), the correlation between output voltage and mechanical stress can finally be found.

$$\sigma = \frac{V\varepsilon_{PVDf}\varepsilon_0}{td_{33}} \quad (4.3.3)$$

Eq. (4.3.3) is highly important as it allows correlate the voltage recorded by the oscilloscope and examining how much stress this voltage. In fact, correlating those values also allows starting the verification analysis regarding the computational analysis conducted in Chapter 3. Table XVI shows the results of solving Eq. (4.3.3) for each generated voltage that was recorded in Table XV.

TABLE XVI. MECHANICAL DEFORMATION EXPRESSED AS THE STRESS INDUCED BY AN EXTERNAL PRESSURE APPLIED TO THE SENSOR.

| Raw Signal Out (mV) | Source Signal Out (mV) | Mechanical deformation (MPa) |
|---------------------|------------------------|------------------------------|
| 128 | 150 | 59.21 |
| 140 | 160 | 64.77 |
| 160 | 180 | 74.02 |
| 170 | 200 | 78.64 |
| 180 | 230 | 83.27 |
| 200 | 240 | 92.52 |

| Raw Signal Out (mV) | Source Signal Out (mV) | Mechanical deformation (MPa) |
|---------------------|------------------------|------------------------------|
| 210 | 260 | 97.15 |
| 240 | 280 | 111.03 |
| 260 | 300 | 120.28 |
| 280 | 320 | 129.53 |
| 310 | 340 | 143.41 |
| 330 | 360 | 152.66 |
| 350 | 380 | 161.91 |

Now, it is possible to examine the results from the finite element analysis with the recently data shown in Table XVI. It is important to remember, though, that when building the model for the finite element analysis, the force applied to the instrument was considered as a result of the distance increments and the force was increased slowly as the distance decreased. In contrast, the force is suddenly applied in the experimental arrangement and actually there is some linear momentum added to the system. This difference is important to keep in mind when examining Figure 4.3.8, which shows the results from the finite element analysis and the results from the experimental data.

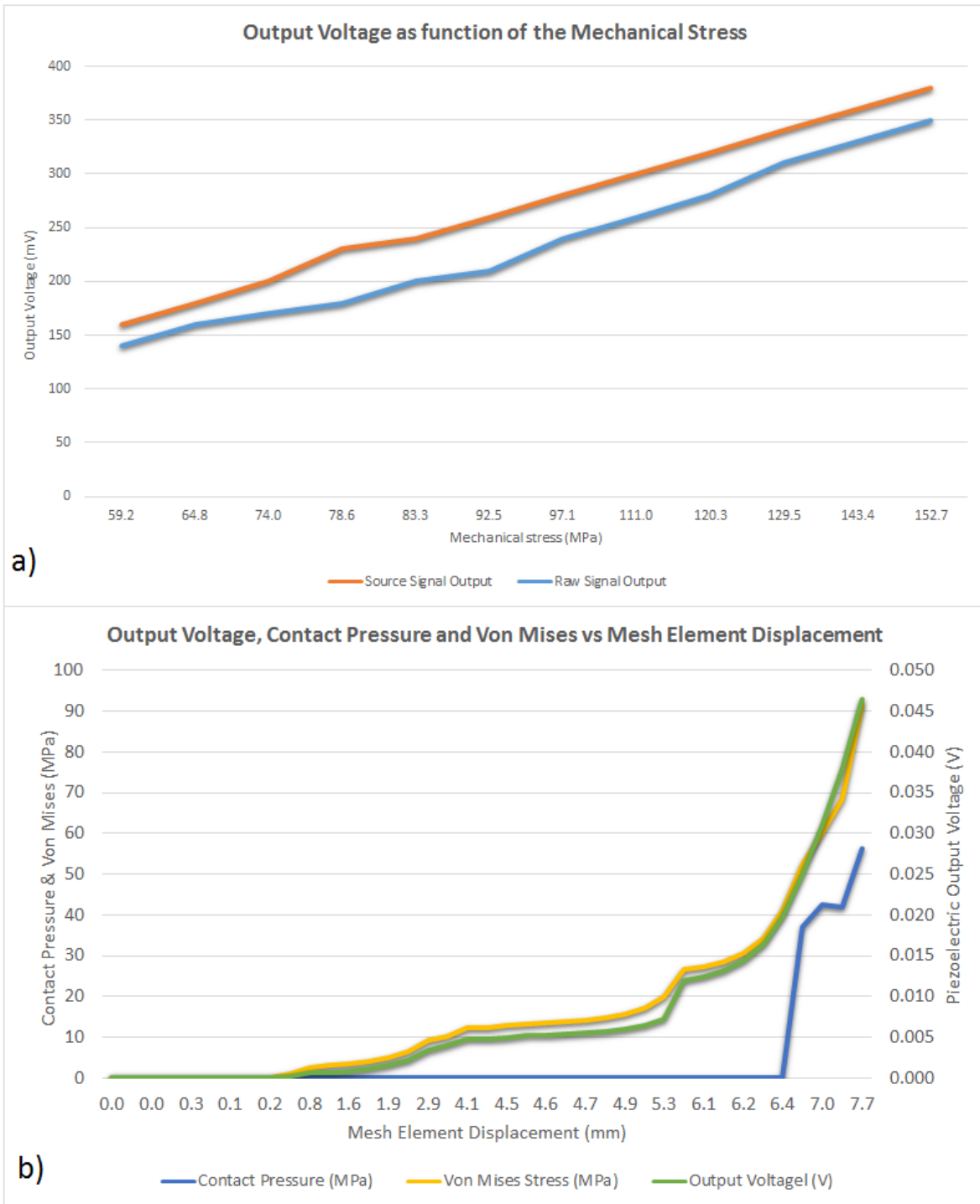


Figure 4.3.8. Graphical comparison between a) experimental data gathering and b) Computational analysis results.

Despite both graphs are quite different, with some help it can be noticed the output voltage is considerable different from the computational analysis and the experimental data. By looking at the end of the green series in Figure 4.3.8b), the maximum voltage reading is

expected to be close to 45 mV for about 90 MPa of mechanical stress in the piezo, whereas at the equivalent mechanical stress, the reading in the experimental arrangement is between 200 mV and 250 mV, depending on the series evaluated from the graph shown in figure 4.3.8a). As discussed recently, the offset between these two sets of data can be analyzed as a correction factor for the DAQ system, which will lead to choose the 200 mV as the corrected value. Under this assumption, the experimental results are **4.4 times** bigger than the numbers given by the computational analysis. One potentially explanation for such a difference lies in the inability for the measurement system to maintain the signal value after the initial oscillation. This step response in the measurements led to record the peak on each observation, which is expected to be substantially bigger than the attenuated value. In fact, upon the correct functionality, the sensor must sustain the signal value while the mechanical deformation and the external force are still applied. Anticipating some thoughts on the conclusions for this work, the data gathered within this test case is not suitable for direct validation of the FEA results.

Some more information was gathered during this experiment, found on the last two columns in Table XIV. Plotting the amplified signal that was also measured and recorded under the “amplified signal output” column lead to an interesting finding that is addressed by examining Figure 4.3.9.

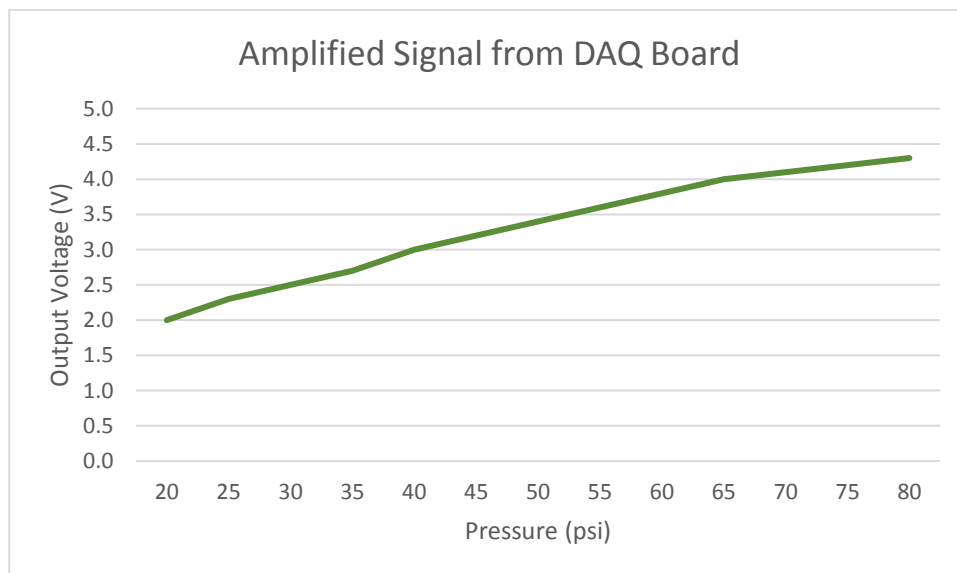


Figure 4.3.9. Graphical representation for the amplified signal from the DAQ board.

In more detail, there is a saturation closeness observed in Figure 4.3.9 where the values tend to saturation when higher pressure values are applied and the amplifier slope starts decreasing to a more horizontal line. This is a typical behavior from operational amplifiers, and it is also important to mention, that the pressure range at which the sensor is supposed to operate is not even close to such high values applied in this experiment. In fact, the nominal value for the sensor to operate is equivalent to 48 psi of compressed air pressure (330.9 kPa and 10.5 N of force), as it has been widely discussed, therefore it is not expected to use the sensor for inputs much greater than this. Moreover, if the force nominal value is increased by a 20% (~15 N) the equivalent compressed air pressure needed is about 60 psi, which as seen by Figure 4.3.8 is still within the safe range of the amplifier. This operational range for the sensor is a key output of this work.

Additionally, it was noticed that the operational amplifier also saturates when disconnecting the channel one from the circuit in Figure 4.3.6, and goes back to normal immediately as the channel 1 is connected again acting as some kind of coupled circuit that increases the impedance as one component is disconnected, causing the amplifiers to saturate. This is also a potential cause for the entire system to fail when working all wired together, from experimental test case #1.

5. Manually reading each row and each column with the corrected grounded connections:

From all the testing, results and discussion so far, it is demonstrated that extracting the information from the sensor will require further analysis. And although some more work needs to get done in order to extract the data more efficiently, the main thesis objective is to design and implement a sensor that works and also to provide a conclusion on whether or not the technology can be used for a finished product. Under this line of thought, it has been demonstrated that the sensor is working and the data is being generated accordingly to the piezoelectric principles. The aim of this last test case is, then, to provide a final piece of evidence of the sensor output. The experiment setup is in general very similar to the previous one with a couple of important differences:

The two channels of the oscilloscope are connected in the same way, channel number one to the sensor direct output and channel number two to the amplified signal coming from the amplifier. However, only the data from the amplified channel was recorded this time.

Only one trace was plugged to the DAQ board inputs, the rest of each line was connected to ground. This was done for each line of both electrodes. In other words, the data collected in this experiment is either a column or a row, depending on which electrode was connected.

The external compressed air pressure was fixed approximately at 48 psi (330.9 kPa) to generate a force of 10.5 N as determined and discussed in Chapter 3.

At the end, two matrices were recorded, one for the rows and one for the columns. And finally, one single matrix is obtained by taking the average between the rows and the columns, as intersection points. The following expression is intended to provide better understanding of the data gathering,

$$n_{averaged} = \frac{n_{rows} + n_{columns}}{2} \quad (4.3.4)$$

where the n_{rows} and $n_{columns}$ are the observed data from the experiment, while $n_{averaged}$ is the result of taking the average between the two gathered values. Taking the average between the row and column observation obeys a fully experimental approach, as there is no theoretical note on how collect the data from this sensor. Other thoughts on this were to take the absolute difference between the values but the resulting data had no sense at all. Same scenario when trying to sum both, rows and columns, the resulting magnitude of the data was just too high for the application to make sense. Basically, this is how it was found that when taking the average between the columns and the rows, the data took an interesting shape resembling the instrument contact surface, which is why, the data is presented in this way.

The intention of this extensive experiment is attempt a 3D surface plot comprised by every single node on the sensor. Table XVII shows the entire array of values taking from the average of the rows and columns, by using Eq. (4.3.4). Moreover, the values observed in table XVII correspond the amplified voltages, in table XVIII, the same values will be translated to the corresponding mechanical stress as it was addressed in the test case #4, by using Eq. (4.3.3).

TABLE XVII. FULL RESOLUTION MEASUREMENT FOR THE SENSOR, AVERAGED VOLTAGES VALUES ON EACH NODE FROM THE COLUMNS AND ROWS.

| | | x- coordinates (mm) | | | | | | | | | | | | | | | | |
|---------------------|-------|---------------------|-------|-------|-------|-------|-------|-------|-------|-------|-------|-------|-------|-------|-------|-------|-------|-------|
| | | 1 | 3 | 5 | 7 | 9 | 11 | 13 | 15 | 17 | 19 | 21 | 23 | 25 | 27 | 29 | 31 | 33 |
| y- coordinates (mm) | 1 | 0.010 | 0.862 | 0.842 | 0.995 | 1.148 | 0.845 | 1.203 | 1.386 | 1.292 | 1.468 | 1.635 | 0.768 | 0.579 | 0.384 | 0.329 | 0.487 | 1.037 |
| | 3 | 0.327 | 1.179 | 1.159 | 1.312 | 1.464 | 1.161 | 1.519 | 1.703 | 1.608 | 1.785 | 1.951 | 1.084 | 0.896 | 0.701 | 0.645 | 0.803 | 1.353 |
| | 5 | 0.232 | 1.084 | 1.064 | 1.217 | 1.369 | 1.066 | 1.424 | 1.608 | 1.513 | 1.690 | 1.856 | 0.989 | 0.801 | 0.606 | 0.550 | 0.708 | 1.258 |
| | 7 | 0.113 | 0.965 | 0.945 | 1.098 | 1.251 | 0.948 | 1.306 | 1.489 | 1.395 | 1.571 | 1.738 | 0.871 | 0.682 | 0.487 | 0.432 | 0.590 | 1.140 |
| | 9 | 0.248 | 1.100 | 1.080 | 1.233 | 1.385 | 1.082 | 1.440 | 1.624 | 1.529 | 1.706 | 1.872 | 1.005 | 0.817 | 0.622 | 0.566 | 0.724 | 1.274 |
| | 11 | 0.121 | 0.973 | 0.953 | 1.106 | 1.259 | 0.956 | 1.314 | 1.497 | 1.403 | 1.579 | 1.746 | 0.879 | 0.690 | 0.495 | 0.440 | 0.598 | 1.148 |
| | 13 | 0.137 | 0.989 | 0.969 | 1.122 | 1.274 | 0.971 | 1.329 | 1.513 | 1.418 | 1.595 | 1.761 | 0.894 | 0.706 | 0.511 | 0.455 | 0.613 | 1.163 |
| | 15 | 0.836 | 1.688 | 1.668 | 1.821 | 1.973 | 1.670 | 1.361 | 1.545 | 1.450 | 1.627 | 1.793 | 1.593 | 1.405 | 1.210 | 1.154 | 1.312 | 1.862 |
| | 17 | 0.867 | 1.719 | 1.699 | 1.852 | 2.005 | 1.702 | 1.393 | 1.576 | 1.482 | 1.658 | 1.825 | 1.625 | 1.436 | 1.241 | 1.186 | 1.344 | 1.894 |
| | 19 | 1.366 | 2.218 | 2.198 | 2.351 | 2.504 | 2.201 | 1.892 | 2.075 | 1.981 | 2.157 | 2.324 | 2.124 | 1.935 | 1.740 | 1.685 | 1.843 | 2.393 |
| | 21 | 0.984 | 1.836 | 1.816 | 1.969 | 2.122 | 1.819 | 1.510 | 1.693 | 1.599 | 1.775 | 1.942 | 1.742 | 1.553 | 1.358 | 1.303 | 1.461 | 2.011 |
| | 23 | 1.032 | 1.884 | 1.864 | 2.017 | 2.169 | 1.866 | 1.557 | 1.741 | 1.646 | 1.823 | 1.989 | 1.789 | 1.601 | 1.406 | 1.350 | 1.508 | 2.058 |
| | 25 | 0.365 | 1.217 | 1.197 | 1.350 | 1.502 | 1.199 | 1.557 | 1.741 | 1.646 | 1.823 | 1.989 | 1.122 | 0.934 | 0.739 | 0.683 | 0.841 | 1.391 |
| | 27 | 0.270 | 1.122 | 1.102 | 1.255 | 1.407 | 1.104 | 1.462 | 1.646 | 1.551 | 1.728 | 1.894 | 1.027 | 0.839 | 0.644 | 0.588 | 0.746 | 1.296 |
| | 29 | 0.937 | 1.789 | 1.769 | 1.922 | 2.075 | 1.771 | 1.462 | 1.646 | 1.551 | 1.728 | 1.894 | 1.694 | 1.506 | 1.311 | 1.255 | 1.413 | 1.963 |
| | 31 | 2.190 | 3.042 | 3.022 | 3.175 | 3.327 | 3.024 | 2.715 | 2.899 | 2.804 | 2.981 | 3.147 | 2.947 | 2.759 | 2.564 | 2.508 | 2.666 | 3.216 |
| | 33 | 1.771 | 2.623 | 2.603 | 2.756 | 2.909 | 2.606 | 2.297 | 2.481 | 2.386 | 2.563 | 2.729 | 2.529 | 2.340 | 2.145 | 2.090 | 2.248 | 2.798 |
| | 35 | 1.378 | 2.230 | 2.210 | 2.363 | 2.515 | 2.212 | 1.903 | 2.087 | 1.992 | 2.169 | 2.335 | 2.135 | 1.947 | 1.752 | 1.696 | 1.854 | 2.404 |
| | 37 | 1.129 | 1.981 | 2.628 | 2.781 | 2.934 | 2.631 | 2.322 | 1.838 | 1.744 | 1.920 | 2.754 | 2.554 | 2.365 | 2.170 | 2.115 | 1.606 | 2.156 |
| | 39 | 0.624 | 1.476 | 2.123 | 2.276 | 2.429 | 2.126 | 1.817 | 1.333 | 1.239 | 1.415 | 2.249 | 2.049 | 1.860 | 1.665 | 1.610 | 1.101 | 1.651 |
| 41 | 0.389 | 1.241 | 1.888 | 2.041 | 2.193 | 1.890 | 1.581 | 1.098 | 1.003 | 1.180 | 2.013 | 1.813 | 1.625 | 1.430 | 1.374 | 0.865 | 1.415 | |
| 43 | 0.518 | 1.370 | 2.017 | 2.170 | 2.323 | 2.020 | 1.711 | 1.227 | 1.133 | 1.309 | 2.143 | 1.943 | 1.754 | 1.559 | 1.504 | 0.995 | 1.545 | |
| 45 | 0.674 | 1.526 | 2.173 | 2.326 | 2.479 | 2.176 | 1.867 | 1.383 | 1.289 | 1.465 | 2.299 | 2.099 | 1.910 | 1.715 | 1.660 | 1.151 | 1.701 | |
| 47 | 0.713 | 1.565 | 2.212 | 2.365 | 2.518 | 2.215 | 1.906 | 1.422 | 1.328 | 1.504 | 2.338 | 2.138 | 1.949 | 1.754 | 1.699 | 1.190 | 1.740 | |
| 49 | 1.069 | 1.921 | 2.568 | 2.721 | 2.874 | 2.571 | 2.262 | 1.778 | 1.684 | 1.860 | 2.694 | 2.494 | 2.305 | 2.110 | 2.055 | 1.546 | 2.096 | |

There are two crucial aspects to consider after this data has been presented: first, the recently mentioned fact that the voltages values gathered in this experiment correspond to the amplified signal of the DAQ board, and second, the offset or correction factor of 34 mV found during test case #4 when evaluating the performance of the sensor with one just node being measured. The reason because these two factors are important is because the data shown in Table XVI already include the correction factor of 34 mV multiplied by the gain factor of 10 produced but the amplifiers in the DAQ board. More simply stated: a correction factor of 340 mV has been applied to all cells in Table XVII, subtracted from the result of expression (4.3.4). Finally, Figure 4.3.10 translates this data in a 3D surface plot by using the Matlab software (Massachusetts, United States).

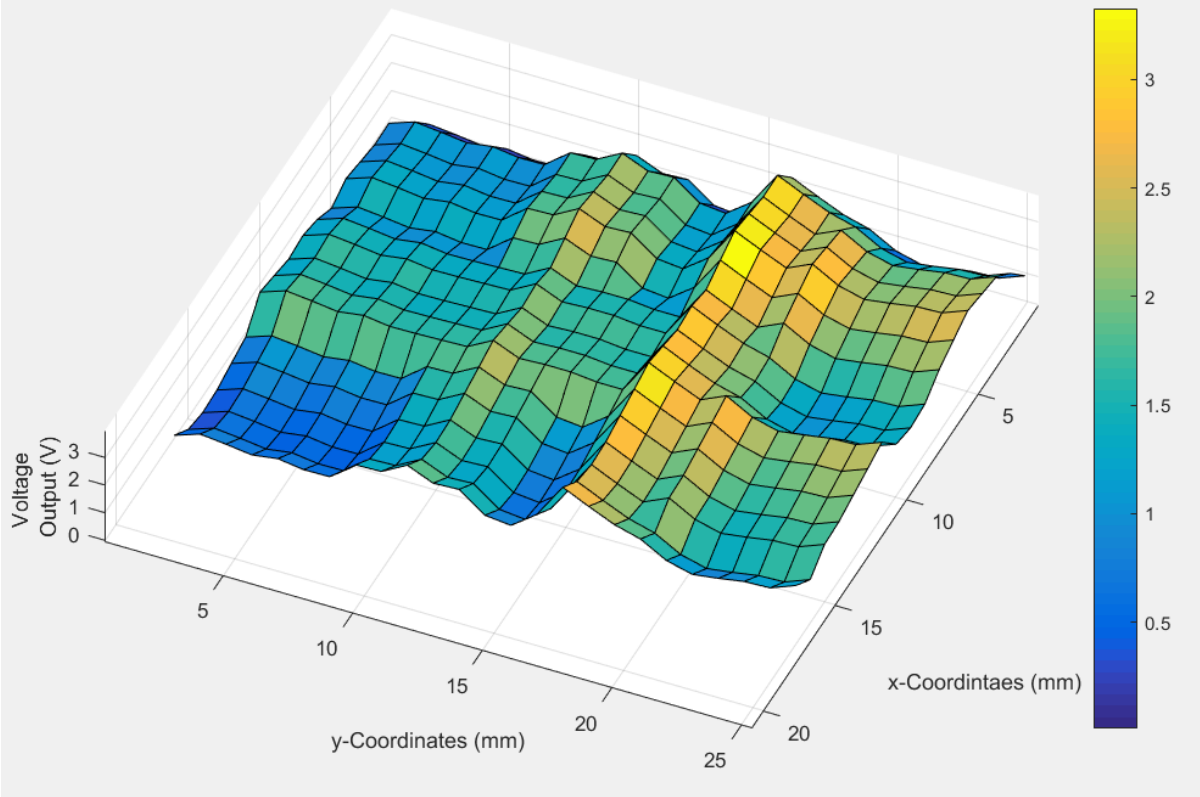


Figure 4.3.10. Entire sensor data collection, surface plot for electrical response, units in V.

The surface generated by the software is the ultimate goal of this thesis work, since it finally depicts the entire sensor response when an external and known pressure is applied. Translating the voltages values to the mechanical deformation according to Eq. (4.3.3). Table XVIII is generated to finally show the true output of the sensor.

TABLE XVIII. FULL RESOLUTION MEASUREMENT, MECHANICAL RESPONSE OF THE SENSOR

| | | x- coordinates (mm) | | | | | | | | | | | | | | | | |
|---------------------|------|---------------------|-------|-------|-------|-------|-------|-------|-------|-------|-------|-------|-------|-------|-------|-------|-------|-------|
| | | 1 | 3 | 5 | 7 | 9 | 11 | 13 | 15 | 17 | 19 | 21 | 23 | 25 | 27 | 29 | 31 | 33 |
| y- coordinates (mm) | 1 | 0.5 | 39.9 | 39.0 | 46.0 | 53.1 | 39.1 | 55.6 | 64.1 | 59.7 | 67.9 | 75.6 | 35.5 | 26.8 | 17.8 | 15.2 | 22.5 | 47.9 |
| | 3 | 15.1 | 54.5 | 53.6 | 60.7 | 67.7 | 53.7 | 70.3 | 78.8 | 74.4 | 82.6 | 90.3 | 50.1 | 41.4 | 32.4 | 29.8 | 37.1 | 62.6 |
| | 5 | 10.7 | 50.1 | 49.2 | 56.3 | 63.3 | 49.3 | 65.9 | 74.4 | 70.0 | 78.2 | 85.9 | 45.8 | 37.0 | 28.0 | 25.4 | 32.8 | 58.2 |
| | 7 | 5.2 | 44.6 | 43.7 | 50.8 | 57.8 | 43.8 | 60.4 | 68.9 | 64.5 | 72.7 | 80.4 | 40.3 | 31.6 | 22.5 | 20.0 | 27.3 | 52.7 |
| | 9 | 11.4 | 50.9 | 49.9 | 57.0 | 64.1 | 50.1 | 66.6 | 75.1 | 70.7 | 78.9 | 86.6 | 46.5 | 37.8 | 28.8 | 26.2 | 33.5 | 58.9 |
| | 11 | 5.6 | 45.0 | 44.1 | 51.2 | 58.2 | 44.2 | 60.8 | 69.3 | 64.9 | 73.0 | 80.7 | 40.6 | 31.9 | 22.9 | 20.3 | 27.6 | 53.1 |
| | 13 | 6.3 | 45.7 | 44.8 | 51.9 | 58.9 | 44.9 | 61.5 | 70.0 | 65.6 | 73.8 | 81.5 | 41.4 | 32.6 | 23.6 | 21.0 | 28.4 | 53.8 |
| | 15 | 38.7 | 78.1 | 77.1 | 84.2 | 91.3 | 77.3 | 63.0 | 71.5 | 67.1 | 75.2 | 82.9 | 73.7 | 65.0 | 56.0 | 53.4 | 60.7 | 86.1 |
| | 17 | 40.1 | 79.5 | 78.6 | 85.7 | 92.7 | 78.7 | 64.4 | 72.9 | 68.5 | 76.7 | 84.4 | 75.2 | 66.4 | 57.4 | 54.8 | 62.2 | 87.6 |
| | 19 | 63.2 | 102.6 | 101.7 | 108.8 | 115.8 | 101.8 | 87.5 | 96.0 | 91.6 | 99.8 | 107.5 | 98.2 | 89.5 | 80.5 | 77.9 | 85.2 | 110.7 |
| | 21 | 45.5 | 84.9 | 84.0 | 91.1 | 98.1 | 84.1 | 69.8 | 78.3 | 73.9 | 82.1 | 89.8 | 80.6 | 71.8 | 62.8 | 60.3 | 67.6 | 93.0 |
| | 23 | 47.7 | 87.1 | 86.2 | 93.3 | 100.3 | 86.3 | 72.0 | 80.5 | 76.1 | 84.3 | 92.0 | 82.8 | 74.0 | 65.0 | 62.5 | 69.8 | 95.2 |
| | 25 | 16.9 | 56.3 | 55.4 | 62.4 | 69.5 | 55.5 | 72.0 | 80.5 | 76.1 | 84.3 | 92.0 | 51.9 | 43.2 | 34.2 | 31.6 | 38.9 | 64.3 |
| | 27 | 12.5 | 51.9 | 51.0 | 58.0 | 65.1 | 51.1 | 67.6 | 76.1 | 71.8 | 79.9 | 87.6 | 47.5 | 38.8 | 29.8 | 27.2 | 34.5 | 60.0 |
| | 29 | 43.3 | 82.7 | 81.8 | 88.9 | 95.9 | 81.9 | 67.6 | 76.1 | 71.8 | 79.9 | 87.6 | 78.4 | 69.6 | 60.6 | 58.1 | 65.4 | 90.8 |
| | 31 | 101.3 | 140.7 | 139.8 | 146.9 | 153.9 | 139.9 | 125.6 | 134.1 | 129.7 | 137.9 | 145.6 | 136.3 | 127.6 | 118.6 | 116.0 | 123.3 | 148.8 |
| | 33 | 81.9 | 121.3 | 120.4 | 127.5 | 134.6 | 120.5 | 106.2 | 114.7 | 110.4 | 118.5 | 126.2 | 117.0 | 108.3 | 99.2 | 96.7 | 104.0 | 129.4 |
| | 35 | 63.7 | 103.1 | 102.2 | 109.3 | 116.3 | 102.3 | 88.0 | 96.5 | 92.2 | 100.3 | 108.0 | 98.8 | 90.0 | 81.0 | 78.5 | 85.8 | 111.2 |
| | 37 | 52.2 | 91.6 | 121.6 | 128.7 | 135.7 | 121.7 | 107.4 | 85.0 | 80.7 | 88.8 | 127.4 | 118.1 | 109.4 | 100.4 | 97.8 | 74.3 | 99.7 |
| | 39 | 28.9 | 68.3 | 98.2 | 105.3 | 112.3 | 98.3 | 84.0 | 61.7 | 57.3 | 65.5 | 104.0 | 94.8 | 86.0 | 77.0 | 74.5 | 50.9 | 76.4 |
| 41 | 18.0 | 57.4 | 87.3 | 94.4 | 101.5 | 87.4 | 73.1 | 50.8 | 46.4 | 54.6 | 93.1 | 83.9 | 75.2 | 66.1 | 63.6 | 40.0 | 65.5 | |
| 43 | 24.0 | 63.4 | 93.3 | 100.4 | 107.4 | 93.4 | 79.1 | 56.8 | 52.4 | 60.6 | 99.1 | 89.9 | 81.1 | 72.1 | 69.6 | 46.0 | 71.5 | |
| 45 | 31.2 | 70.6 | 100.5 | 107.6 | 114.7 | 100.6 | 86.3 | 64.0 | 59.6 | 67.8 | 106.3 | 97.1 | 88.4 | 79.3 | 76.8 | 53.2 | 78.7 | |
| 47 | 33.0 | 72.4 | 102.3 | 109.4 | 116.5 | 102.4 | 88.2 | 65.8 | 61.4 | 69.6 | 108.1 | 98.9 | 90.2 | 81.1 | 78.6 | 55.0 | 80.5 | |

| | | x- coordinates (mm) | | | | | | | | | | | | | | | | |
|---|---|---------------------|------|-------|-------|-------|-------|-------|------|------|------|-------|-------|-------|------|------|------|------|
| | | 1 | 3 | 5 | 7 | 9 | 11 | 13 | 15 | 17 | 19 | 21 | 23 | 25 | 27 | 29 | 31 | 33 |
| 4 | 9 | 49.5 | 88.9 | 118.8 | 125.9 | 132.9 | 118.9 | 104.6 | 82.3 | 77.9 | 86.0 | 124.6 | 115.4 | 106.6 | 97.6 | 95.0 | 71.5 | 96.9 |

After the mechanical deformation has been expressed in terms of the stress at the piezofilm, a similar 3D surface plot is generated. An aspect to remind is that the relationship between the electrical and mechanical response in a piezoelectric material is linear, therefore, the expectation in terms of the shape of the 3D plot is to keep the same contour.

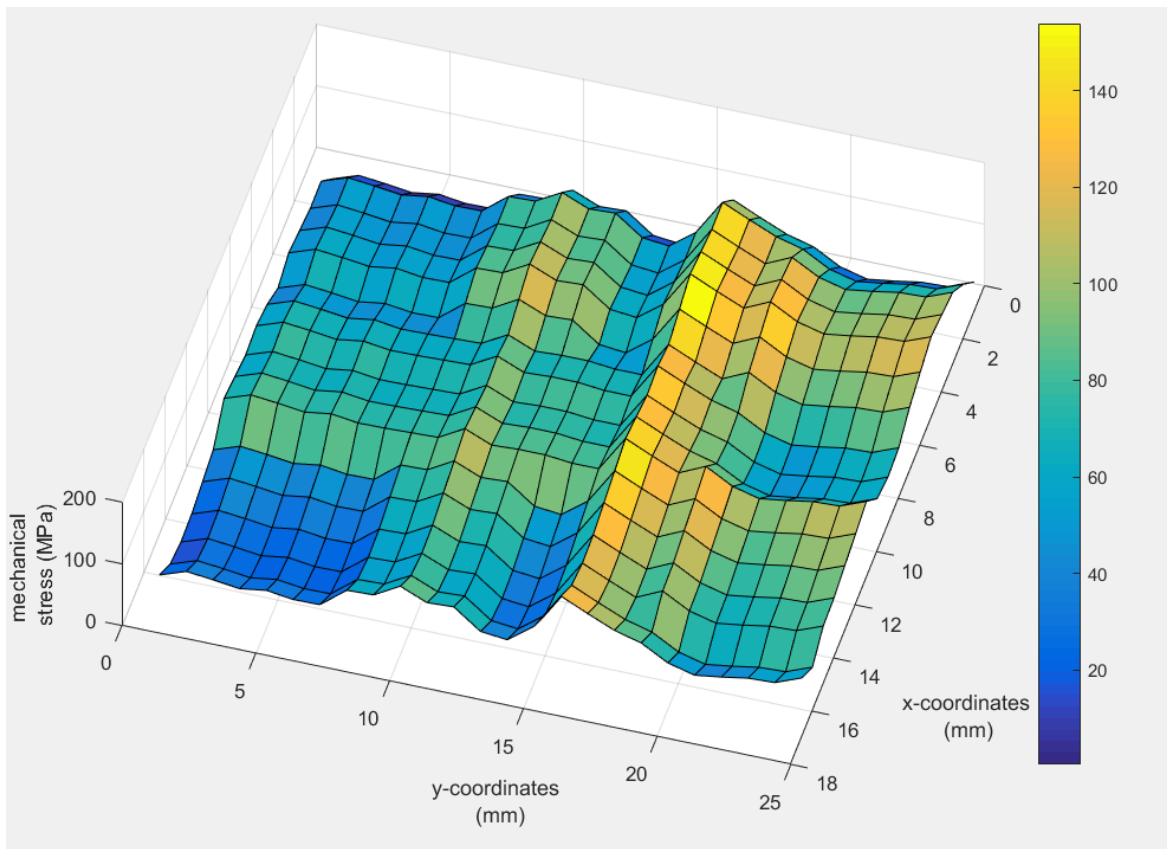


Figure 4.3.11. Entire sensor data collection, surface plot for mechanical response, in MPa.

The most wanted plot is finally generated with the data collected from the sensor and several observations can be related with the results from the FEA model in chapter 3. Prior to that, it is important to highlight the surface plot in Figure 4.3.11 is a “negative” for the contact surface between the instrument and the bone, and although it does not fully match with the true shape of the instrument, the regions of higher stress are correlated with the regions of higher stress in the FEA model as well. Figure 4.3.12 shows the two surfaces of the piezo film, one generated from the experiment and the other one from the FEA model results.

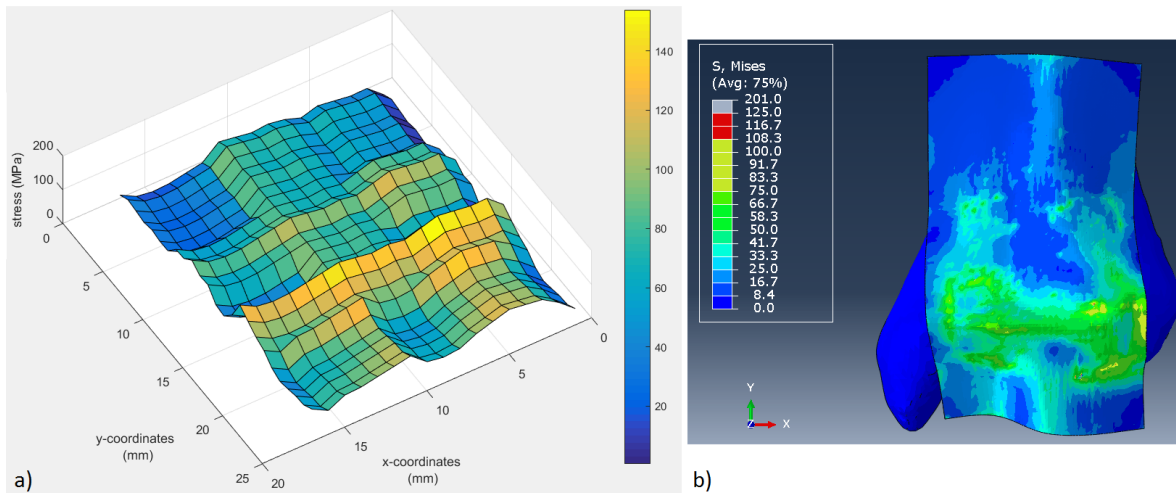


Figure 4.3.12. Piezoelectric film surface plot, a) generated from the experimental data and b) generated by the FEA model results.

An example of the correlation mentioned above, is the central and lower section of the piezoelectric film in both surface plots, where it can be appreciated that the stress is higher and gets concentrated for both cases. Same situation with the middle right and upper central sections, which show considerable lower stress in the surface plot from both, the sensor readings, as well as it does for the contact analysis results in the FEA model. An interesting fact from the experimental fixture is that the instrument is attached to the pneumatic actuator in the upper central section and therefore, it could have been expected more stress produced in that area. However, the experimental data shows otherwise but is actually good, since it follows and verifies the results from the finite element analysis.

More insight from Figure 4.3.12 shows another key aspect that has been discussed to some degree in this work: the magnitude of the mechanical stress translated from the voltage readings compared with the mechanical stress from the Von Mises distribution calculated by the Abaqus software. As discussed in test case #3, the peak voltages recorded are approximately 4.4 bigger than the voltages values from the simulations, which should also be reflected in the stress calculated. This is seen by reviewing the color scale in both surface plots, for example, the experimental data shows stress values close to 150 MPa, while the simulations results show that the higher values are in between 50 to 100 MPa (the green and some yellow portions). This results show a difference rate from 0.5 times to 1.0 time higher mechanical stress from the experimental data. An expected question would be why this

difference is not the same as the 4.4 times in magnitude observed in the voltage readings. The answer to that question relies on the Von Mises stress distribution from the software, which is a distribution that considers the stress from each direction and creates an average as a function of the general state of stress, whereas the stress calculated from Eq. (4.3.3) only considers the effect of the piezo coefficient d_{33} for the z-direction or the thickness of the piezo. Therefore, it can be expected that the true Von Mises distribution with the voltages generated by the sensor get higher than the distribution shown by the Matlab software.

6. Verifying sensor output by inducing an incorrect alignment of the instrument relative to the bone model: To finally complete the testing of the sensor, the instrument was misaligned from the correct position and the same force from test case #5 was exerted on the instrument through the compressed air actuator. The misalignment between the bone and the instrument was measured with a standard goniometer and it was fixed at 20° clockwise. Figure 4.3.13 shows how the instrument was rotated to achieve the 20° of difference between the bone and the instrument.

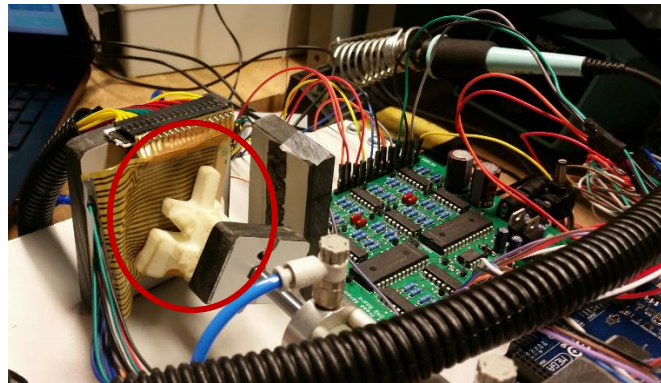


Figure 4.3.13. Rotation of the instrument relative to the bone model fixed position. Angle measured to be 20° clockwise.

Since the instrument was not externally fixed to hold this rotation, eventually it rotates back to the correct position as a response of the force being applied by the pneumatic actuator. However, the measurements were collected upon the initial contact of the misaligned instrument and the bone. That initial peak of voltage was the one recorded for the data gathering of this test case. Besides this difference, the methodology was the same and a table

mostly similar to the ones shown in test case #5 was recorded and the following 3D surface plot was generated as a result.

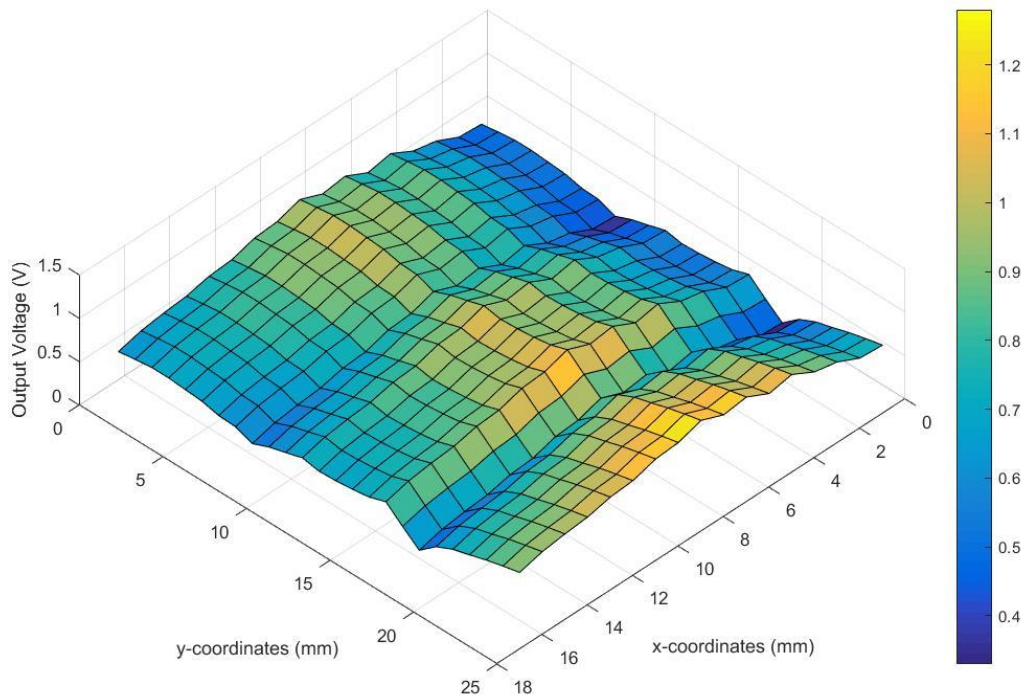


Figure 4.3.14. Pressure map resulting from an incorrect alignment of the patient specific instrument pressed on the bone, with a rotation angle of 20° clockwise.

As seen in Figure 4.3.14, there is no clear pattern of the instrument following the surface of the bone, which is expected since the misalignment mentioned previously. In fact, by looking Figure 4.3.13, it can be seen who the sensor is reading more pressure from the sections under higher bending moments induced by the bad placement of the instrument. The two lower rows located approximately at 9 mm and 19 mm coordinates in the y-axis, correspond to areas of little contact between the two bodies, however, the data from the columns allowed to follow the bending profile of the sensor.

CHAPTER 5

Conclusions and Further Work

5.1 Conclusions

5.2 Future Work

5.1 Conclusions

Three milestones enabled the completion of this thesis work: *need for the application, theoretical background and design implementation*. The first is the Total Ankle Replacement and the patient specific instrumentation background, understanding the application and illustrating the value added by developing a flexible and surface adjustable sensor. Then, the second milestone was achieved by combining the theory from piezoelectric effect, classical mechanics, and MEMS fabrication and modeling techniques; allowing a new design creation through well-known technologies to a fairly new application in the orthopedics market. This milestone was completed when final geometry was designed and when the finite element analysis simulated that geometry. The third and biggest milestone was achieving sensor physical assembly, designing and building a DAQ board system and setting up an experiment using a custom made fixture to perform the testing; this milestone was successfully achieved when generating the surface plot seen in Figure 4.3.13 as the final outcome of this work. In general, a sensor prototype was designed, built and tested by successfully combining the piezoelectric, MEMS and patient specific instrumentation technologies. A considerable amount of testing was carried out in order to obtain data from this sensor, and some particular conclusions can be addressed more specifically:

- The aim of this work is to develop an instrument capable of helping surgeons when placing patient specific instruments onto the bone surface, for Total Ankle Replacement. Through the combination of piezoelectric materials, MEMS techniques, and patient specific instrumentation technology, the sensor was successfully designed and implemented. In addition, several data has been collected to demonstrate this technology combination works and is capable of providing valuable information. This data however, also shows the prototype sensor needs design adjustments and additional work in order

to be used as final product in the healthcare industry. For example, the sensor ability to adopt the surface match region between the bone and the instrument is not ideal for a surgeon to use it in the operating room, as the thickness of the assembled sensor does not allow an easy bending of the sensor and additional effort might be required to install the sensor in between the patient bone and the instrument. In fact, this is the main reason why a test fixture was built, since it was necessary to keep the sensor fixed in the middle of the instrument and the bone. In summary, the sensor is “alive” and generating valuable data for the application, but more work needs to be done in order to have this working as a finished product.

- Regarding sensor prototype construction, the research conducted in this thesis work provides evidence that the combined technology of piezoelectric materials and MEMS fabrication techniques in flexible substrates, can be successfully applied to flexible sensing applications where a contact map needs to be generated. It is also concluded that the mechanical design for this sensor was conservative and the ideal flexibility of the assembled sensor is not achieved. More importantly, the mechanical design using PVDF as the piezoelectric material, *will always result in plastic deformations* since the stress generated by the application is always greater than the yield limit, reported to be **30 MPa** from the manufacturer. These data are shown from three different scenarios: 1. Theoretical design where the stress calculated by the maximum moment was **73.9 MPa** and **111.0 MPa** for two cases analyzed, both higher than the material yield limit. 2. Simulated stress distribution from the FEA analysis where the magnitudes of the stress range between **50 MPa** and **100 MPa** and 3. From the experimental data documented in test case #5 where the stress reaches values as high as **150 MPa**, which is also higher than the yield limit. More simply stated, since the sensor will always operate higher than the elastic limit, it is concluded that the mechanical design for the sensor can be less conservative and thinner piezo films, with thinner copper electrodes and thinner polyamide substrates, should be considered to gain a more surface-adjustable type of sensor. Aligned with the above conclusion, is the sensor resolution. The width of the copper traces for the electrodes needs to be able to provide higher resolution or sensing nodes by unit of area (cm^2 for example), therefore the width needs to be decreased from the current 1.0 mm. This is easily observed in Figure 4.3.13 where the FEA results are compared with the

experimental data through surface plots. In this image, the thick mesh of the built sensor is appreciated.

- The data acquisition system needs to be redesigned to better extract the data from the sensor. Reducing the sensor resolution by connecting ground traces in the same electrode, led to zero reaction from the system and the information from the piezoelectric activity cannot be extracted this way, as explained in section 4.2 and test case #1. One potential explanation relies on electric potential basics, where having an entire array of ground connections next to “sensing” lines all along the column and row electrodes, does not help creating the right conditions for the electrical potential. A probe of this is observed when connecting the sensing lines in one electrode and the ground connections in the electrode on the front, across the piezoelectric film. Despite only one trace was connected as sensing line in the experiment documented in case #5, it can be seen that having ground connections in front helps creating the electric field required for the piezoelectric effect to happen. In summary, when extracting data from the sensor, one entire electrode must be connected to ground and the electrode on the front should be connected to the input of the DAQ board, afterwards, they can change positions in order to extract the information from the other electrode. In fact, the conclusion directly affects the DAQ board design and layout, which should be changed accordingly. Also related to the testing of the sensor, are the signal processing issues, which are independent from the data acquisition system. This is important to clarify since it has been already concluded that a second revision for the DAQ board needs to be carried out; however, the main signal processing issue is that the signal is not being able to sustain in time and rapidly gets decreased to the noise level. Although still unclear, this signal condition must be addressed through a new circuit design from Figure 4.2.2, in fact, in the future work section, a new element is proposed for this circuit, which is a voltage follower intended to stabilize the signal and preventing it from getting lost as capacitance in the sensor array. In summary, the conclusion is that the DAQ board second revision should not only be in terms of the ground and input connections, but also in terms of how provide stability for the signal generated by the sensor.
- In terms of the sensor scope of providing a pressure map from the contact interaction between the bone and the patient specific instrumentation, is concluded that the prototype

developed provides a significant difference in the output of the pressure map when the patient specific instrumentation is incorrectly pressed onto the bone surface, while properly resembling the patient specific instrument shape when pressed correctly. This is clearly appreciated in Figures 4.3.12 and 4.3.14, where two map pressures are shown as a result of the contact interaction of the bone and patient specific instrumentation. Moreover, by looking at these two surface plots, the shape of the patient specific instrumentation can be observed by Figure 4.3.12, whereas Figure 4.3.14 shows a 3D surface plot with no defined shape at all. This particular result is important as it leads to conclude the sensor developed can successfully determine the positioning of the instrument relative to the bone. As part of this scope verification, the contact interaction between the bone and the patient specific instrumentation was also evaluated through finite element computational analysis, where two result groups are provided: first is the electrical response of the experimental data relative to the electrical response predicted by the computational model, here an extremely high difference is found (4.4 times) and it can be attributed to the values recorded in the experiment, since those observations were actually peak values of the piezoelectric effect but the true steady signal could not have been seen according to the experiment setup. Therefore, the conclusion left to consider is that there is not true evidence for comparing the results of the simulations relative to the experimental data, and is needed a more reliable signal acquisition system to fully validate the computational analysis. The second subgroup however, is the comparison between the Von Mises stress distribution of the piezo film in the FEA model with the normal stress distribution obtained in the 3D surface plot from Figure 4.3.12. Despite this surface plot was constructed by using the peak values observed by the experimental setup, the correction or calibration factor of 340 mV could have helped smoothing the values and enable a similar distribution with respect to the finite element analysis.

Finally, upon these conclusions, the reader is encouraged to read a quick guideline for conducting the design change and lastly, several recommendations to consider regarding taking this research to the next level, in the future work section.

5.2 Future work

A quick reference guide to evaluate the design changes proposal is presented below, in order to provide a clear horizon on what things could be changed to achieve a new set of results from a reinforced designed:

Piezoelectric film thickness: There are copolymers films with piezoelectric properties from companies such PIEZOTECH that offers thin layers of 12 μm , which would be interesting to evaluate in this application. Upon this change, finite element analysis must be performed again to compare results.

Thickness reduction in other sensor layers: It would be valuable to examine copper thickness reduction since the electric charge is not expected to have a considerable high value. In addition, reduction of the width of the trace is also something interesting to evaluate, since it will provide higher resolution for the sensor and better results would be available.

Pitch reduction or distance between the copper traces in the electrodes: there is not a number or equation to calculate an optimal pitch distance, but is definitely recommended to the decrease the current distance and gain some more insight on the pressure map.

Data acquisition system second revision: The research efforts should also be concentrated on providing stability to the signal value and finally be able to read a sustainable value for the electrical response. Figure 5.2.1 illustrates a proposal on how redesign the DAQ board in order for this to happen. However, it is strongly recommended to run some circuit simulations or to build this circuit in a prototype board first, prior to have the second revision manufactured and soldered.

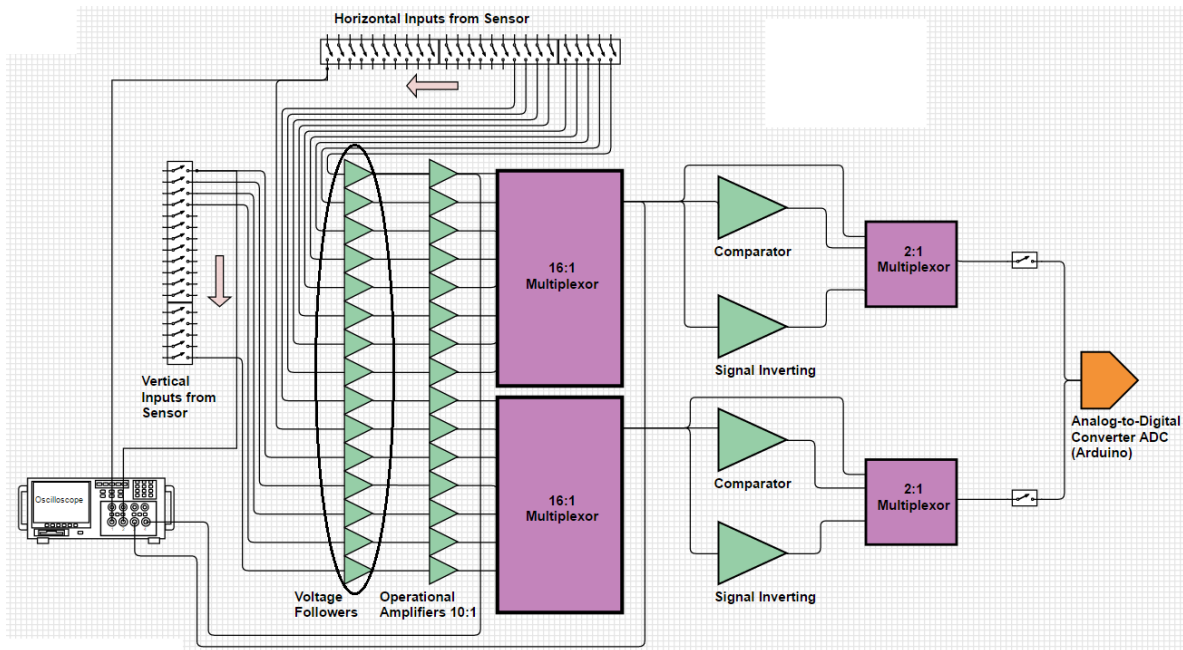


Figure 5.2.1. Proposed DAQ block diagram to include voltage followers to each signal and remove the ground connections from the sensor inputs.

Additionally, Figure 5.2.1 also includes removing the ground connections for the sensor inputs and the sensors are connected directly to the amplifiers, however, this arrangement would still need to collect the data in two steps: a first one for the columns, and a second one for the rows. Some sort of multiplexing would be worth it to examine, to understand if the inputs can be interchangeable between ground and actual live sensor connections. As a final closure to this thesis, some important considerations are discussed for further work relative to this research. When this project was originally conceived, the goal was to create a final released product or functional prototype. Now, after a final prototype has been successfully designed, manufactured, tested and partially debugged, there is still a very long way to go to close the gap between this prototype and a final market product. This is particularly more difficult since dealing with the medical device industry, which has very restrict regulations for all products under development and for all of those who try to place them in the market for human use.

Under that consideration, it is necessary to address some of the challenges for this research to become a final use product. Assuming that upon all the implementations discussed earlier at the beginning of this section, the performance from the sensor is effectively enhanced, all the wiring in between the sensor and the DAQ system needs to be revised, since there is no

actual possibility for the sensor and other components to get sterilized in order to be used in a controlled environment such as the operating room, which also needs a material analysis to verify the components are not degraded because of a sterilization process. Beyond this, design controls should be addressed as per international regulation such as FDA and ISO-13485, where design validations are performed in order to create a device history file that responds to the product design traceability. Consequently, manufacturing processes would need to be considered upon design validation and then the concept of process validation is also included in the equation, for instance, the packaging process to comply with regulatory affairs. Also, it must be determined whether or not clinical data is needed to provide functional evidence for the product submission. On top of these regulation related topics, further market investigations are part of the eventual further work and feedback from the surgeons and field agents is needed to close the gap between design output and true customer requirements, such as the operating room (OR) handling of the device.

Despite it might be some more questions that need to be answered if a market launch is being planned for this device, the above statement intends to provide a general guideline and a starting point to approximate or to guide further research on this topic.

Way beyond this thesis scope, an automatic placing fixture could be thought for robotic placement of the patient specific instrumentation, equipped with pneumatic actuation to press the instrument onto the bone, with the correct electronic packaging for all the circuits and wiring, and with the sensor automatically sending a go/no-go flag when the surface generated actually resembles the expected correct placement of the instrument, and afterwards the drilling could also be performed by this automatic fixture, in the same robotic fashion. Actually, this system could potentially take the patient specific instrumentation to whole new level. However, this is solely a nice to have though that is deep into the future.

Bibliography

- [1] Bone and Joint Initiative, USA. What is the Impact of Burden of Musculoskeletal Disorders and Why is the U.S. Bone and Joint Initiative Important?. 2015 [Online]. Available at: http://www.boneandjointburden.org/docs/USBJI%20MSK%20Impact%20Statement_2015_Revised%2011%2002%2015.pdf. [Accessed 5 - NOV - 2016].
- [2] Tibesku, C. O., Hofer, P., Portegies, W., Ruys, C. J. M., & Fennema, P. (2013). Benefits of using customized instrumentation in total knee arthroplasty: results from an activity-based costing model. *Archives of Orthopaedic and Trauma Surgery*, 133(3), 405–11. doi:10.1007/s00402-012-1667-4
- [3] Leszko, F., Komistek, R. D., Mahfouz, M. R., Ratron, Y.-A., Judet, T., Bonnin, M., ... Lin, S. S. (2008). In vivo kinematics of the salto total ankle prosthesis. *Foot & Ankle International*. / American Orthopaedic Foot and Ankle Society [and] Swiss Foot and Ankle Society, 29(11), 1117–25. doi:10.3113/FAI.2008.1117
- [4] Labek, G., Thaler, M., Janda, W., Agreiter, M., & Stöckl, B. (2011). Revision rates after total joint replacement: cumulative results from worldwide joint register datasets. *The Journal of Bone and Joint Surgery. British Volume*, 93(3), 293–7. doi:10.1302/0301-620X.93B3.25467
- [5] Leardini, a, O'Connor, J. J., Catani, F., & Giannini, S. (1999). Kinematics of the human ankle complex in passive flexion; a single degree of freedom system. *Journal of Biomechanics*, 32(2), 111–8.
- [6] Theofilou, P., & Panagiotaki, H. (2012). *Trauma & Treatment The Association between Musculoskeletal Disorders and Quality of Life*, 1(1), 1–2.
- [7] Leardini, Alberto. O'Connor, John. Catani, Fabio. Giannini, S. (2004). *Mobility of the Human Ankle and the Design of Total Ankle Replacement*.
- [8] Espinosa, N., Walti, M., Favre, P., & Snedeker, J. G. (2010). Misalignment of total ankle components can induce high joint contact pressures. *The Journal of Bone and Joint Surgery. American Volume*, 92(5), 1179–87. doi:10.2106/JBJS.I.00287
- [9] Leszko, F., Komistek, R. D., Mahfouz, M. R., Ratron, Y.-A., Judet, T., Bonnin, M., ... Lin, S. S. (2008). In vivo kinematics of the salto total ankle prosthesis. *Foot & Ankle International*. / American Orthopaedic Foot and Ankle Society [and] Swiss Foot and Ankle Society, 29(11), 1117–25. doi:10.3113/FAI.2008.1117
- [10] Bottlang, M., Marsh, J. L., & Brown, T. D. (1999). Articulated external fixation of the ankle: minimizing motion resistance by accurate axis alignment. *Journal of Biomechanics*, 32(1), 63–70.
- [11] Barg, A. Elsner, A. Chuckpaiwong, B. Hintermann, B. (2010). Insert Position in three Component Total Ankle Replacement. *Foot & Ankle International*. / American Orthopaedic Foot and Ankle Society [and] Swiss Foot and Ankle Society.
- [12] Giannini, S. (2000). Review article Total ankle replacement : review of the designs and of the current status, 77–88.
- [13] Gougoulias, N., Khanna, A., & Maffulli, N. (2010a). How successful are current ankle replacements?: a systematic review of the literature. *Clinical Orthopaedics and Related Research*, 468(1), 199–208. doi:10.1007/s11999-009-0987-3
- [14] Huiskes, R., Weinans, H., & van Rietbergen, B. (1992). The relationship between stress shielding and bone resorption around total hip stems and the effects of flexible materials. *Clinical Orthopaedics and Related Research*, (274), 124–34.
- [15] Insall JN, Binazzi R, Soudry M, Mestriner LA. Total knee arthroplasty. *Clin Orthop Relat Res*. 1985;(192):13-22.
- [16] Nunley, R. M., Ellison, B. S., Zhu, J., Ruh, E. L., Howell, S. M., & Barrack, R. L. (2012). Do patient-specific guides improve coronal alignment in total knee arthroplasty? *Clinical Orthopaedics and Related Research*, 470(3), 895–902. doi:10.1007/s11999-011-2222-2
- [17] Haaker, R. Konermann, W. (2013). *Computer and Template Assisted Orthopedic Surgery*. Berlin, Heidelberg: Springer Berlin Heidelberg. doi:10.1007/978-3-642-29728-1
- [18] Berlet, G. C., Penner, M. J., Lancianese, S., Stemmiski, P. M., & Obert, R. M. (2014). Total Ankle Arthroplasty Accuracy and Reproducibility Using Preoperative CT Scan-Derived, Patient-Specific Guides. *Foot & Ankle International*. / American Orthopaedic Foot and Ankle Society [and] Swiss Foot and Ankle Society. doi:10.1177/1071100714531232
- [19] Noble, J. W., Moore, C. a. & Liu, N. (2012). The value of patient-matched instrumentation in total knee arthroplasty. *The Journal of Arthroplasty*, 27(1), 153–5. doi:10.1016/j.arth.2011.07.006
- [20] MacDessi, S. J., Jang, B., Harris, I. A., Wheatley, E., Bryant, C., & Chen, D. B. (2014). A comparison of alignment using patient specific guides, computer navigation and conventional instrumentation in total knee arthroplasty. *The Knee* 21 (2014) 406–409, 21(2), 406–9. doi:10.1016/j.knee.2013.11.004
- [21] Mayer, S. Kevin. T. Hansen, B. Bolognesi, M (2012). Total Knee Arthroplasty in Osteopetrosis Using Patient-Specific Instrumentation. *The Journal of Arthroplasty Vol. 27 No. 8*.
- [22] Chareancholvanich, K., Narkbunnam, R., & Pornrattanamaneepong, C. (2013). A prospective randomised controlled study of patient-specific cutting guides compared with conventional instrumentation in total knee replacement. *The Bone & Joint Journal*, 95-B(3), 354–9. doi:10.1302/0301-620X.95B3.29903
- [23] Barret, W., Hoeffel, D., Dalury, D., Mason, J. B., Murphy, J., & Himden, S. (2014). In-vivo alignment comparing patient specific instrumentation with both conventional and computer assisted surgery (CAS) instrumentation in total knee arthroplasty. *The Journal of Arthroplasty*, 29(2), 343–7. doi:10.1016/j.arth.2013.06.029
- [24] Bugbee, W. D., Mizu-Uchi, H., Patil, S., & D'Lima, D. (2013). Accuracy of implant placement utilizing customized patient instrumentation in total knee arthroplasty. *Advances in Orthopedics*, 2013, 891210. doi:10.1155/2013/891210
- [25] Deprez, P., & Victor, J. (2012). Why using navigation in total knee arthroplasty? *The Knee Joint*. Chapter 82, pp 879-884.
- [26] Ng, V. Y., DeClaire, J. H., Berend, K. R., Gulick, B. C., & Lombardi, A. V. (2012). Improved accuracy of alignment with patient-specific positioning guides compared with manual instrumentation in TKA. *Clinical Orthopaedics and Related Research*, 470(1), 99–107. doi:10.1007/s11999-011-1996-6
- [27] Goldberg, A. J., Sharp, B., & Cooke, P. (2009). Early failure in total ankle replacements due to component malposition: a report of two cases. *Foot & Ankle International*. / American Orthopaedic Foot and Ankle Society [and] Swiss Foot and Ankle Society, 30(8), 783–7. doi:10.3113/FAI.2009.0783

- [28] Marimuthu K, Chen DB, Harris IA, Wheatley E, Bryant CJ, M. S. (2014). A Multi-Planar CT-Based Comparative Analysis of Patient-Specific Cutting Guides With Conventional Instrumentation in Total Knee Arthroplasty. *J Arthroplasty*. 2014 Jun;29(6):1138-42. Doi: 10.1016/j.arth.2013.12.019. Epub 2013 Dec 19.
- [29] Overhoff, H. M., & Engineering, M. (2006). Computer Assisted Orthopaedic Surgery. *International Journal of Computer Assisted Radiology and Surgery*, 1(S1), 229–250. doi:10.1007/s11548-006-0016-x
- [30] Jefferey, RS. Morris, RW. Denham, A. (1991). Coronal Alignment After Total Knee Replacement, 73(5).
- [31] Hollister, Anne. Jatana, Sanjay. Singh Anoop. Sullivan, William and Lupichuk, A. (1993). The axes of rotation of the knee. *Clinical Orthopaedics and Related Research*, 290, 259–268.
- [32] Stronach, BM. Pelt, CE. Erickson JA. Peters, C. (2014, June). Patient-specific instrumentation in total knee arthroplasty. *The Journal of Knee Surgery*. doi:10.1055/s-0034-1374813
- [33] DeHaan, A., Adams, J., DeHart, M., & Huff, T. W. (2014). Patient-specific versus conventional instrumentation for total knee arthroplasty: Peri-operative and cost Differences. *The Journal of Arthroplasty*. doi:10.1016/j.arth.2014.06.019
- [34] Hamilton, W. G., Parks, N. L., & Saxena, A. (2013). Patient-specific instrumentation does not shorten surgical time: a prospective, randomized trial. *The Journal of Arthroplasty*, 28(8 Suppl), 96–100. doi:10.1016/j.arth.2013.04.049
- [35] Ivie, C. B., Probst, P. J., Bal, A. K., Stannard, J. T., Crist, B. D., & Sonny Bal, B. (2014). Improved Radiographic Outcomes with Patient-Specific Total Knee Replacement. *The Journal of Arthroplasty*. doi:10.1016/j.arth.2014.06.024
- [36] Thienpont, E., Bellemans, J., Delpont, H., Van Overschelde, P., Stuyts, B., Brabants, K., & Victor, J. (2013). Patient-specific instruments: industry's innovation with a surgeon's interest. *Knee Surgery, Sports Traumatology, Arthroscopy: Official Journal of the ESSKA*, 21(10), 2227–33. doi:10.1007/s00167-013-2626-5
- [37] Klugeemail, W. H. (2007). Computer-assisted knee replacement techniques. *Current Orthopaedics*, 21(3), 200–206.
- [38] Hamid, K. S, Matson, A.P, Nwachukwu, B.U, Scott, D.J, Mather, R.C 3rd, DeOrio, J.K. (2016). Determining the Cost-Savings Threshold and Alignment Accuracy of Patient-Specific Instrumentation in Total Ankle Replacements. *Foot and Ankle International*, 2016 Sep 20. pii: 101100716667505.
- [39] Rydell, N. W. (1966). Forces acting on the femoral head-prosthesis. A study on strain gauge supplied prostheses in living persons. *Acta Orthopaedica Scandinavica*, 37, Suppl 88:1–132.
- [40] Waugh, T. R. (1966). Intra-vital measurements during instrumental correction of idiopathic scoliosis. *Acta Orthopaedica Scandinavica*, Suppl 93:1–87.
- [41] Ledet, EH. D'Lima, D. Westerhoff, P., Szivek, J. A., & Wachs, R. A. (2012). Implantable Sensor Technology: From Research to Clinical Practice Abstract. *Medical Engineering & Physics*, 20(6), 383–392.
- [42] D'Lima, D. D., Fregly, B. J., & Colwell, C. W. (2013). Implantable sensor technology: measuring bone and joint biomechanics of daily life in vivo. *Arthritis Research & Therapy*, 15(1), 203. doi:10.1186/ar4138
- [43] Brand, R. a, Pedersen, D. R., Davy, D. T., Kotzar, G. M., Heiple, K. G., & Goldberg, V. M. (1994). Comparison of hip force calculations and measurements in the same patient. *The Journal of Arthroplasty*, 9(1), 45–51.
- [44] Burny, F., Donkerwolcke, M., Moulart, F., Bourgois, R., Puers, R., Van Schuylenbergh, K., Lawes, P. (2000). Concept, design and fabrication of smart orthopedic implants. *Medical Engineering & Physics*, 22(7), 469–79.
- [45] Costigan, P. a, Deluzio, K. J., & Wyss, U. P. (2002). Knee and hip kinetics during normal stair climbing. *Gait & Posture*, 16(1), 31–7.
- [46] D'Lima, D. D., Fregly, B. J., & Colwell, C. W. (2013). Implantable sensor technology: measuring bone and joint biomechanics of daily life in vivo. *Arthritis Research & Therapy*, 15(1), 203. doi:10.1186/ar4138
- [47] D'Lima, D. D., Fregly, B. J., Patil, S., Steklov, N., & Colwell, C. W. (2012). Knee joint forces: prediction, measurement, and significance. *Proceedings of the Institution of Mechanical Engineers. Part H, Journal of Engineering in Medicine*, 226(2), 95–102.
- [48] D'Lima, D. D., Patil, S., Steklov, N., Slamin, J. E., & Colwell, C. W. (2006). Tibial forces measured in vivo after total knee arthroplasty. *The Journal of Arthroplasty*, 21(2), 255–62. doi:10.1016/j.arth.2005.07.011
- [49] D'Lima, D. D., Steklov, N., Patil, S., & Colwell, C. W. (2008). The Mark Coventry Award: in vivo knee forces during recreation and exercise after knee arthroplasty. *Clinical Orthopaedics and Related Research*, 466(11), 2605–11. doi:10.1007/s11999-008-0345-x
- [50] D'Lima, D. D., Townsend, C. P., Arms, S. W., Morris, B. A., & Colwell, C. W. (2005). An implantable telemetry device to measure intra-articular tibial forces. *Journal of Biomechanics*, 38(2), 299–304. doi:10.1016/j.jbiomech.2004.02.011
- [51] Damm, P., Graichen, F., Rohlmann, A., Bender, A., & Bergmann, G. (2010). Total hip joint prosthesis for in vivo measurement of forces and moments. *Medical Engineering & Physics*, 32(1), 95–100. doi:10.1016/j.medengphy.2009.10.003
- [52] Davy, DT. Kotzar, M. Brown, RHHeiple, K. G., Goldberg, M., Berillat, J., Reserve, M. W., & Engineering, A. (1988). Telemetric across Measurements Total the Hip after Arthroplasty *, 70(D).
- [53] English, TA. Kilvington, M. (1979). In Vivo Records of Hip Loads Using a Femoral Implant with Telemetric Output (a preliminary report), 1(2), 111–115.
- [54] Kutzner, I., Heinlein, B., Graichen, F., Bender, A., Rohlmann, A., Halder, A. Bergmann, G. (2010). Loading of the knee joint during activities of daily living measured in vivo in five subjects. *Journal of Biomechanics*, 43(11), 2164–73. doi:10.1016/j.jbiomech.2010.03.046
- [55] Almouahed, S., Gouriou, M., Hamitouche, C., Stindel, E., & Roux, C. (2011). Smart Knee Implant. *IEEE Transactions on Biomedical Engineering*, 58(4), 971–982.
- [56] Westerhoff, P., Graichen, F., Bender, A., Rohlmann, A., & Bergmann, G. (2009). An instrumented implant for in vivo measurement of contact forces and contact moments in the shoulder joint. *Medical Engineering & Physics*, 31(2), 207–13. doi:10.1016/j.medengphy.2008.07.011
- [57] Graichen, F., Arnold, R., Rohlmann, A., & Bergmann, G. (2007). Implantable 9-channel telemetry system for in vivo load measurements with orthopedic implants. *IEEE Transactions on Bio-Medical Engineering*, 54(2), 253–61. doi:10.1109/TBME.2006.886857
- [58] Erhart, J. C., Dyrby, C. O., D'Lima, D. D., Colwell, C. W., & Andriacchi, T. P. (2010). Changes in in vivo knee loading with a variable-stiffness intervention shoe correlate with changes in the knee adduction moment. *Journal of Orthopaedic Research: Official Publication of the Orthopaedic Research Society*, 28(12), 1548–53. doi:10.1002/jor.21183

- [59] Anderson, I. a., MacDiarmid, A. a., Harris, M. L., Gillies, R. M., Phelps, R., & Walsh, W. R. (2003). A novel method for measuring medial compartment pressures within the knee joint in-vivo. *Journal of Biomechanics*, 36(9), 1391–1395. doi:10.1016/S0021-9290(03)00158-1
- [60] Fregly, B. J., Besier, T. F., Lloyd, D. G., Delp, S. L., Banks, S. A., Pandy, M. G., & D’Lima, D. D. (2012). Grand challenge competition to predict in vivo knee loads. *Journal of Orthopaedic Research : Official Publication of the Orthopaedic Research Society*, 30(4), 503–13. doi:10.1002/jor.22023
- [61] Taylor, S. J., & Walker, P. S. (2001). Forces and moments telemetered from two distal femoral replacements during various activities. *Journal of Biomechanics*, 34(7), 839–48.
- [62] Arami, A., Simoncini, M., Atasoy, O., Hasenkamp, W., Ali, S., Bertsch, A. Ryser, P. (2011). Instrumented prosthesis for knee implants monitoring. 2011 IEEE International Conference on Automation Science and Engineering, 828–835.
- [63] Holmberg, J., Alexander, L., Rajamani, R., & Bechtold, J. E. (2013). Battery-Less Wireless Instrumented Knee Implant. *Journal of Medical Devices*, 7(1), 011006. doi:10.1115/1.4023412
- [64] Bergmann G, Graichen F, R. A. (1993). Hip joint loading during walking and running, measured in two patients. *Journal of Biomechanics*, 8, 969–90.
- [65] Bergmann, G., Graichen, F., Rohlmann, A., Bender, A., Heinlein, B., Duda, G. N, Morlock, M. M. (2010). Realistic loads for testing hip implants. *Bio-Medical Materials and Engineering*, 20(2), 65–75. doi:10.3233/BME-2010-0616
- [66] Heller, M. O., Bergmann, G., Deuretzbacher, G., Dürselen, L., Pohl, M., Claes, L, Duda, G. N. (2001). Musculo-skeletal loading conditions at the hip during walking and stair climbing. *Journal of Biomechanics*, 34(7), 883–93.
- [67] Kirking, B., Krevolin, J., Townsend, C., Colwell, C. W., & D’Lima, D. D. (2006). A multiaxial force-sensing implantable tibial prosthesis. *Journal of Biomechanics*, 39(9), 1744–51. doi:10.1016/j.jbiomech.2005.05.023
- [68] Hodge, W. A., Fijan, R. S., Carlson, K. L., Burgess, R. G., Harris, W. H., & Mann, R. W. (1986). Contact pressures in the human hip joint measured in vivo. *Proceedings of the National Academy of Sciences*, 83(9), 2879–2883. doi:10.1073/pnas.83.9.2879
- [69] Rohlmann, A., Bergmann, G., Graichen, F., & Weber, U. (1997). Comparison of loads on internal spinal fixation devices measured in vitro and in vivo. *Medical Engineering & Physics*, 19(6), 539–46.
- [70] Seiregt, A., & Arvikar, R. J. (1971). The Prediction of Muscular Load Sharing and Joint Forces in the Lower Extremities During Walking.
- [71] Stansfield, B. W., Nicol, A. C., Paul, J. P., Kelly, I. G., Graichen, F., & Bergmann, G. (2003). Direct comparison of calculated hip joint contact forces with those measured using instrumented implants. An evaluation of a three-dimensional mathematical model of the lower limb. *Journal of Biomechanics*, 36(7), 929–36.
- [72] Brand, R. a, Pedersen, D. R., Davy, D. T., Kotzar, G. M., Heiple, K. G., & Goldberg, V. M. (1994). Comparison of hip force calculations and measurements in the same patient. *The Journal of Arthroplasty*, 9(1), 45–51.
- [73] Morrison, J. B. (1970). The mechanics of the knee joint in relation to normal walking. *Journal of Biomechanics*, 3(1), 51–61
- [74] Taylor, W. R., Heller, M. O., Bergmann, G., & Duda, G. N. (2004). Tibio-femoral loading during human gait and stair climbing. *Journal of Orthopaedic Research : Official Publication of the Orthopaedic Research Society*, 22(3), 625–32. doi:10.1016/j.orthres.2003.09.003
- [75] Lin, Y.-C., Walter, J. P., Banks, S. a, Pandy, M. G., & Fregly, B. J. (2010). Simultaneous prediction of muscle and contact forces in the knee during gait. *Journal of Biomechanics*, 43(5), 945–52. doi:10.1016/j.jbiomech.2009.10.048
- [76] Antonius Rohlmann, L. H. Riley, G. Bergmann, F. G. (1996). In vitro load measurement spinal fixation device using an instrumented. *Medical Engineering and Physics*, 18(6), 485–488.
- [77] L. Lanyon, W. Hampson, A. Goodship, J. Shah, “Bone deformation recorded in vivo from strain gauges attached to the human tibial shaft.”, *Acta Orthopaedica Scandinavica*, 46(2), 256–68, 1975.
- [78] U. Von Jan, D. Sandkühler, L. Kirch, O. Rühmann, H.M. Overhoff. “Surgical Planning for the Humeral part of a Shoulder Endoprosthesis Surgery Based on Landmarks De termined from 3D Ultrasound Volumes”, *International Journal of Computer Assisted Radiology and Surgery*, 1(S1), 229–250. DOI: 10.1007/s11548-006- 0016-x. 2006.
- [79] K. Johnson, *Contact Mechanics*, 9th edition, Cambridge University Press, ISBN 0 521 347963. 2005.
- [80] V. Popov. *Contact Mechanics and Friction*. Springer, ISBN: 978-3-642-10802-0. DOI: 100.1007/978-3-642-10803-0. 2010.
- [81] L. Lediaev, *Modeling Piezoelectric PVDF Sheets with Conductive Polymer Electrodes*, Montana State University, Bozeman, Montana, 2006.
- [82] V. Piefort. *Finite Element Modeling of Piezoelectric Active Structures*. Université Libre de Bruxelles, Faculty of Applied Sciences. 2001.
- [83] Younis, M.I. *MEMS Linear and Nonlinear Statics and Dynamics*. Springer books (2011). ISBN 978-1-4419-6019-1. DOI: 10.1007/978-1-4419-6020-7. Chapter 3, pp 61-70.
- [84] F. Beer, E. Johnson, J. DeWolf, *Mechanics of Materials*, 4th Edition, McGraw Hill, ISBN 0-07-298090-7. 2006.
- [85] Abaqus 6.13-1 Documentation.
- [86] PIÉZOTECH S.A.S. Piezoelectric Films Technical Information. [ONLINE]. Available at: <http://www.piezotech.fr/image/documents/22-31-32-33-piezotech-piezoelectric-films-leaflet.pdf>. [Accessed 08-JAN-2017]
- [87] GoodFellow. Technical Information – Polyvinylidene fluoride, FV301301. [ONLINE]. Available at http://www.goodfellow.com/catalogue/GFCat4J.php?ewd_token=q9zyi5fdPegPYsoFrT0kpEwkHCEfkn&n=BXLssWfMMMwuhc9Dkih65GnZNEZ1S. Accessed 10-JAN-2017]
- [88] S. Kon, K. Oldham, R. Horowitz. Piezoresistive and Piezoelectric MEMS Strain Sensors for Vibration Detection. *Sensors and Smart Structures Technologies for Civil, Mechanical and Aerospace Systems*. 2007. Proc. of SPIE Vol. 6529 65292V-1

Appendix A

Determining Experimental Contact Force

The experiment setup consisted on having an operator to manually place the instrument on to the bone surface and push with the amount of force needed to make sure the instrument was locked in position. The materials and equipment are listed in table below

TABLE XIX. MATERIALS AND EQUIPMENT FOR EXPERIMENT SETUP

| Materials | Manufacturer | Model/Series No. | Calibration date |
|--|----------------|------------------|------------------|
| Patient Specific Instrument for tibia bone | Wright Medical | NA | NA |
| 3D Printed Bone model of tibia bone | Wright Medical | NA | NA |
| Analytical Mass Balance | Precisa | 2200C/68160 | 10-OCT-2014 |

The experiment was conducted on June the 29th in 2015, approximately 8 months after the last registered calibration. However, the equipment is calibrated on yearly basis. Therefore, it was under calibrated parameters when used. Figures A1 and A2 below, show the calibration information regarding the analytical scale used during the experiment run.

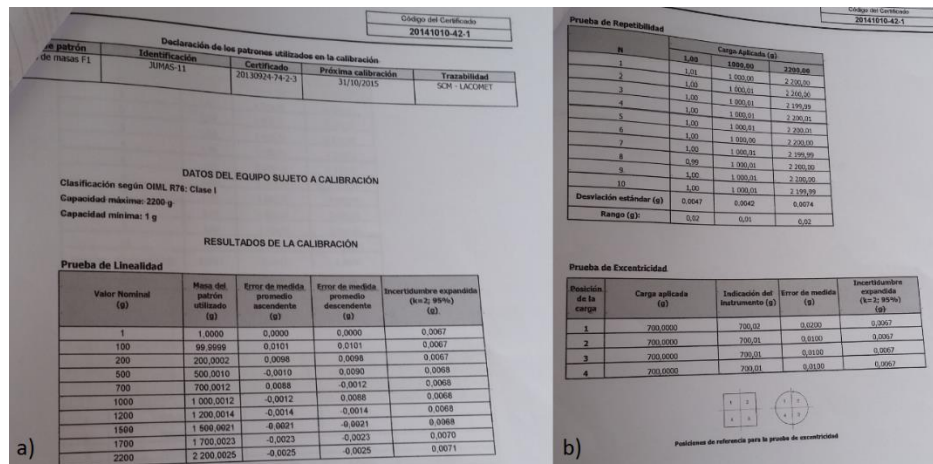


Figure A1. Calibration results from last registered calibration on October 10th 2014, a) general information and linearity test, b) repeatability and eccentricity tests.



Figure A2. Calibration results from last registered calibration on October 10th 2014, a) general information and linearity test, b) repeatability and eccentricity tests.

For each run, the operator removed the instrument and bone model and performed the instructions all over, for a total of 90 runs. All the readings taken from the scale were recorded on Table XIX, shown below.

TABLE XX. EXPERIMENT RUNS AND RECORDS

| Run Order | Reading value from mass balance (g) |
|-----------|-------------------------------------|
| 1 | 1018.62 |
| 2 | 1118.29 |
| 3 | 1011.29 |
| 4 | 1060.74 |
| 5 | 1026.89 |
| 6 | 972.90 |
| 7 | 1070.45 |
| 8 | 925.37 |
| 9 | 1222.05 |
| 10 | 1035.02 |
| 11 | 1065.82 |
| 12 | 1070.86 |
| 13 | 1005.60 |
| 14 | 944.64 |
| 15 | 986.76 |
| 16 | 946.48 |
| 17 | 901.64 |
| 18 | 892.37 |
| 19 | 1001.45 |
| 20 | 817.68 |
| 21 | 980.16 |
| 22 | 1045.05 |
| 23 | 931.54 |
| 24 | 985.62 |
| 25 | 978.65 |
| 26 | 1020.18 |
| 27 | 1026.37 |
| 28 | 1108.37 |
| 29 | 1080.54 |
| 30 | 1015.61 |
| 31 | 1007.10 |
| 32 | 999.83 |
| 33 | 1006.55 |
| 34 | 975.50 |
| 35 | 1108.53 |
| 36 | 1020.15 |
| 37 | 1049.35 |
| 38 | 1007.40 |
| 39 | 996.15 |
| 40 | 970.45 |
| 41 | 938.75 |

| Run Order | Reading value from mass balance (g) |
|------------------|--|
| 42 | 1035.88 |
| 43 | 1024.35 |
| 44 | 1062.38 |
| 45 | 1012.60 |
| 46 | 1053.03 |
| 47 | 1064.53 |
| 48 | 1005.43 |
| 49 | 1037.43 |
| 50 | 1130.80 |
| 51 | 1087.63 |
| 52 | 1032.70 |
| 53 | 1071.95 |
| 54 | 1082.53 |
| 55 | 1091.70 |
| 56 | 1157.08 |
| 57 | 1159.95 |
| 58 | 1070.45 |
| 59 | 1222.00 |
| 60 | 1158.13 |
| 61 | 1054.04 |
| 62 | 1146.63 |
| 63 | 964.66 |
| 64 | 1036.70 |
| 65 | 1017.75 |
| 66 | 1091.27 |
| 67 | 1246.05 |
| 68 | 1151.00 |
| 69 | 1265.95 |
| 70 | 1170.88 |
| 71 | 1117.29 |
| 72 | 1023.06 |
| 73 | 1004.37 |
| 74 | 1153.01 |
| 75 | 1172.53 |
| 76 | 1084.55 |
| 77 | 1001.00 |
| 78 | 1063.84 |
| 79 | 1097.10 |
| 80 | 1054.57 |
| 81 | 1190.00 |
| 82 | 1151.72 |
| 83 | 1038.93 |
| 84 | 1130.47 |
| 85 | 1077.06 |
| 86 | 1196.81 |
| 87 | 1174.55 |
| 88 | 1172.66 |
| 89 | 1168.69 |
| 90 | 1180.42 |

Appendix B

Source Code for Arduino program

```
/*
  Data_Aqq
  Data Acquisition Program for Arduino Coarse Reading

  ITCR

  modified Nov 2016
  by Roy Araya & Marco Bedoya
*/

int A = 0; // Digital input for large MUX1 S0
int B = 0; // Digital input for large MUX1 S1
int C = 0; // Digital input for large MUX1 S2
int D = 0; // Digital input for large MUX1 S3
int E = 0; // Digital input for large MUX2 S0
int F = 0; // Digital input for large MUX2 S1
int G = 0; // Digital input for large MUX2 S2
int H = 0; // Digital input for large MUX2 S3

int countpinA = 7; // count variable for selecting the Mux output for the columns of the sensor.
int countpinB = 0; // count variable for selecting the Mux output for the rows of the sensor.
int delta = 0; // Variable for comparing values higher than the desired read we want to have to start out the
program.
int state = 0; //State variable to separate stages of the program.
int i = 0; //counter for columns
int j = 0; //counter for rows
int col = 0;
int row = 0;
int datacolumn[13]; //array for number of columns
int datarow[13]; //Array for number of rows
int datacombined[9][13]; //Combined 2D array for the rows and columns
int bin [] = {0000, 1, 10, 11, 100, 0101, 0110, 0111, 1000, 01001, 01010, 01011, 01100, 11101, 01110,
01111};

int flag = 0;

void setup() {

pinMode(22, OUTPUT);
pinMode(23, OUTPUT);
pinMode(24, OUTPUT);
pinMode(25, OUTPUT);
pinMode(26, OUTPUT);
pinMode(27, OUTPUT);
pinMode(28, OUTPUT);
```

```

pinMode(29, OUTPUT);

memset(datacolumn, 0, sizeof(datacolumn));
memset(datarow, 0, sizeof(datarow));

state = 0;

Serial.begin(9600); //starting the serial port

Serial.println("=====
=\n");

}

void loop() {

    delta = analogRead(A0);
    //Serial.print("Delta: "); //Lines needed for debugging if a misreading is encountered
    //Serial.println(delta); //Lines needed for debugging if a misreading is encountered

    //Serial.print("Estado =====> "); //Lines needed for debugging if a misreading is encountered
    //Serial.println(state); //Lines needed for debugging if a misreading is encountered

    //Estado 0 = The program is waiting a change in the signal for the reading to start
    if (state == 0){
        //Serial.println("ooooooooo_Estado_1_oooooooooooo"); //Lines needed for debugging if a misreading is
        encountered
        if (delta > 800){ //Si la lectura del pin A0 es mayor a XXXXXX se puede decir que ya se puede hacer la
        lectura
            //Serial.println("====="); encountered
            state = 1; //State is now changed to State 1
        }
    }

    //Initial state to begin with the readings from the sensor
    if (state == 1) {

        for (i = 0; i < 9; i++) {

            col = bin[countpinA];

            A = bitRead(col,0); //A0 and reads the farthest right bit from the binary equivalent number from the
            channel, for instance: if is channel 4, binary will be 100
            B = bitRead(col,1); //A1 and reads the second bit from the right and so on...
            C = bitRead(col,2); //A2 and reads the third bit from the right and so on...
            D = bitRead(col,3); //A3 and reads the fourth bit from the right and so on...

            //Here the variables are configured so the AnalogRead0 meets the corresponding column

            digitalWrite(22, A); //combination of logic pins in the large MUX1 to open the door of the binary number
            + 1.
            digitalWrite(23, B); //combination of logic pins in the large MUX1 to open the door of the binary number
            + 1.
            digitalWrite(24, C); //combination of logic pins in the large MUX1 to open the door of the binary number
            + 1.

```

```
digitalWrite(25, D); //combination of logic pins in the large MUX1 to open the door of the binary number
+ 1.
```

```
//Here the column mux has been setup for the corresponding pin reading.
```

```
//Column Analog reading
datacolumn[i] = analogRead(A0);
```

```
countpinA = countpinA + 1;
```

```
for (j = 0; j < 13; j++) {
```

```
    row = bin[countpinB];
```

```
    E = bitRead(row,0); //A0 for large MUX2
```

```
    F = bitRead(row,1); //A1 for large MUX2
```

```
    G = bitRead(row,2); //A2 for large MUX2
```

```
    H = bitRead(row,3); //A3 for large MUX3
```

```
    //Here the variables are configured so the AnalogRead1 meets the corresponding row
```

```
    digitalWrite(26, E);
```

```
    digitalWrite(27, F);
```

```
    digitalWrite(28, G);
```

```
    digitalWrite(29, H);
```

```
    //Here the row mux has been setup accordingly to each pin reading.
```

```
    //Row Analog reading
```

```
    datarow[j] = analogRead(A1);
```

```
    countpinB = countpinB + 1;
```

```
    datacombined[i][j] = (datacolumn[i] + datarow[j])/2;
```

```
    }
```

```
  }
```

```
  state = 2;
```

```
}
```

```
if (state == 2) {
```

```
  for (j = 0; j < 13; j++) {
```

```
    for (i = 0; i < 9; i++) {
```

```
      Serial.print(datacombined[i][j]);
```

```
      Serial.print(" \t");
```

```
    }
```

```
    Serial.println("\n");
```

```
  }
```

```
Serial.println("=====
=");
```

```
  state = 3;
```

```
}
```

```
if (state == 3) {
```

```
}
```

```
}
```

Appendix C

Data Acquisition Board Schematic, layout information and Bill of Materials (BOM)

The PCB design for the data acquisition system was developed using Eagle 7.2.0 layout software. The schematic from where the layout was created is shown below in Figure C1. Also, the symbology and the bill of materials are also listed below.

TABLE XXI. SYMBOL DESCRIPTION FOR SCHEMATIC READING

| Symbol | Description |
|-----------------------------|---|
| S#A#_NII# e.g. S1A1_NII1 | Sensor line # connected to amplifier # to the non-inverting input # (each amplifier has 4 non-inverting inputs) Sensor line1 connected to amplifier 1 to the non-inverting input 1 |
| GND | Ground Connection |
| R(even number) | 2kΩ Metal Resistors +/-1% tolerance |
| R (odd number) | 10kΩ Metal Resistors +/-1% tolerance |
| V+ | Vcc = +5V |
| V- | Vee = -5V |
| A#O# e.g. A1O3 | Amplifier number followed by output number (each amplifier has 4 outputs) e.g. Amplifier #1 Output#3 |
| A#II# e.g. A1II4 | Amplifier number followed by the inverted input pin number (each amplifier has 4 inverted input pins) e.g. Amplifier #1 inverted input #4 |
| M#VD e.g. M1VD | Multiplexer number output e.g. Multiplexer #1 output |
| M#A0 e.g. M2A0 | 16 channel Multiplexer number address or selection pin A0, per manufacturer datasheet e.g. Multiplexer #2 address pin A0 |
| M#A1 | 16 channel Multiplexed number address or selection pin A1, per manufacturer datasheet |
| M#A2 | 16 channel Multiplexed number address or selection pin A2, per manufacturer datasheet |
| M#A3 | 16 channel Multiplexed number address or selection pin A3, per manufacturer datasheet |
| Horizontal Inputs | 17x1 male pin connectors with 0.1" pitch |
| Vertical Inputs | 25x1 male pin connectors with 0.1" pitch |
| JP39 | 10x1 male pin connectors with 0.1" pitch |
| J1 & J2 | Female Jack connectors 2mm inner diameter |
| C# | Non-polarized Capacitor number |
| C12, C15, C13 and C14 | Polarized capacitors with corresponding capacitance values |
| D# | Diode number |
| L7805 | Positive voltage regulator |
| L7905 | Negative voltage regulator |
| Probes | 1x1 male pin headers for circuit verification (located at the lower left corner of the schematic) |

TABLE XXII. BILL OF MATERIALS FOR DAQ BOARD LAYOUT

| Part Description | Manufacturer | Part Number | Value | Quantity |
|-----------------------------|-----------------------|-----------------|---|----------|
| 4-1 rail-to-rail op amp | Texas Instruments | LMC6484 CMOS | NA | 8 |
| CMOS analog multiplexers | Maxim | DG506A | NA | 2 |
| +/-1% Metal Resistors | Multiple | NA | 2k Ω | 22 |
| +/-1% Metal Resistors | Multiple | NA | 10k Ω | 22 |
| Ceramic capacitors | Multiple | NA | 0.110 μ F | 6 |
| 2:1 channel multiplexor | Analog Devices | AD8180 | NA | 2 |
| Male pin headers 0.1" pitch | Pololu or equivalent | NA | NA | 82 |
| 2mm Female jack connectors | CUI Inc or equivalent | PJ-202A | NA | 2 |
| Diodes | Multiple | IN4004 | NA | 4 |
| Polarized capacitor | Multiple | NA | 0.1 μ F, 1.0 μ F or 1.1 μ F | 2 |
| Polarized capacitor | Multiple | NA | 0.33 μ F or 2.0 μ F | 2 |
| Positive voltage regulator | ST | L7805 | 5V | 1 |
| Negative voltage regulator | ST | L7905 | 5V | 1 |

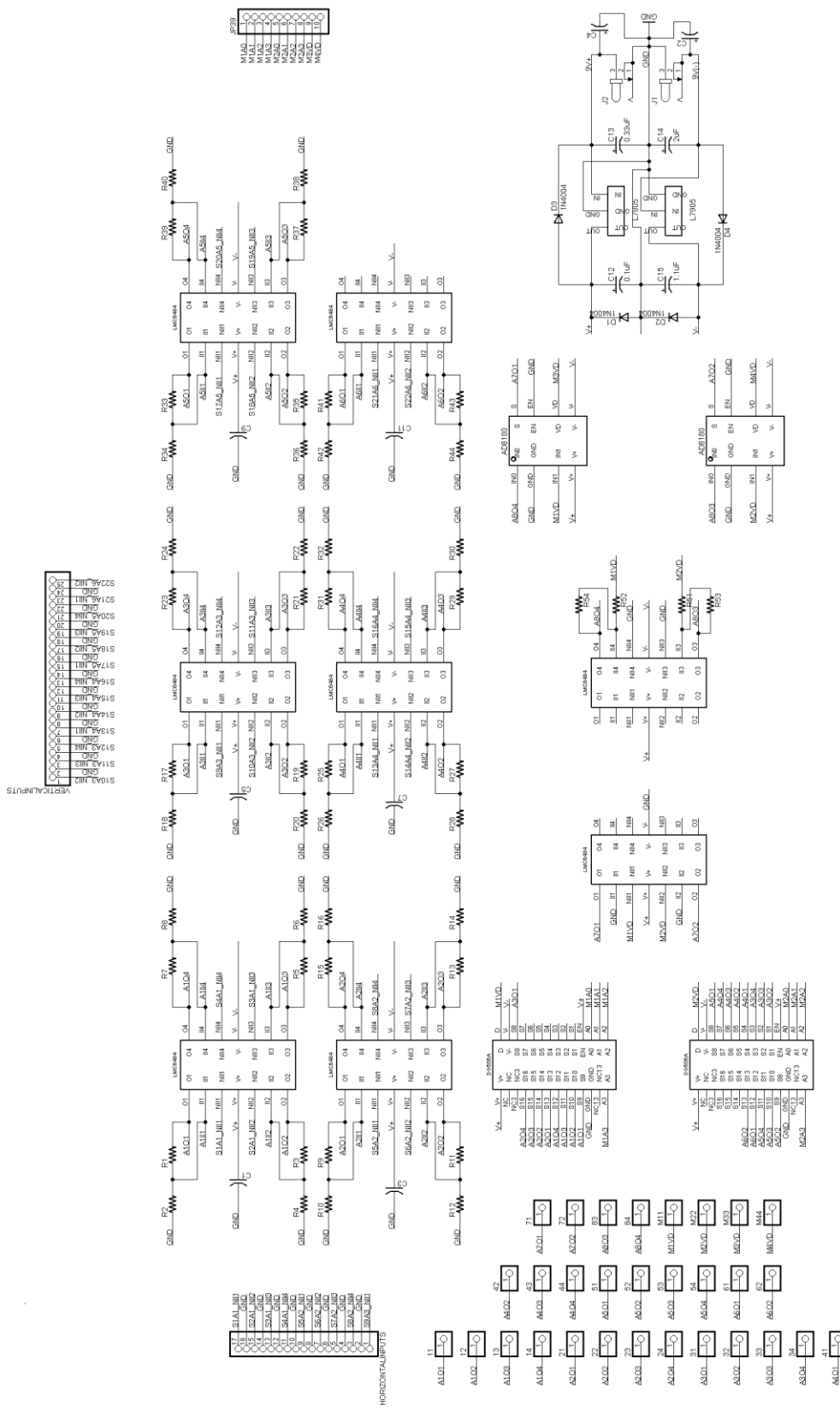


Figure C1. DAQ Board schematic image.